Wave propagation in stented blood vessels

Thesis submitted in accordance with the requirements of
the University of Liverpool for the degree of Doctor in Philosophy by

Sara Frecentese

September 2020

Abstract

This thesis introduces and develops a number of mathematical models to investigate the propagation of waves in a stented artery. Generally, healthy arteries have smooth inner walls and blood flows through them easily. However, vessels may become occluded due to the accumulation of plaque on the inner walls, which can reduce blood flow or, in some instances, block it altogether. Intraluminal stenting is one technique that can be performed to restore adequate flow and avoid ischaemia (restriction of blood flow to tissues) occurring.

Arterial walls are elastic and subjected to pulse waves originating from the left ventricle of the heart, the frequency of which vary with physical activity and possible disease states. It is important to identify how the reinforcement of arteries with stents may affect the propagation of these waves through the arterial network. New models are proposed here to analyse how elastic waves, induced by a pulsating flow in a stenotic artery containing several stents, are reflected and transmitted, both in the frequency and time domains.

The reflection of waves in blood vessels is well documented in the literature, but it has generally been linked to a strong variation in geometry, such as the branching of vessels. The aim of this work is to detect the possibility of wave reflection in a stented artery due to the repetitive pattern of the stents, using the Bloch-Floquet approach and the analysis of reflection-transmission problems. The investigation of time-harmonic wave propagation and possible blockages is complemented with numerical simulations in the transient regime.

Dispersion properties of the waves depend on the stent structure and are addressed throughout this thesis. Several vascular stenting procedures include overlapping stents; this configuration is included within the models, as well as the presence of atherosclerotic plaque. An additional analytical one-dimensional model is developed as an approximation to the full three-dimensional methods. The analytical derivations are accompanied by numerous illustrative examples and simulations.

This thesis introduces a complete set of coupled fluid-solid models to analyse wave propagation in stented arteries. An appealing aspect of the work is that the one-dimensional model is able to identify ranges of interest rapidly, which can then be investigated in more detail using the more precise, but time-consuming, full three-dimensional models.

Contents

List of Figures and Tables

List of Figures

List of Tables

Acknowledgements

I would like to thank Professors Alexander and Natasha Movchan. It has been a great privilege and pleasure to have them as supervisors during the PhD. Their encouragement and dedication has been very important for me to grow and understand how beautiful it is to work in academia as a researcher. They have been extremely helpful with their insight and support during these years of research.

I would like to thank the co-authors of my papers: Dr Luca Argani, Dr Giorgio Carta, Dr Theodosios Papathanasiou and Mr Mike Wall for providing their valuable knowledge in the different areas and aspects of the research. I feel very lucky to have had the great honour to work with all of them.

A huge thanks to my former flatmate Eugenia who supported me during the moments of stress and despair, because we both know that research is not all roses. It has been wonderful to live three years together and have shared the same experience. I still can't believe how lucky I was to find you. I have to say I miss our nights with dinner and movies and sticky toffee pudding (very valuable to relieve the daily stress). I have also to thank you for all the dinners you prepared for me when I was late home from work. You are a very thoughtful friend.

And of course I would like to thank my family. Mamma, papà, Dani, Greg, Marco, Stefano and Francesca thanks for your love and support. (Stefano traduci). A big thanks also to my new family, Sandy, Mike, Gareth, Toby and Mandy. It is an honour and I feel very lucky to be part of the Haslinger family. Thanks to all of you for your support and help with English. A particular thanks to Gareth who proofread the whole thesis.

Last, but the most important, a huge thanks to my husband, Stewart. We met during my first year of PhD and we got married during the last year and you have always been there for me by my side, supporting and encouraging me more than anyone else. Thanks love of my life. Words simply can't describe how thankful I am.

List of publications

1. S. Frecentese, L. P. Argani, A. B. Movchan, N. V. Movchan, G. Carta, and M. L. Wall. Waves and fluid–solid interaction in stented blood vessels. *Proceedings of the Royal Society of London A: Mathematical, Physical and Engineering Sciences*, 474 (2209), 2018. doi: 10.1098/rspa.2017.0670

2. S. Frecentese, T. K. Papathanasiou, A. B. Movchan, and N. V. Movchan. Dispersion of waves and transmission–reflection in blood vessels with structured stents. *Proceedings of the Royal Society of London A: Mathematical, Physical and Engineering Sciences*, 475(2223):20180816, 2019. doi: 10.1098/rspa.2018.0816

3. M. Wall, S. Frecentese, N. Movchan, and A. Movchan. Dynamic response of stents in vascular systems: Development of an adaptive model to study the effect of stent placement on aneurysmal and occlusive arterial disease in various anatomical configuration. *European Journal of Vascular and Endovascular Surgery*, 58(6):e853, 2019

Conference Presentations

1. EPSRC Workshop - Elastic deformation and dynamic response of aneurysm repairs: modelling and applications, *University of Liverpool*, (2017): **Modelling of waves in stented blood vessels**

2. 59th British Applied Mathematics Colloquium, *University of Surrey, Guildford*, (2017): **Bloch waves in blood vessels with stents**

3. The Vascular Societies' Annual Scientific Meeting, *Manchester*, (2017): **Wave propagation and fluid-structure interaction in stented blood vessels**

4. 61st British Applied Mathematics Colloquium, *University of Bath, Bath*, (2019): **Propagation of waves and transmission-reflection in stented arteries**

5. 14th International Conference on Vibration Problems, *Crete, Greece*, (2019): **Propagation of waves in stented arteries: 3D and 1D models**

Chapter 1

Introduction

Cardiovascular disease (CVD) is the most common cause of mortality in adults within the Western world. The pathological process underpinning CVD is atherosclerosis, which can lead to narrowing and/or occlusion of blood vessels and result in an interruption in blood flow to the heart. Common causes are the accumulation of plaque within arteries or thickening of the arterial wall, see Charonko *et al.* [26], for example. The resulting reduction in both the volume and velocity of blood flow causes tissue ischaemia (lack of oxygen delivery) in the region supplied by the affected artery. Intraluminal stenting is one technique that can be performed to restore adequate flow and avoid ischaemia occurring. The outcomes of stenting vary, depending on the anatomical site of the diseased arteries. For example, coronary stents have very good success rates in improving patency (degree of openness measured as a percentage) of vessels, preventing further cardiac ischaemia and avoiding the need for surgical bypass.

However, stenting of larger limb vessels in peripheral vascular disease has been less successful and large amounts of energy and resources have been exhausted in determining explanations. The reasons for this variability in stenting outcome are poorly understood and likely to be multifactorial. Arterial walls are elastic and subjected to pulse waves originating from the left ventricle of the heart, the frequency and regularity of which are altered with physical activity and multiple disease states. It is a possibility that reinforcement of arteries with stents alters the propagation of pulse waves through the arterial network, changing the flow dynamics. This may lead to decreased flow velocity or increased shear stresses in the arterial wall that could induce changes leading to restenosis of occlusion.

The standard reference for blood flow in arteries is the book by McDonald, first published in 1960 [76]. Since then, several updated editions have been published [94], which include the latest scientific, technical and medical developments that occurred in the intervening years. Several topics are covered by McDonald, including coronary circulation, atherosclerosis, reflection of waves, harmonic analysis of pressure and flow in the arterial system etc.

Reflection of waves in blood vessels is a well known phenomenon, but it has always been related to strong geometrical changes within the arterial tree, such as the branching

of vessels. Some references for the topic of branching include the books by Ethier and Simmons [32] and by Humphrey and O'Rourke [56]. Standing, or stationary, waves are rarely observed, as reported by Peynircioglu *et al.* [98] but appear as multiple serrated indentations symmetrically distributed at evenly spaced intervals along arteries; in most cases, these have been seen at peripheral arteries [98]. A major aim of this thesis is to investigate whether reflection of waves can occur in a stented artery, due to the reinforcement provided by the stents. Mathematical models, informed by the vast literature of medical research on the subject, were derived to increase understanding of the underlying physics and biomedical mechanisms associated with blood flow in stented arteries.

Wave propagation in fluid-filled cylinders has been extensively investigated in the applied dynamics literature. Fluid-solid structure interaction is well-known to be challenging; on one hand, it is difficult to find solutions in a closed form, meaning that approximations and/or numerical techniques were often employed; on the other hand, the study of the dynamics of fluid-filled cylinders constitutes the basis for the analysis of piping systems for a range of applications. Examples listed in the recent study by Jiang *et al.* [58] include the oil and water industries (often for the detection of potential leaks), manufacturing industries (for example, food, pharmaceutical and chemical industries) and in several engineering sectors, from civil to mechanical.

For example, the collection of papers by Baik *et al.* [9, 10] and by Jiang *et al.* [58] compared results for an analytical model [9] with finite element methods [58] for predictions of attenuation and sound speeds in a fluid-filled pipe. Two practical applications, beyond the analysis of the original analytical model [9], were investigated in [58] demonstrating the versatility of mathematical modelling techniques. The first example models acoustic propagation within the mercury-filled steel pipework of the Spallation Neutron Source at the Oak Ridge National Laboratory in Tennessee in the United States. The second example considers acoustic sensors used on planetary probes. The results showed the importance of modelling the fluid-solid coupling correctly.

Theoretically, several early investigations were conducted to determine the resonant frequencies and wave propagation in piping systems with fluids [31, 61–63, 72]. The frequency equation for vibrations of a thin cylindrical elastic shell, filled with non-viscous, compressible fluid, was derived using the exact three dimensional equations of motion for the shell by Kumar [61]. The equation was solved for two different sets of parameters, with comparisons provided with respect to the preceding work by Lin and Morgan [72], which used a basis of approximate equations of motion. Further work by Kumar included a study of the flexural vibrations of empty and fluid-filled shells of varying thickness [62]. The analysis identified propagating and attenuating modes and it was observed that the effect of the fluid was negligible on the vibrations of thick shells. As the wall thickness decreases, additional modes of vibration, linked to the presence of the fluid, arise. It was also noted that for the attenuating modes, the frequency spectra of the fluid-filled shells follow the spectra of an empty shell, or of a fluid column with rigid walls.

In a subsequent study by Kumar [63], dispersion of axially symmetric waves in empty and fluid-filled circular cylindrical shells, of varying thickness, was investigated. A specific regime of frequency and wavenumber was found such that the number of real, imaginary and complex branches for an empty shell decreases as the walls become thinner. However, the presence of fluid within the shell contributes extra radial modes of vibration and, therefore the number of real, imaginary and complex branches increases as the walls become thinner for a fluid-filled shell. The analysis also used exact three-dimensional equations of linear elasticity and thus presented a comparison of various shell theories.

A complementary study on the dispersion behaviour and distributions of energy for free waves in thin-walled cylindrical elastic shells filled with fluid were investigated by Fuller and Fahy [39]. Dispersion curves were presented for a range of parameters and the characteristics of individual branches were discussed and explained. A non-dimensional equation that provides the distribution of vibrational energy, between the shell wall and the filling fluid, was also derived, as well as its variation with frequency and material parameters.

Some more recent studies include Liu *et al.* [73], which considers the effect of hydrostatic pressure on the vibration dispersion characteristics of fluid-loaded and fluid-filled cylindrical shells, and Zhang *et al.* [126]. The latter article implements a wave propagation model to analyse coupled structural-acoustic systems of finite fluid-filled cylindrical shells. The coupled analysis provides comparisons of the frequencies with those obtained using established numerical finite element/boundary element methods (FEM/BEM). The fluid effect on the shell was shown to be significant, as indicated many years earlier by Kumar [62].

Of course, there are also significant achievements devoted to the motions of empty cylindrical shells, including the early technical report produced by Herrmann and Mirsky [47] for the United States Airforce in 1955, which led directly to two research articles [48, 83]. The first of these papers [48] demonstrated a Timoshenko-type theory for cylindrical shells possessing axial symmetry, which was then generalised to include non-axially symmetric motion [83]. The original model described the connection of transverse shear and rotatory inertia, in addition to the standard membrane and bending effects, but was restricted to axially symmetric motion. The subsequent generalisation to non-axially symmetric motion, which includes the axially symmetric theory as a special case, is able to describe a much wider range of phenomena than the classical shell theories that were limited to membrane and bending effects only.

As an extension to the model the propagation of free harmonic waves through an infinite, hollow, circular cylinder using the three-dimensional equations of linear elasticity was carried out by Gazis [41] in 1958, and there were several related publications by Gazis, Herrmann and Mirsky for the remainder of the decade [42, 43, 84, 85]. These articles focus attention on the vibrations of thick-walled cylinders [41–43], as well as some corrections and errata [43, 84].

The approximate theories, proposed by Herrmann and Mirsky [47, 48, 83] and Naghdi and co-workers [30, 91, 92], govern the free vibrations of infinitely long, hollow, elastic cylindrical shells but are mainly based on assumptions that restrict validity to shells whose thickness is small compared with the inner radius, see McNiven *et al.* [79]. These latter models are also mainly restricted to low frequency regimes and could be used to analyse flow in arteries. The subsequent studies on thick-walled cylindrical shells [82, 84] were also primarily applicable to low frequency regimes, but they were restricted to the analysis of the longitudinal mode.

An alternative approach was developed in a two-part publication by McNiven *et al.* [78, 79] in the 1960s. The theory was designed to be applicable to a much wider range of cylinder thicknesses, from thin-walled hollow rods to thick-walled cases, and even to the solid cylinder in the limit. The first paper [79] takes into account the coupling between the lowest three modes (longitudinal, lowest radial and lowest axial shear). The results comparing the frequency spectra for the approximate model with those of the exact three-dimensional theory reported by Gazis [41, 42], for various wall thicknesses and physical parameters, showed excellent agreement [79].

The theory developed in [78, 79] followed the method utilised for solid rods by Mindlin and McNiven [81]. It was based on expansions of the displacements as a series of orthogonal polynomials that retain only the terms representing the lowest three modes. The discrepancy, arising from the omission of higher order terms, was offset by introducing adjustment factors chosen such that the behaviour of the first three branches of the exact frequency spectrum is matched at long wavelengths. The quality of the approximate theory [78, 79], as with any, is best judged by how well the frequencies and the vibration modes match, for a given propagation constant, to the corresponding frequencies from the exact three-dimensional theory [78]. Frequency spectra were obtained and the approximate theory was effective in reproducing important physical features of the exact three-dimensional theory [65] for the first three modes.

The extension by Kumar and Stephens [65] investigated the dispersion of flexural waves in circular, cylindrical shells of various wall thickness, using exact three-dimensional theory and shell theory. Both real and purely imaginary branches were analysed and the effects of varying the Poisson ratio, and the ratio of inner to outer shell radii, were studied. This work was also related to the earlier article by Kumar [62], for the case of flexural vibrations of fluid-filled circular cylindrical shells. Kumar went on to consider the finite case with a series of related publications.

The two-part study by Kumar and Chandra [20, 64] for axially symmetric vibrations of finite-sized cylindrical shells (with various wall thicknesses) was published in 1976 and 1977. This was followed by the two-part report for flexural vibrations by the same authors [21, 22]. The first pair of papers produced aspect ratio curves, residual stresses and displacements for various wall thicknesses. The motion of the shell was assumed to be axially symmetric in both cases, but it was assumed to be symmetric about the central plane in part one, [64], and anti-symmetric about the central plane in part two [20].

Both papers utilised the exact three-dimensional linear elasticity theory. The flexural case was studied in a similar way [21, 22], with frequency-aspect ratio curves obtained for finite, isotropic, cylindrical shells of varying wall thickness. Part one [21] assumed symmetric motion about the central plane, whereas the follow-up [22] considered the case of anti-symmetric motion about the central plane.

Interesting extensions of the literature included a study by Fuller [38] of the effects of discontinuities in the pipe walls. For the case of flexural waves, theoretical curves of transmission loss were obtained for various wavenumber and wave types, as functions of frequency [38]. Key factors influencing the propagation of waves through wall discontinuities were found to include:

- Material stiffness;
- Frequency;
- Radial vibration amplitude.

Some more recent works include a review of various shell theories without fluid by Farshidianfar and Oliazadeh [34] and a pair of papers by Zhang *et al.* [125, 126], for which a wave propagation method was implemented to analyse coupled structural-acoustic systems of finite fluid-filled cylindrical shells.

In biomechanics, many computational models were performed for haemodynamics, but only a limited number of investigations addressed the propagation of waves in stented blood vessels. The paper by Casciaro *et al.* [19] used one-dimensional patient-specific models to predict the effect on pulse wave reflections for certain endovascular cases. Even fewer studies investigated systems that exhibit a repetitive pattern in their geometry, with one example being the work by Papathanasiou *et al.* [96]. A recent paper by Jaganathan *et al.* [57] shows a comparison between different types of stents on the basis of their natural frequencies, and the analysis was performed for the metallic structure in isolation.

The collection of papers by Charonko and co-authors [24–26] combined mathematical modelling and experimental measurements to investigate the reflection of pressure waves in stented arteries. The first of these publications [26] describes a one-dimensional finite-difference model that was used to perform a parametric study of variations in stent and vessel properties; these included stiffness and length of stent, vessel radius and arterial wall thickness. The authors introduce a single non-dimensional parameter to describe the effect of all the factors listed above on wave reflections, with the emphasis on comparing the magnitudes of reflected pressure waves with and without stents.

Some other articles featuring stented artery modelling are discussed in the review by Hirschhorn *et al.* [49], specifically in their Section 10. Pulse wave propagation (PWP) is integral to the circulatory system; the body's large arteries are elastic and facilitate blood flow by responding to the pressure cycles initiated by the left ventricle of the heart and stents are believed to contribute to a reduction in PWP [49]. The review [49] cited one of the papers [36] featured in this thesis, see Chapter 3, where the models and explanations are expanded beyond the journal publication. As stated by [49], the results

of [36] illustrate why certain vessels respond better to stenting than others, and provide important insights to guide the orientation of stents to aid PWP. Another good source of relevant literature is the review by Karanasiou *et al.* [59] which summarises biomechanics, biomaterials and insights from computational modelling for stents.

One well-known biomechanical phenomenon is that the junctions between blood vessels act as scatterers, and reflection of acoustic waves from branched blood vessels is observed in routine measurements. For more details, the reader is advised to refer to the book by Caro *et al.* [14] and the review paper by Van de Vosse and Stergiopulos [116]. Accordingly, reflection of acoustic waves is expected whenever the properties of the arterial wall are altered. Another important aspect is compliance mismatch, which is described by Selvarasu *et al.* [108], and may arise due to the presence of a stent. The resultant localised haemodynamic effects were investigated in [108], which noted that the compliance mismatch is at its maximum at the proximal and distal ends of the stent. The main focus was the generation of non-physical wall shear stress. Three-dimensional, spatio-temporally resolved computational simulations of pulsatile flow were carried out for a simplified coronary artery, with physiologically relevant flow parameters [108].

Another important factor for modelling stented vessels is the consideration of atherosclerotic plaque. As described by Pericevic *et al.* [97] and Naghavi *et al.* [90], the plaque is a highly complex material, typically consisting of accumulated cells, lipids, calcium, collagen and inflammatory infiltrates. Understanding the mechanical behaviour of atherosclerotic plaque is critical for the prediction, treatment and prevention of cardiovascular diseases. An excellent review on the subject is provided by Topoleski and Stephen [113]. It is natural to consider first the material properties, but as explained in [113], plaques demonstrate huge variability and therefore it is an open research topic to narrow down both geometries and material parameters for simulations. Most biological tissues are unpredictable in their presentation for mechanical evaluation, and especially atherosclerotic plaque according to [113]. Numerous studies have been conducted to investigate the material and mechanical properties of plaque, including those by Barrett *et al.* [11], Chua *et al.* [29] and Lawlor *et al.* [67].

This thesis primarily focuses on carotid arteries, and the study [67] utilised experiments to determine the material characteristics of fresh carotid artery plaques. One of the motivations for [67] was the implication that mechanical forces during stent deployment were a critical factor in plaque fatigue and rupture which was reported by Cheng *et al.* in [28]. Tables, stress and strain plots are provided in [67] to inform simulations but the results are based on a small sample of patients.

A similar study was carried out by Barrett *et al.* [11]. The earlier work of Chua *et al.* [29] presented an analysis of the interactions between a stented artery and plaque using finite element simulations. The study included investigation of the post-expansion response of the stent in the presence of the plaque-artery system. The model assumed the arterial wall and plaque to both be linearly isotropic and nearly incompressible [29]. A subsequent paper by Pericevic *et al.* [97] analysed the influence of plaque composition on

arterial over-stretching and how this may impose damage to the vessel wall post-expansion of the stent.

The geometry of the majority of commercially available stents, which is described in the paper by Auricchio *et al.* [6], is based on a brand-specific pattern consisting of the repetition of a *primitive cell* along the circumference of the structure, thus yielding the *unit cell* of the system. The geometry and unit cell used for the models in this thesis are described in detail in Section 3.1.3. The deployed stent structure consists of the repetition of several unit cells along the axis of the vessel. These features suggest that a stented artery can be considered as a *periodic structure*, defined by a unit cell composed of the artery wall, the stent structure, and the blood; hence, the system can be modelled as a fluid-filled periodically reinforced cylinder with a flexible wall.

Periodic structures are known to exhibit special features when subjected to harmonic vibrations in terms of the propagation and attenuation of waves. A valuable technique to analyse the behaviour of periodic systems is the Bloch-Floquet analysis which was pioneered by Brillouin [12]. Its application to fluid-filled periodically reinforced cylinders constitutes a novel approach for the detection of reflected waves in stented arteries, in the absence of branching or any other sudden geometrical variation. The Bloch-Floquet analysis is used to obtain the deformation modes of the stented blood vessel in the time-harmonic pulsation regime, as shown in Figure 1.1 and in Chapter 3.

The Bloch-Floquet waves technique has been recently employed in many applications in order to understand the dynamic properties of periodic systems. Examples include bi-coupled periodic civil engineering structures such as bridges, pipelines and railways as reported in the studies by Carta *et al.* [15, 16]. Another recent paper by Carta *et al.* [18] used Bloch-Floquet analysis to investigate the suppression of vibrations for periodic arrays of fluid-filled tanks such as those in petrochemical plants or used to store water. Studies of periodically distributed cracks that arise in delaminating bi-material strips have also been carried out by Mishuris and co-workers [86, 117, 118]. An important observation made in [15] is that some structures composed of repeating units, although finite in reality, may be analysed as infinite systems for which Bloch-Floquet analysis is effective. In particular, in the studies by Haslinger *et al.* [46] and Brun *et al.* [13] it has been shown that there is a link between the dispersion properties of an infinite periodic system and the transmission problem for the corresponding finite system.

The effects of propagation and attenuation of waves on localisation of strain and reduction of flow velocity can be investigated by means of the frequency response analysis, which is utilised in this thesis for an assembly of a finite number of unit cells. In addition, a transient regime analysis is performed for the finite-length stented artery, which shows in detail how the flow is affected by the reinforcements. In the transient computations, the fluid is described by the complete Navier-Stokes equations and full fluid-structure interaction is taken into account.

Two main branches of analysis are presented throughout this thesis:

- the Bloch-Floquet waves analysis for a periodically stented artery;

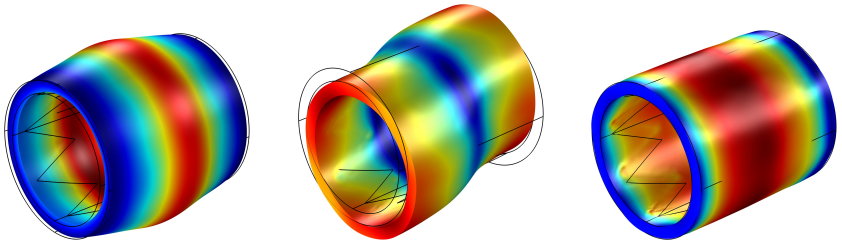

(a) *Axisymmetric mode.* (b) *Flexural mode.* (c) *Torsional mode.*

Figure 1.1: Representative shapes of some of the deformation modes observed in the unit cell with a stent.

- the frequency response analysis linked to the transmission/reflection problem for the case of a stented region of finite length.

Chapter 3 also features a transient regime analysis for a finite-length stented artery with nonlinear viscous fluid. Each of the analysis techniques assumes the blood to be an acoustic fluid.

Biomedical acoustics is a well-developed research area encompassing the investigation of acoustic and ultrasonic wave interaction with biological systems of soft tissues, bones and organs. There are numerous established concepts and ideas used in medical diagnosis techniques and for a range of technical applications. One specific topic of interest is acoustic wave propagation in biological materials such as arterial tissue. As is often the case for the analysis of acoustic waveguides, mathematical modelling is very important in biomechanical problems that include pulsating flow.

Analytical models and numerical simulations presented in [35, 55, 80, 96] cover pulsating blood flow for an unstented artery. All four of these articles consider one-dimensional blood flow models, with three of them applying linear analysis whilst the paper by Formaggia *et al.* [35] presents a suite of one-dimensional non-linear systems to model blood pulse propagation in compliant arteries. The effects of including inertia, longitudinal pre-stress and viscoelasticity are all included within the models. Branching and possible discontinuities in the wall properties are also investigated in [35]. The effects of branching and vessel permeability are also included in the earlier work of Hughes and Lubliner [55] from the 1970s. The more recent paper by Melicher and Gajdošík [80] considers one-dimensional blood flow models applicable to larger arteries, with its numerical solution obtained using a moving grid method, rather than the standard Taylor-Galerkin scheme.

The biomechanical studies of Alastruey *et al.* [2, 3] used experimental measurements as a basis for a one-dimensional viscoelastic non-linear model of the human arterial network. The first mentioned paper [2] tested the accuracy of the non-linear one-dimensional blood flow model in large arteries, by comparing wave measurements in a silicone tree with the numerical predictions. Inclusion of viscoelastic contributions for the wall demonstrated some reduction in relative errors. The subsequent study [3] concentrated on physical determining factors of the arterial pulse waveform. Properties such as local elasticity

and viscosity of the arterial wall, total compliance (zero stiffness) and net peripheral resistance of the systemic arterial tree are impossible to measure *in vivo* [3], but can be computed from pressure, flow and wall displacement measurements obtained from *in vivo* experiments.

A linear analysis of the one-dimensional equations of blood flow in viscoelastic arteries was carried out by Alastruey *et al.* [3] to investigate the effects of blood viscosity, flow inertia, wall viscoelasticity, total arterial compliance, net resistance, peripheral outflow pressure and flow rate (at the aortic root) on pulse wave propagation. These dynamic factors are described in detail by standard biomechanics books mentioned earlier in the introduction, including [32, 56, 94].

It should be noted that the wall of a healthy blood vessel is a highly adaptable, nonlinear system. Thus, in order to introduce a universal mathematical approach, that system would best be described by non-linear partial differential equations, whose coefficients depend on both spatial and temporal variables. However, an unhealthy (clogged) or stented blood vessel loses much of its flexibility as noted by Back *et al.* in [8] and so linearised approaches may be adopted to provide valuable insights.

Chapter 2 presents underlying theoretical background material used throughout the research, and consists of sections on wave propagation, Bloch-Floquet analysis in periodic structures, reflection-transmission methods, finite element methods and Mathieu's equation.

In Chapter 3, an extended version of the author's publication [36], three approaches are combined: the first one uses the Bloch-Floquet framework applied to an infinite periodic system, the second method is based on the transmission analysis of a finite-thickness structured interface and the third features a transient regime analysis for a finite-length stented artery. This combination of approaches is new for the dynamic response analysis of blood vessels, and it uncovers important phenomena attributed to transitional regimes where pulsating flow changes rapidly and hence higher-order harmonics occur. The Bloch-Floquet method is extended to the case of arteries containing atherosclerotic plaque in Chapter 4.

The analytical nature of the approach, in conjunction with transient simulations, is used to effectively identify the values of parameters leading to the transitional regimes, which may be linked to vascular blockages in multi-scale stented systems. The vibration eigenmodes and dispersion curves are obtained using fully three-dimensional finite element methods (FEM). Details related to parameter values for the artery tissue, blood and stents are provided in Sections 3.1.3, 3.1.4. The meshing and time steps used in the finite element domains are optimised with respect to wavelength and wave speeds. General concepts of finite element analysis are provided in Section 2.5 in the background and underlying theory Chapter 2.

In Chapter 5, based on the recent paper by Frecentese *et al.* [37], a simplified one-dimensional model is developed as an approximation to the full three-dimensional formulation introduced in Chapter 3. It follows previous work published by Papathanasiou

et al. [96], for a general Bloch-Floquet analysis of a solid-fluid interaction problem. The novel feature in this chapter of the thesis is the introduction of the stent for the one-dimensional model, for which different material parameters are defined. In particular, homogenisation approximations are explored, where a stented region is described by differential equations with variable coefficients. Conclusions and future work are discussed in Chapter 6.

Chapter 2

Theory and background

2.1 Wave propagation in arteries

As described in the book by Caro *et al.* [14], when blood is ejected from the heart during systole, the pressure in the aorta and other large arteries rises, and then during diastole it falls again. The pressure rise is associated with outward motions of the walls, and they subsequently recover their shape because they are elastic. This process occurs during every cardiac cycle, and it can be seen that elements of the vessel walls oscillate cyclically, with a frequency of oscillation equal to that of the heartbeat. The blood also flows in a pulsatile manner, in response to the pulsatile pressure. In fact, a pressure wave is propagated throughout the whole system of arteries, known as the arterial tree.

In particular, as blood is pumped into the entrance of the aorta, pressure increases there and the vessel wall becomes stretched. As the rate of cardiac ejection naturally slows down, the pressure begins to drop and the distended wall returns to its equilibrium position. However, the fluid continues moving, due to its inertia, after the driving pressure difference has fallen. Thus, some of the artery wall extends beyond its equilibrium position, and an oscillatory cycle is initiated. Simultaneously, the adjoining section of the arterial wall becomes distended and as it springs back, the fluid ejected distends a further section which recoils, and so on.

The propagation of this disturbance is a pressure wave, and it is analogous to a wave that propagates along a stretched string. An important factor is that there is a balance between the restoring force, linked to the elasticity of the artery walls, and inertia, mainly due to the blood albeit with a small contribution from the wall itself. The pressure wave may propagate in either direction, but it is well known that in systemic arteries, it primarily originates in the heart and travels distally.

Another type of motion is associated with the pressure wave: radial wall disturbances cause some longitudinal motions of the vessel wall as it is stretched or compressed. However, these are secondary and have a negligible impact on the propagation of the pressure wave. One may also imagine an alternative type of wave where the oscillatory wall motions are longitudinal which, in turn, drive longitudinal fluid motions in the boundary layer due to viscosity, thereby providing inertia.

The consequences of pulsatile blood flow can be modelled using the laws of classical mechanics. Many theoretical and experimental studies have been published to describe pulsatile flow through the arterial tree. An example is the Moens-Korteweg relationship, which was derived for an inviscid fluid in an infinitely long, thin-walled elastic tube. This model contains no viscous terms but the momentum equations still contain non-linear convective acceleration terms although these can be neglected as a first order approximation as described in the book by Chandran *et al.* [23]. The well-known Moens-Korteweg equation expresses the speed of pressure wave propagation through a thin-walled elastic tube that contains an incompressible, inviscid fluid. The wave speed is proportional to the tube's modulus of elasticity and to the ratio of the tube's thickness and radius.

Womersley [121, 122] published several papers on the theoretical analysis of blood flow through arteries. His models considered unsteady flow of incompressible, Newtonian fluid through elastic tubes and the results were expressions for velocity profiles in the cross-section of the tube. Morgan and Kiely [87] also published work on viscous blood flow through arteries. The modelling in this thesis assumes incompressible, inviscid fluid for the blood. All the details are provided in the next section and in Chapter 3.

2.2 Derivation of the one-dimensional model

Wave propagation in blood vessels is mainly associated with the displacement of the arterial wall (due to its elasticity) in response to the motion of pressure/velocity waves as blood flows through the artery. In order to model this phenomenon, a system of partial differential equations describing fluid-solid interaction must be derived and solved simultaneously, as described in detail by Rubenstein *et al.* in [103], and summarised in what follows. An important concept is the intrinsic fluid-solid interaction, such that fluid forces impact the wall and, in turn, the elastic wall imparts responsive forces.

A blood vessel is considered to be a tube (i.e. cylindrical and straight) with mechanical properties that are homogeneous and elastic. Furthermore, it is assumed that the fluid is incompressible, inviscid and its motion is relatively slow. The application of a pressure pulse at one end of the blood vessel results in a geometric change in the vessel, and the pulse propagates, with a specific speed, along the length of the tube. In many cases, the wavelength is much larger than the diameter of the tube; such an assumption enables one to model the flow velocity as one-dimensional, as used in Chapter 5 here. The combination of these assumptions and the use of the Navier-Stokes and continuity equations are implemented to determine the speed of wave propagation within the artery.

The analysis begins with the forces that act on the blood vessel as the pressure pulse propagates through the vessel. It is assumed that the forces balance in the y-direction (see Figure 2.1). In the x-direction, the summation of the pressure forces is given by

$$\sum F_x = p_{inlet} A_{inlet} - p_{outlet} A_{outlet} + p_{walls} A_{walls} \,, \tag{2.1}$$

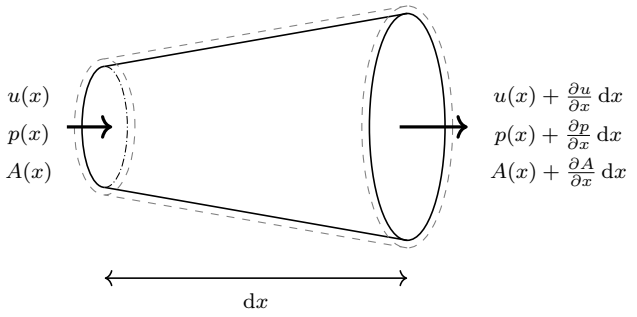

Figure 2.1: Wave propagation within a deformable homogeneous artery.

which is expressed mathematically as

$$p(x)A - \left[p(x) + \frac{\partial p}{\partial x}dx\right]\left[A + \frac{\partial A}{\partial x}dx\right] + p(x)\frac{\partial A}{\partial x}dx = -A\frac{\partial p}{\partial x}dx\,, \tag{2.2}$$

provided that the second order derivatives are ignored. Note that A is the cross-sectional area of the tube and p is the pressure. Applying Newton's second law of motion, the resultant force acting on a differential element (the right-hand side of (2.2)) is equal to the product of its mass and acceleration. In equation form, this may be written as

$$-A\frac{\partial p}{\partial x}dx = (\rho A dx)\left(\frac{\partial u}{\partial t} + u\frac{\partial u}{\partial x}\right)\,, \tag{2.3}$$

where ρ is the density, and u is the flow velocity. Rearranging equation (2.3),

$$\frac{1}{\rho}\frac{\partial p}{\partial x} + \frac{\partial u}{\partial t} + u\frac{\partial u}{\partial x} = 0\,, \tag{2.4}$$

which is a simplified form of the Navier-Stokes equation. The principle of conservation of mass applied to the differential element must take into account the increase in area of the element during an infinitesimal interval of time. Assuming that the density remains constant throughout the entire element (the fluid is assumed to be incompressible), the conservation of mass states that

$$uA = \left(u + \frac{\partial u}{\partial x}dx\right)\left(A + \frac{\partial A}{\partial x}dx\right) + \frac{\partial A}{\partial t}dx\,, \tag{2.5}$$

which, after expansion and neglecting second order terms, produces

$$uA = uA + u\frac{\partial A}{\partial x}dx + A\frac{\partial u}{\partial x}dx + \frac{\partial A}{\partial t}dx\,. \tag{2.6}$$

Rearranging (2.6) yields

$$u\frac{\partial A}{\partial x} + A\frac{\partial u}{\partial x} + \frac{\partial A}{\partial t} = 0\,, \tag{2.7}$$

and applying the chain-rule, the above equation may be written as

$$\frac{\partial A}{\partial t} + \frac{\partial}{\partial x}(uA) = 0\,. \tag{2.8}$$

To determine the wave propagation in the blood vessel, the material properties of the elastic arterial wall are related to the properties of the fluid. It is assumed that changes in the radius (r_i) of the blood vessel are linearly proportional to the blood pressure (p) acting on the vessel wall, according to the following relationship:

$$r_i = r_{i,0} + \alpha p \,, \tag{2.9}$$

where $r_{i,0}$ is the radius of the blood vessel at zero external pressure and α is a constant that describes material properties of the artery.

Recalling that the fluid velocity is relatively slow, the product of the velocity and its rate of change with respect to the spatial coordinate is negligible and so equation (2.4) becomes

$$\frac{1}{\rho}\frac{\partial p}{\partial x} + \frac{\partial u}{\partial t} = 0 \,. \tag{2.10}$$

Substituting the area $A = \pi r_i^2$ into (2.8), the equation is expanded in the form:

$$0 = \frac{\partial \left(\pi r_i^2\right)}{\partial t} + \frac{\partial}{\partial x}(u\pi r_i^2) = 2\pi r_i \frac{\partial r_i}{\partial t} + \pi r_i^2 \frac{\partial u}{\partial x} + u\pi \frac{\partial r_i^2}{\partial x} = \pi r_i^2 \left(\frac{2}{r_i}\frac{\partial r_i}{\partial t} + \frac{\partial u}{\partial x}\right) , \tag{2.11}$$

where second order terms have been neglected. Substituting (2.9) into (2.11), and for non-trivial solutions it follows

$$0 = \frac{2}{r_i}\frac{\partial}{\partial t}\left(r_{i,0} + \alpha p\right) + \frac{\partial u}{\partial x} = \frac{2\alpha}{r_i}\frac{\partial p}{\partial t} + \frac{\partial u}{\partial x} \,. \tag{2.12}$$

It will be assumed that the changes in the radius are too small compared with $r_{i,0}$.

To solve this in the form of a wave equation the temporal derivative of (2.12) is subtracted from the spatial derivative of (2.10) such that

$$\frac{\partial^2 p}{\partial x^2} - \frac{1}{c^2}\frac{\partial^2 p}{\partial t^2} = 0 \,, \tag{2.13}$$

where the wave speed is expressed in the form

$$c = \sqrt{\frac{r_i}{2\alpha\rho}} \,. \tag{2.14}$$

2.3 Bloch-Floquet waves in periodic structures

Bloch-Floquet analysis is a useful technique for investigating periodic systems. The underlying concept is a repeating elementary cell, from which the dynamic properties of the whole system may be obtained. The approach is adopted here in Chapters 3-5 to analyse a stented artery which may be considered as a periodic structure consisting of repeating units. The application of Bloch-Floquet analysis was formulated for several classes of problems in the classical book by Brillouin [12] and more recently, by Kittel [60]. Many engineering studies have also demonstrated the effectiveness of the technique for real structures such as bridges, pipelines, railways, fluid-filled tanks [13, 15, 17, 18, 46].

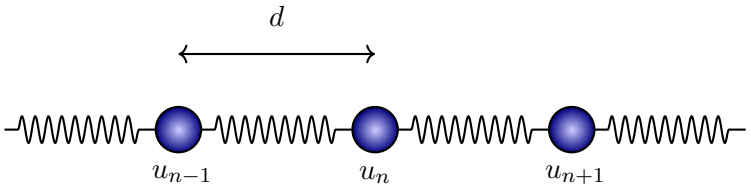

(a) *Periodic spring-mass chain.*

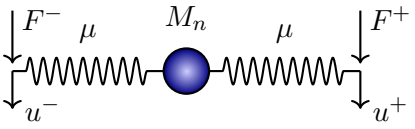

(b) *Unit cell.*

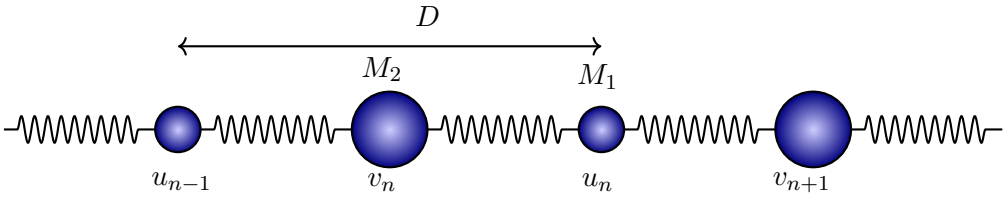

(c) *Periodic spring-mass chain containing two types of masses.*

Figure 2.2: Spring-mass systems to illustrate Bloch-Floquet waves in periodic structures. The size of the elementary cell is given by d in part (a) and (b) , and by D in part (c). The stiffness of the spring is denoted by μ.

The great advantage of the Bloch-Floquet method is that the complexity of the problem is reduced to the study of the elementary cell and implementation of quasi-periodicity conditions to connect all the cells within the system. Three cases are presented here to illustrate the technique, which is applied to more complicated problems in Chapters 3-5. The illustrative examples in this Chapter are based on those described in the book by Movchan *et al.* [89]:

1. infinite lattice of rigid particles with the same mass connected by massless springs,
2. infinite lattice of rigid particles with different mass connected by massless springs,
3. infinite lattice of elastic rods of different stiffness.

2.3.1 One-dimensional lattice of identical particles

Consider an infinite lattice of rigid particles connected by massless springs. All the particles have the same mass M. The distance between neighbouring masses is set to be d, and the stiffness of springs is assumed to be μ. The coordinate position of the particle n is given by $x_n = nd$. The system described is shown in Figure 2.2a. Let u_n be the displacement of the nth particle within the chain. The equations of motion then take the form

$$M\ddot{u}_n = \mu(u_{n+1} - u_n) - \mu(u_n - u_{n-1}) = \mu(u_{n+1} + u_{n-1} - 2u_n) \ . \tag{2.15}$$

Assuming that the motion is time harmonic, that is $u_n(t) = U_n e^{-\mathrm{i}\,\omega t}$, then

$$-M\omega^2 U_n = \mu(U_{n+1} + U_{n-1} - 2U_n)\ . \tag{2.16}$$

Solutions are sought in the form of Bloch-Floquet waves, which satisfy the following relation

$$u_{n+q} = u_n e^{\mathrm{i}\,qdK}\,, \tag{2.17}$$

where K is called the Bloch parameter (or wavenumber). In the case of travelling waves,

$$U_n = U e^{\mathrm{i}\,nKd}\,, \tag{2.18}$$

with U a constant, and the equation of motion (2.16) becomes

$$-M\omega^2 U e^{\mathrm{i}\,nKd} = \mu(U e^{\mathrm{i}(n+1)Kd} + U e^{\mathrm{i}(n-1)Kd} - 2U e^{\mathrm{i}\,nKd})\,. \tag{2.19}$$

Rearranging and simplifying the equation results in

$$-M\omega^2 = \mu(e^{\mathrm{i}\,Kd} + e^{-\mathrm{i}\,Kd} - 2)\,. \tag{2.20}$$

Recalling that $2\cos(Kd) = e^{\mathrm{i}\,Kd} + e^{-\mathrm{i}\,Kd}$ then the equation of motion becomes

$$-M\omega^2 = 2\mu(\cos(Kd) - 1)\,. \tag{2.21}$$

A non-trivial solution U_n of (2.16) and (2.21) exists, provided ω and K satisfy the following dispersion relation

$$\omega^2 = 2\frac{\mu}{M}\left(1 - \cos(Kd)\right)\,, \tag{2.22}$$

whose non-negative roots have the form

$$\omega = 2\sqrt{\frac{\mu}{M}}\left|\sin\left(\frac{Kd}{2}\right)\right|. \tag{2.23}$$

A plot of the dispersion curve for ω versus K is shown in Figure 2.3 for specified values of μ, M and d. The irreducible and first Brillouin zones are illustrated using solid and dashed lines, respectively. The dispersion curve represents a periodic function of the wavenumber K with the period

$$K = \frac{2\pi}{d}\,. \tag{2.24}$$

The range of wave numbers may be restricted to the following interval

$$-\frac{\pi}{d} \le K \le \frac{\pi}{d}\,, \tag{2.25}$$

which is called the first Brillouin zone [12]. Using symmetry, all the required information is contained within $0 \le K \le \pi/d$, which is called the irreducible Brillouin zone and is

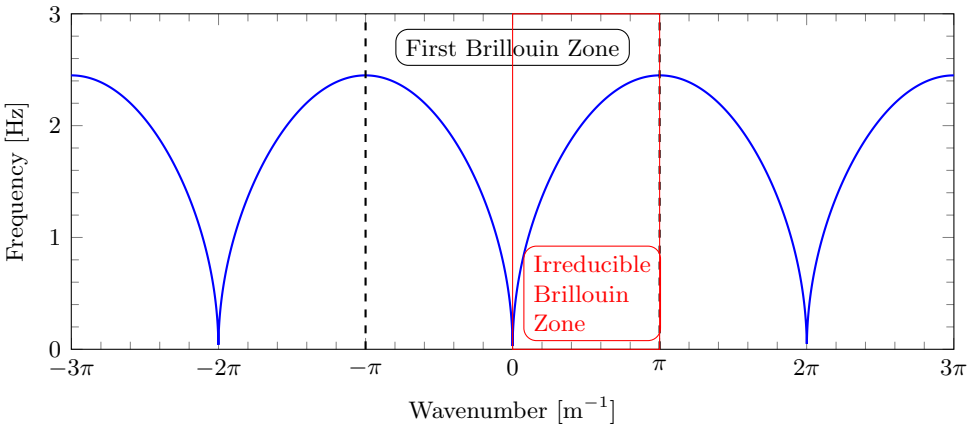

Figure 2.3: Dispersion curve for the periodic spring-mass system shown in 2.2a. The values used are $\mu = 1.5$, $M = 1$, $d = 1$.

illustrated in Figure 2.3.

2.3.2 Group velocity

Taking the limit $\omega d \to 0$, one obtains the continuum limit. Noting that

$$U_{n+1}/U_n = e^{iKd}, \tag{2.26}$$

and within the Brillouin zone $K_{max} = \pi/d$, in the continuum limit, $K_{max} \to \infty$.

The transmission velocity of a wave packet is called the group velocity, and it is given by

$$v_g = \frac{d\omega}{dK} = \sqrt{\frac{\mu}{M}} d \cos\left(\frac{Kd}{2}\right), \tag{2.27}$$

for $0 < K < \pi/d$. On the boundaries $K = \pm\pi/d$ of the Brillouin zone, $v_g = 0$; the solution U_n represents a standing wave with zero net transmission velocity, and $U_n = (-1)^n U$. Chapter 3 features analysis of standing waves for a stented artery.

In many physical applications, it is useful to have asymptotic approximations corresponding to the long wave limit. In particular, this will give the slope of the curve $\omega = \omega(K)$ as $K \to 0^+$, which is also referred to as the effective group velocity v_{eff} often used in homogenisation approximations of wave phenomena in structured media [12]. When $Kd \ll 1$, we have $\cos(Kd) \approx 1 - \frac{1}{2}(Kd)^2$, and hence $\omega^2 \approx \frac{\mu}{M}(Kd)^2$. Hence, $v_{\mathit{eff}} = \sqrt{\frac{\mu}{M}} d$, and thus v_{eff} is frequency-independent in this limit.

2.3.3 Two mass chain

Consider now the one-dimensional periodic lattice consisting of two types of particles, of different masses M_1 and M_2 with stiffness μ. The scheme is shown in Figure 2.2c. In this case, the elementary cell of the periodic lattice comprises two different particles, whose

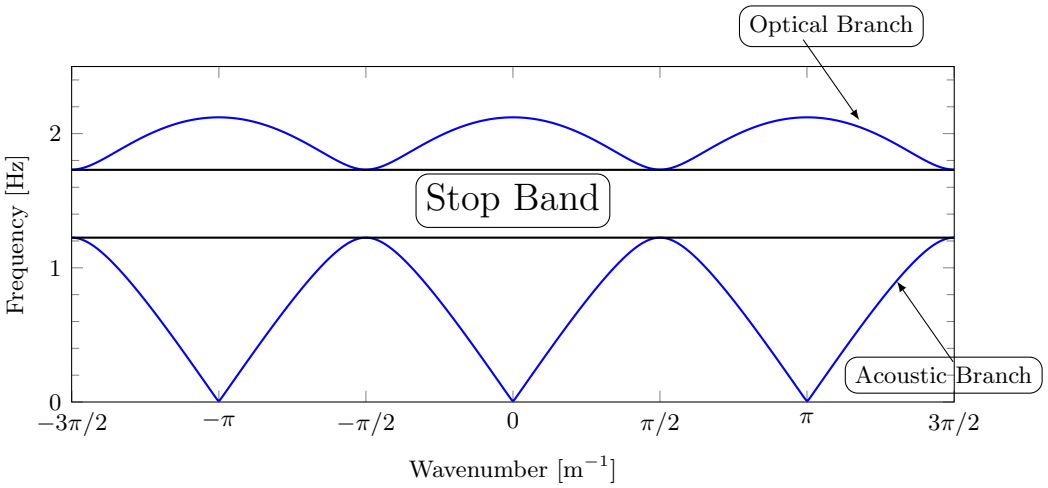

Figure 2.4: Dispersion curves for the periodic spring-mass system shown in 2.2c. The parameter values used are $\mu = 1.5$, $M_1 = 1$, $M_2 = 2$, $D = 2$.

displacements are denoted by u_n and v_n. Two equations of motion are required:

$$M_1 \frac{d^2 u_n}{dt^2} = \mu \left(v_n + v_{n-1} - 2u_n \right) , \tag{2.28a}$$

$$M_2 \frac{d^2 v_n}{dt^2} = \mu \left(u_{n+1} + u_n - 2v_n \right) . \tag{2.28b}$$

Let D be the size of the elementary cell (see Figure 2.2c), which is equal to the distance between the particles of the same mass. Travelling waves are defined by

$$u_n = U e^{\mathrm{i}(nKD - \omega t)} , \tag{2.29a}$$

$$v_n = V e^{\mathrm{i}(nKD - \omega t)} , \tag{2.29b}$$

where K is the wave number. Substituting into the equation of motion, then gives

$$\omega^2 \mu^{-1} M_1 U + V \left(1 + e^{-\mathrm{i}\, KD} \right) - 2U = 0 \tag{2.30a}$$

$$\omega^2 \mu^{-1} M_2 V + U \left(1 + e^{\mathrm{i}\, KD} \right) - 2V = 0 . \tag{2.30b}$$

This is a system of homogeneous linear algebraic equations with respect to U and V. There is a non-trivial solution if and only if the determinant of the matrix associated with the equations is equal to zero, i.e.

$$\frac{M_1 M_2}{\mu^2} \omega^4 - \frac{2 \left(M_1 + M_2 \right)}{\mu} \omega^2 + 2 \left(1 - \cos \left(KD \right) \right) = 0 . \tag{2.31}$$

This is the dispersion equation providing the relationship between the frequency ω and the wavenumber K. Equation (2.31) has explicit solutions of the form

$$\omega^2 = \mu \frac{M_1 + M_2 \pm \sqrt{\left(M_1 + M_2 \right)^2 - 2 M_1 M_2 \left(1 - \cos \left(KD \right) \right)}}{M_1 M_2} . \tag{2.32}$$

From equation (2.32) it is possible to deduce that the dispersion diagram shown in Figure 2.4 has two branches known as the "acoustic branch" (corresponding to the sign"-") and "optical branch" (corresponding to the sign "+"). Note that for the non-homogeneous system, when $M_1 \neq M_2$, there is a non-zero separation between the dispersion curves, known as a stop-band. The width of the stop-band can be computed by evaluating the frequencies at the end points of the Brillouin zone. At the boundary of the Brillouin zone, when $K = \pm\pi/D$, the roots of the dispersion equation are defined by

$$\omega^2 = \frac{\mu}{M_1 M_2}\left[M_1 + M_2 \pm |M_1 - M_2|\right] . \tag{2.33}$$

The stop-band width is calculated by finding the difference of the two frequencies obtained from (2.33).

2.3.4 Asymptotic approximation for continuous structured media

Consider a bi-material continuum system such as the propagation of out-of-plane shear elastic waves through a periodic array of homogeneous isotropic layers described in [88], as shown in Figure 2.5, or a one-dimensional periodic array of elastic rods of different stiffness E_j, $j = 1, 2$, and non-zero mass density [89]. The two problems share the same method of solution and here the second case is explained, following the analysis of [89].

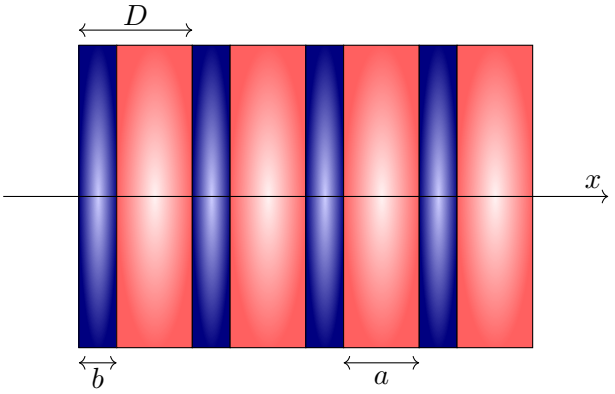

Figure 2.5: One-dimensional bi-material stratified periodic structure. The widths of the two layers are indicated by a and b, and D is the width of the elementary cell.

For simplicity, it is assumed that the linear mass density ρ is the same for all the elements of the structure. The elementary cell contains two types of elastic rods. The notations $S_1^{(n)} = (-b + nD, nD)$, and $S_2^{(n)} = (nD, a + nD)$, where n is integer, and $D = a + b$ is the total size of the elementary cell, are used.

Assuming time harmonic waves, with radian frequency ω, the amplitudes of the longitudinal displacements $U_j(x)$ satisfy the equations:

$$E_j U_j'' + \omega^2 \rho U_j = 0\,, \quad x \in S_j^{(n)}\,, \quad j = 1, 2\,. \tag{2.34}$$

A boundary condition of ideal contact at the interface between neighbouring rods implies continuity of both displacements and tractions, such that

$$U_1 = U_2\,, \quad E_1 U_1^{'} = E_2 U_2^{'}\,. \tag{2.35}$$

The solution is then sought in the class of Bloch-Floquet waves, which satisfy the following relation:

$$U_j(x+D) = e^{\mathrm{i}\,KD} U_j(x)\,, \quad j = 1,2\,, \quad |K| < \pi/D\,. \tag{2.36}$$

The general solution of (2.34) is given by

$$U_j = A_j e^{\mathrm{i}\,k_j x} + B_j e^{-\mathrm{i}\,k_j x}\,, \quad x \in S_j^{(n)}\,, \quad j = 1,2\,, \tag{2.37}$$

where A_j and B_j are constant coefficients and $k_j(\omega) = \omega\sqrt{\rho/E_j}$ are linear functions of the radian frequency ω for $j = 1, 2$. Application of the interface conditions (2.35) and Bloch-Floquet conditions (2.36), for displacements within the elementary cell, lead to a homogeneous system of linear equations for the coefficients A_j and B_j:

$$\mathbf{Q}(K,\omega) \begin{pmatrix} A_1 \\ B_1 \\ A_2 \\ B_2 \end{pmatrix} = 0\,, \tag{2.38}$$

where

$$\mathbf{Q}(K,\omega) = \begin{bmatrix} 1 & 1 & -1 & -1 \\ E_1 k_1 & -E_1 k_1 & -E_2 k_2 & E_2 k_2 \\ -e^{\mathrm{i}(KD-k_1 b)} & -e^{\mathrm{i}(KD+k_1 b)} & e^{\mathrm{i}\,k_2 a} & e^{-\mathrm{i}\,k_2 a} \\ k_1 e^{\mathrm{i}(KD-k_1 b)} & -k_1 e^{\mathrm{i}(KD+k_1 b)} & -\frac{E_2 k_2}{E_1} e^{\mathrm{i}\,k_2 a} & \frac{E_2 k_2}{E_1} e^{-\mathrm{i}\,k_2 a} \end{bmatrix}. \tag{2.39}$$

This system has a non-trivial solution for zeros of the determinant of the matrix $\mathbf{Q}$:

$$\det \mathbf{Q}(K,\omega) = 0\,, \tag{2.40}$$

which relates the frequency to the Bloch parameter K, and hence represents the dispersion equation for Bloch-Floquet waves that propagate within the periodic system. Introducing the notation $\epsilon = E_1/E_2$, it follows that $k_2 = k_1\sqrt{\epsilon}$. Then, the dispersion relation (2.40) leads to

$$(\epsilon+1)\sin(k_1 b)\sin\left(k_1 a\sqrt{\epsilon}\right) - 2\sqrt{\epsilon}\left[\cos(k_1 b)\cos\left(k_1 a\sqrt{\epsilon}\right) - \cos(KD)\right] = 0\,. \tag{2.41}$$

The assumptions $\epsilon \ll 1$ and $k_1 b \ll 1$ imply that the structure has a high contrast in the stiffness of its phases, and the length b of one of the elastic rods in the elementary cell is relatively small. Then the corresponding sine and cosine terms of (2.41) may be expanded into power series. After truncation, a polynomial in powers of ω is obtained.

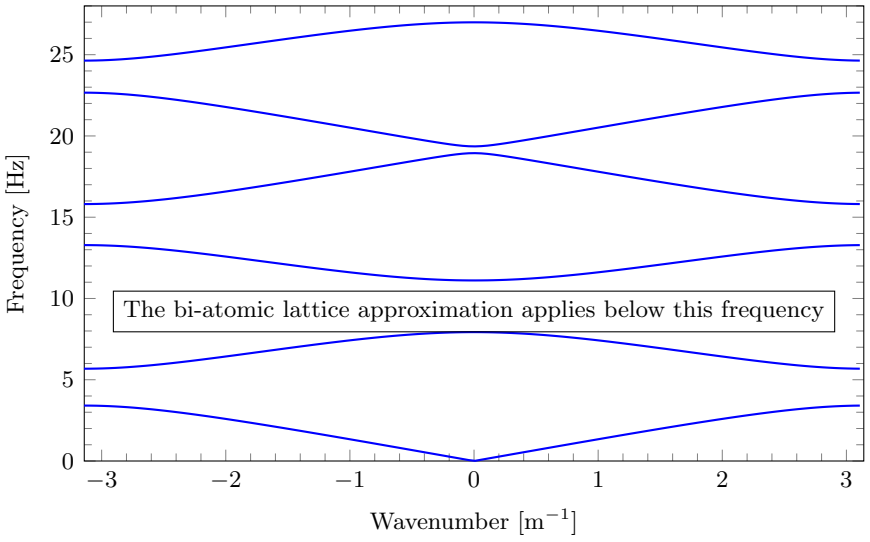

Figure 2.6: Dispersion diagram for Bloch-Floquet waves in the high-contrast bi-material periodic system. The parameters used are $D = 1$, $a = b = 0.5$, $\epsilon = 0.1$, $\rho = 1$.

Retaining the terms up to the fourth power of the frequency, the following approximate dispersion equation is obtained:

$$\omega^4 \Pi - \omega^2 \Theta + 2\left(1 - \cos\left(KD\right)\right) = 0\,, \tag{2.42}$$

where the terms Π and Θ are positive-valued and have the form:

$$\Pi = \frac{\rho^2 E_1^2}{12}\left(\epsilon a^2 + 2\epsilon b a + b^2\right)\left(\epsilon a^2 + b^2 + 2ba\right)\,, \tag{2.43a}$$

$$\Theta = \frac{\rho}{E_1}\left(a + b\right)\left(\epsilon a + b\right)\,. \tag{2.43b}$$

Recall that the dispersion equation for the discrete system, consisting of a one-dimensional array of masses M_1, M_2 connected by elastic springs with stiffness E, is given by (2.31) which has the same structure as (2.42). Hence, a discrete lattice may be used to approximate a high-contrast periodic continuous medium to derive its dynamic response for the low frequency regime. This discrete model (2.31) is characterised by the two parameters M_1/E and M_2/E so that the two dispersion equations become identical when

$$\Pi = \frac{M_1 M_2}{E^2}\,, \quad \Theta = \frac{2\left(M_1 + M_2\right)}{E}\,. \tag{2.44}$$

Note that the dispersion relation for the bi-material continuum (2.41) is a transcendental equation and so has an infinite number of solutions. In contrast, the lattice approximation model covers only the first two dispersion curves, nearest to the origin. Figure 2.6 illustrates solutions of the full dispersion equation (2.41) for the high-contrast two-phase system, and also indicates the regime where the lattice approximation may be applied (the first two dispersion curves).

2.3.5 Periodic stent structure

A stent is a tube that is inserted into the lumen of an atherosclerotic blood vessel to open it up. Many types of stent are used for different purposes, for example coronary stents, vascular stents, stent grafts, ureteral stents, etc. Vascular stents are commonly used to treat peripheral and cerebrovascular disease. The arteries most frequently treated are the carotid, iliac and femoral. Due to the external compression and mechanical forces that act at these locations, flexible stent materials such as nitinol are used.

Vascular self-expanding nitinol stents are usually between $5 - 10\,\text{mm}$ in diameter and can be between $20 - 200\,\text{mm}$ in length. Typically they consist of several coils connected by links and they present a structure that can be considered periodic due to the pattern repetition. Therefore, Bloch-Floquet analysis, although applicable to infinite systems, gives insight about dispersion properties of pulse waves in a finite portion of stented arteries, similar to other finite systems reported in [13] and [46]. Depending on the stent geometry, a specific unit cell is defined for the Bloch-Floquet analysis. One important feature related to group velocity is when it is zero, for which standing waves occur in the blood vessel. This type of wave is undesirable because it disrupts blood flow and causes changes in pressure.

Elastic systems, in general, possess resonant frequencies, which can be obtained using eigenfrequency analysis. Such frequencies are often initiated by external forces and for a human body, these may be linked to factors such as walking, running, riding a motorcycle, using heavy machinery, all of which produce vibrations. For example, public transportation for cases of rough street surface, speed bumps, and old railway tracks induce vibrations that range between 1 Hz and 20 Hz or wider, as reported by Argani *et al.* [5]. This range of frequencies is relevant for the cases of overlapping (see Chapter 5) or clusters of stents (see Chapter 3). In these scenarios, stop-band regions may arise meaning that pulse waves are likely to be significantly attenuated leading to possible disruption of blood flow. Stop-band regimes are affected by many parameters such as number of coils, number of links between the coils, and location, geometry and density of plaque.

2.4 Reflection-transmission

Consider a similar system to that of Section 2.3.4, but with a finite number of sequentially connected elastic rods aligned with the x-axis. The book [89] describes this as a "structured interface" and states that the rods may have different lengths, densities and stiffness. A wave that propagates in the positive direction of the x-axis arrives at, and interacts with, the interface. Some of the energy is reflected, whilst the remaining energy is transmitted through the interface, the percentage of which is frequency-dependent.

In the case of a repeating pattern of a sufficiently large number of rods, it becomes possible to associate this interface with the analysis of Bloch-Floquet waves and their dispersion properties, as explained by Lekner [69] and by Movchan *et al.* [89]. However,

when the number of rods is relatively small, i.e. the interface has a finite thickness, the analysis requires a different approach that focuses on trapped modes; their existence within the structured interface may modify and enhance transmission effects. An effective tool for such investigations is the transmission matrix technique [69], which is described in the following section. This technique is used in 3 for both the case of a portion of stented artery and for the case of a cluster of stents. In addition, it is used in 5 for the one-dimensional model and the case of overlapping stents.

2.4.1 Transmission matrix technique

The amplitude of the displacement for time-harmonic motion with radiant frequency ω is denoted by u and satisfies the following ordinary differential equation:

$$E\frac{d^2u}{dx^2}(x) + \rho\omega^2 u(x) = 0\,, \tag{2.45}$$

where ρ is the mass density and E is the stiffness of a single rod. The solution may be expressed in terms of complex amplitudes A and B:

$$u(x) = Ae^{\mathrm{i}\,Kx} + Be^{-\mathrm{i}\,Kx}\,, \tag{2.46}$$

where

$$K = \omega c\,, \quad c = \sqrt{\frac{\rho}{E}}\,. \tag{2.47}$$

Consider a one-phase interface between $x = x_0$ and $x = x_1 = x_0 + D$, where D is a small increment. Then, the displacements and tractions are related by

$$\begin{pmatrix} u(x_1) \\ E\frac{\partial u}{\partial x}(x_1) \end{pmatrix} = \mathbf{T}\begin{pmatrix} u(x_0) \\ E\frac{\partial u}{\partial x}(x_0) \end{pmatrix}\,, \tag{2.48}$$

where, referring to equation (2.46), the transmission matrix $\mathbf{T}$ is defined by [69]

$$\mathbf{T} = \begin{bmatrix} \cos(KD) & \frac{\sin(KD)}{EK} \\ -EK\sin(KD) & \cos(KD) \end{bmatrix}\,. \tag{2.49}$$

Note that KD is known as the phase increment. The eigenvalues of the transmission matrix $\mathbf{T}$ are straightforwardly determined to be

$$\cos(KD) \pm \sqrt{\cos^2(KD) - 1} = e^{\pm\,\mathrm{i}\,KD}\,. \tag{2.50}$$

Similarly, a discrete interface, which consists of two springs of stiffness μ and mass M, may be analysed using transmission matrix methods. The spring-mass lattice is a mono-coupled system since each mass has only one degree of freedom and the coupling between two adjacent cells is given only by the force exerted by the spring. As a consequence, in this case the transfer matrix is a two-by-two matrix that relates the vector $\mathbf{u}^+$ of

displacement and the force at the end of each cell to the vector $\mathbf{u}^-$ at the beginning of the cell shown in Figure 2.2b:

$$\mathbf{u}^+ = \begin{pmatrix} u^+ \\ F^+ \end{pmatrix} = \mathbf{T}_n \mathbf{u}^- = \begin{bmatrix} T_{11}^{(n)} & T_{12}^{(n)} \\ T_{21}^{(n)} & T_{22}^{(n)} \end{bmatrix} \begin{pmatrix} u^- \\ F^- \end{pmatrix} , \tag{2.51}$$

where $n = 1, \cdots, N$ is an index denoting the nth position of the mass. According to Newton's law of motion,

$$F^+ + F^- = M \frac{d^2 u}{dt^2} , \tag{2.52}$$

where

$$F^+ = \mu \left(u^+ - u \right) , \tag{2.53}$$

and

$$F^- = \mu \left(u - u^- \right) . \tag{2.54}$$

Assuming time-harmonic motion, equation (2.52) becomes

$$F^+ + F^- = -M\omega^2 u . \tag{2.55}$$

Inserting equations (2.55), (2.54), and (2.53) in the system (2.51), the following set of equations is obtained

$$u^+ = u^- \left(1 - \frac{M\omega^2}{\mu} \right) + F^- \left(\frac{2}{\mu} - \frac{M\omega^2}{\mu^2} \right) , \tag{2.56a}$$

$$F^+ = u^- \left(-M\omega^2 \right) + F^- \left(1 - \frac{M\omega^2}{\mu} \right) . \tag{2.56b}$$

In this case then, the transfer matrix $\mathbf{T}_n$ for the discrete interface is written in the following form

$$\mathbf{T}_n = \begin{bmatrix} 1 - \frac{M\omega^2}{\mu} & \frac{2}{\mu} - \frac{M\omega^2}{\mu^2} \\ -M\omega^2 & 1 - \frac{M\omega^2}{\mu} \end{bmatrix} . \tag{2.57}$$

The eigenvalues are:

$$1 - \frac{M\omega^2}{\mu} \pm \sqrt{\frac{M\omega^2}{\mu} \left(\frac{M\omega^2}{\mu} - 2 \right)} . \tag{2.58}$$

The algebraic dependence contrasts with the continuous one-phase interface case (2.50). It is also notable that the eigenvalues for the discrete case (2.58) become complex for sufficiently small values of ω, and are real for sufficiently large values, in particular when $\omega^2 > 2\mu/M$.

The power of the transmission matrix technique is that if an interface consists of several regions, whether continuous or discrete, placed together to form a stack, the overall transmission matrix is obtained by appropriate multiplication of the constituent transmission matrices that characterise each individual layer [69].

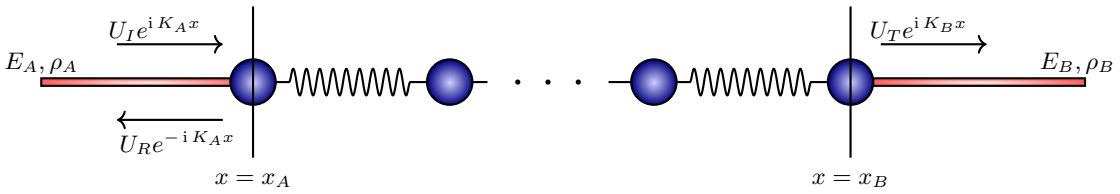

Figure 2.7: Representation of the transmission problem for a monatomic lattice located between two semi-infinite elastic rods of stiffness E_A and E_B, and mass densities ρ_A and ρ_B.

2.4.2 Reflection-transmission problem for non-uniform interface

To illustrate an application of the transmission matrix technique, consider the case of a monatomic lattice perfectly connected to two semi-infinite elastic rods, as shown in Figure 2.7. Recall that the equation of motion for a single elastic rod is given by (2.45). For this discrete-continuous system, there are two semi-infinite rods so index notation is adopted when writing the equation of motion for each rod:

$$E_j \frac{d^2 u_j(x)}{dx^2} + \rho_j \omega^2 u_j(x) = 0\,, \quad j = A, B\,. \tag{2.59}$$

Here E_A, E_B and ρ_A, ρ_B are, respectively, the elastic moduli and mass densities of the rods. The phase velocities are denoted as $c_A = \sqrt{E_A/\rho_A}$ and $c_B = \sqrt{E_B/\rho_B}$, and the impedances of the two rods, as $Q_A = E_A\omega/c_A$ and $Q_B = E_B\omega/c_B$.

The displacement field for rod A is represented by the sum of incident and reflected waves:

$$u_A\,(x) = U_I e^{\mathrm{i}\,K_A x} + U_R e^{-\mathrm{i}\,K_A x}\,, \tag{2.60}$$

where $K_A = \omega/c_A$ is the wavenumber. The displacement field in rod B represents the transmitted waves and it is written as

$$u_B\,(x) = U_T e^{\mathrm{i}\,K_B x}\,, \tag{2.61}$$

where $K_B = \omega/c_B$ is the wavenumber. In order to derive the system of governing equations, the tensile stresses of the rods are defined by

$$\sigma_j = E_j \frac{du_j}{dx}, \quad j = A, B. \tag{2.62}$$

The system of equations is then written in matrix form:

$$\begin{aligned}\begin{pmatrix} u_B\,(x = x_B) \\ \sigma_B\,(x = x_B) \end{pmatrix} &= \begin{pmatrix} U_T e^{\mathrm{i}\,K_B x_B} \\ \mathrm{i}\,K_B E_B U_T e^{\mathrm{i}\,K_B x_B} \end{pmatrix} = \mathbf{T}_N \begin{pmatrix} u_A\,(x = x_A) \\ \sigma_A\,(x = x_A) \end{pmatrix} \\ &= \begin{bmatrix} T_{11}^{(N)} & T_{12}^{(N)} \\ T_{21}^{(N)} & T_{22}^{(N)} \end{bmatrix} \begin{pmatrix} U_I e^{\mathrm{i}\,K_A x_A} + U_R e^{-\mathrm{i}\,K_A x_A} \\ \mathrm{i}\,K_A E_A \left(U_I e^{\mathrm{i}\,K_A x_A} - U_R e^{-\mathrm{i}\,K_A x_A}\right) \end{pmatrix}. \end{aligned} \tag{2.63}$$

Note that the subscript becomes a superscript when writing the matrix $\mathbf{T}_N$ in component form.

The solution of the system yields expressions for the normalised reflection and transmission coefficients:

$$\frac{U_R}{U_I} = \frac{Q_A Q_B T_{12}^{(N)} + T_{21}^{(N)} + \mathrm{i}\left(Q_A T_{22}^{(N)} - Q_B T_{11}^{(N)}\right)}{Q_A Q_B T_{12}^{(N)} - T_{21}^{(N)} + \mathrm{i}\left(Q_A T_{22}^{(N)} + Q_B T_{11}^{(N)}\right)} e^{\mathrm{i}\,2K_A x_A} \tag{2.64}$$

and

$$\frac{U_T}{U_I} = \frac{\mathrm{i}\,2Q_A}{Q_A Q_B T_{12}^{(N)} - T_{21}^{(N)} + \mathrm{i}\left(Q_A T_{22}^{(N)} + Q_B T_{11}^{(N)}\right)} e^{\mathrm{i}(K_A x_A - K_B x_B)}\,, \tag{2.65}$$

respectively. The respective energies are obtained by determining the squares of the moduli of the coefficients:

$$\mathcal{R} = \left|\frac{U_R}{U_I}\right|^2 = \frac{\left(Q_A Q_B T_{12}^{(N)} + T_{21}^{(N)}\right)^2 + \left(Q_A T_{22}^{(N)} - Q_B T_{11}^{(N)}\right)^2}{\left(Q_A Q_B T_{12}^{(N)} - T_{21}^{(N)}\right)^2 + \left(Q_A T_{22}^{(N)} + Q_B T_{11}^{(N)}\right)^2} \tag{2.66}$$

and

$$\mathcal{T} = \left|\frac{U_T}{U_I}\right|^2 = \frac{4Q_A^2}{\left(Q_A Q_B T_{12}^{(N)} - T_{21}^{(N)}\right)^2 + \left(Q_A T_{22}^{(N)} + Q_B T_{11}^{(N)}\right)^2}\,. \tag{2.67}$$

By the conservation of energy principle, the sum of $\mathcal{R}$ and $\mathcal{T}$ should be 1 and this is easily verified by noting that $\det(\mathbf{T}^{(N)}) = 1$. In non-propagation regimes, almost all the energy is reflected for which $R \simeq 1$ and $T \simeq 0$.

Illustrative energy plots for the reflection and transmission coefficients are shown in Figure 2.8 for two specific examples. Figure 2.8a considers the case of the monatomic lattice and Figure 2.8b shows the reflection-transmission for a two-mass chain lattice. Note the connection between stop-bands in Figure 2.4, and the reflection maxima in Figure 2.8b. Similar reflection-transmission plots are shown in Section 5.4 for stented artery problems.

2.5 Finite element approximation: the Galerkin method

Finite element methods are based on a solid mathematical background and provide a general solution technique for partial differential equations with a wide range of applications. The steps to derive a finite element discretization are outlined in the following. Most problems in mechanics and physics are described by a set of partial differential equations accompanied by initial or boundary conditions, and the whole set of equations is referred to as the strong form of the problem. However, finite element methods are based on the weak form of the problem, which is equivalent to the former, as shown by the proof given by Hughes in [54].

A finite element approach using the Galerkin method is used in Chapter 5 for a one-dimensional approximation of a stented artery. The underlying theory is presented

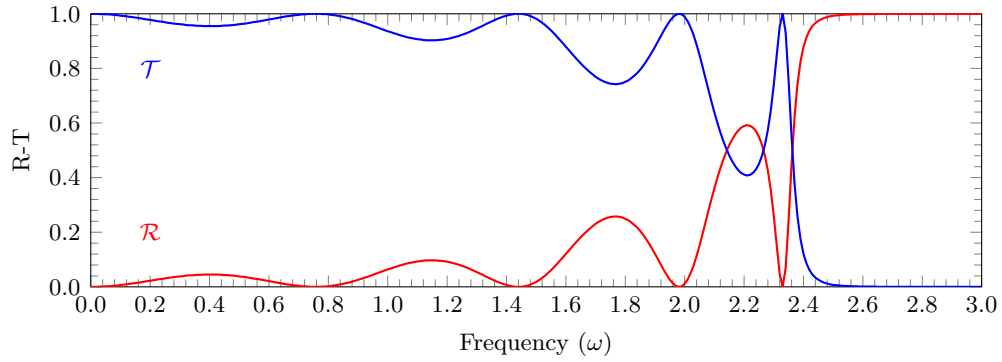

(a) *Reflection-transmission diagram for a monatomic lattice. The parameter values used are* $E_A = 1$, $E_B = 1$, $\rho_A = 1$, $\rho_B = 1$, $\mu = 1.5$, $M = 1$.

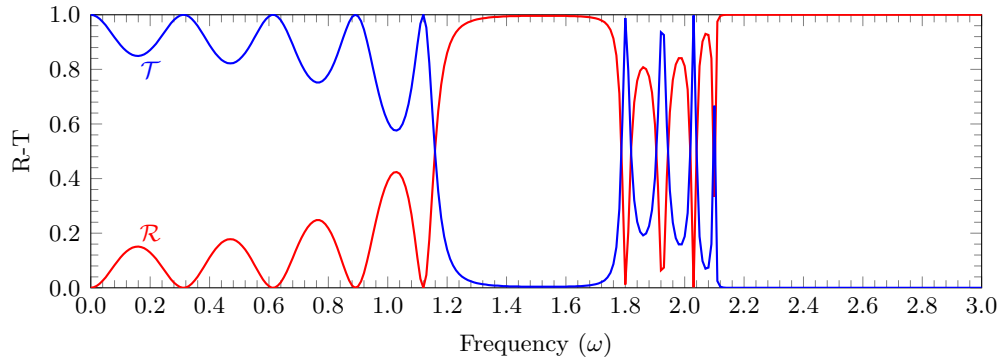

(b) *Reflection-transmission diagram for a two-mass chain lattice. The parameter values used are* $E_A = 1$, $E_B = 1$, $\rho_A = 1$, $\rho_B = 1$, $\mu = 1.5$, $M_1 = 1$, $M_2 = 2$.

Figure 2.8: Reflection-transmission diagrams. For both diagrams $N = 5$.

here for the following one-dimensional linear boundary-value problem:

$$-\frac{\mathrm{d}}{\mathrm{d}x}\left(a(x)\frac{\mathrm{d}u}{\mathrm{d}x}\right) + b(x)\frac{\mathrm{d}u}{\mathrm{d}x} + c(x)u(x) = f(x)\,, \quad x \in (0,1) \tag{2.68a}$$

$$u(0) = g_0\,, \quad a(1)\frac{\mathrm{d}u}{\mathrm{d}x}(1) = g_1\,, \tag{2.68b}$$

with $u \in C^2(0,1) \cap C^1([0,1])$. The functions $a \in C^1([0,1])$ and $b, c, f \in C^0([0,1])$ are given functions on the interval $(0,1)$ and $g_0, g_1 \in \mathbb{R}$ are given boundary data. Here, $C^n([x_0,x_1])$ denotes the space of n-times continuously differentiable functions on the interval $[x_0,x_1]$. For many applications, for instance with discontinuous coefficients, and more general boundary conditions these requirements are too restrictive and so it is necessary to relax the smoothness requirements. This is accomplished by considering weak solutions and transforming the boundary value problem into a weak formulation. In order to define the weak formulation for (2.68) it is necessary to introduce the space

$$V_g = \left\{u \in C^1([0,1]) \quad \text{such that} \quad u(0) = g\right\}\,. \tag{2.69}$$

Multiplying equation (2.68a) with an arbitrary test function $\varphi = \varphi(x)$ in V_0, and integrating over the domain $[0,1]$, then a weighted residual formulation of the original

equation is obtained:

$$-\int_0^1 \frac{\mathrm{d}}{\mathrm{d}x}\left(a(x)\frac{\mathrm{d}u}{\mathrm{d}x}\right)\varphi\,\mathrm{d}x + \int_0^1 b(x)\frac{\mathrm{d}u}{\mathrm{d}x}\varphi\,\mathrm{d}x + \int_0^1 c(x)u(x)\varphi\,\mathrm{d}x = \int_0^1 f(x)\varphi\,\mathrm{d}x\,. \quad (2.70)$$

The weak formulation is obtained using integration by parts:

$$\int_0^1 \left(a(x)\frac{\mathrm{d}u}{\mathrm{d}x}\frac{\mathrm{d}\varphi}{\mathrm{d}x} + b(x)\frac{\mathrm{d}u}{\mathrm{d}x}\varphi + c(x)u(x)\varphi\right)\mathrm{d}x = \int_0^1 f(x)\varphi\,\mathrm{d}x + \left[a(x)\frac{\mathrm{d}u}{\mathrm{d}x}\varphi\right]_0^1 . \quad (2.71)$$

The integration by parts results in boundary contributions, which can be replaced by either using the boundary conditions or using the restrictions imposed on the test function φ. At $x = 0$ the restriction $\varphi(0) = 0$ on the test function φ is imposed, so that the boundary contribution at 0 is eliminated from the weak formulation. At $x = 1$ the boundary condition $a(1)\frac{\mathrm{d}u}{\mathrm{d}x}(1) = g_1$ is used and there is no restriction on the test function φ at $x = 1$.

The boundary value problem (2.68) can be now formulated in terms of the equivalent weak formulation. Find $u \in V_{g_0}$, such that for all $\varphi \in V_0$, the equation:

$$\int_0^1 \left(a(x)\frac{\mathrm{d}u}{\mathrm{d}x}\frac{\mathrm{d}\varphi}{\mathrm{d}x} + b(x)\frac{\mathrm{d}u}{\mathrm{d}x}\varphi + c(x)u(x)\varphi\right)\mathrm{d}x = \int_0^1 f(x)\varphi\,\mathrm{d}x + \varphi(1)g_1\,, \quad (2.72)$$

is satisfied. An important benefit of the weak formulation is that now it is only required that u is differentiable once instead of two times. The weak formulation provides the basis for the finite element discretization.

The objective is to construct piecewise linear continuous functions to be used as test functions in order to compute approximate solutions to the problem of interest. Let N be a positive integer and let x_i, $i = 0, \cdots, N$, define points (called vertices) in $\Omega = (0, 1)$ such that $0 = x_0 < x_1 < x_2 < \cdots < x_N = 1$. Let $I_i = [x_{i-1}, x_i]$ be the intervals (called elements) such that $\bar{\Omega} = \bigcup_{i=1}^N I_i$. The size of the elements is given by $h_i = |x_i - x_{i-1}|$.

Let $V_{g,h}^k = \left\{u \in C^0 \mid u \in P^k(I_i), \forall I_i \subset \Omega, u(0) = g\right\} \subset V_g$, with $P^k(0, 1)$ the space of polynomials of degree k on the interval $(0, 1)$. This implies that in each element, polynomial basis function of degree k are used, and it is only required that the functions are continuous at the element boundaries. The basis functions are defined as $\phi_i(x) \in P^k(I_i)$ if $x \in I_i$, and satisfy the condition $\phi_i(x_j) = \delta_{ij}$, with δ_{ij} the Kronecker delta symbol, which is defined as $\delta_{ij} = 1$ if $i = j$, and zero otherwise. This implies that:

$$\phi_i(x) = \begin{cases} 1\,, & \text{if } x = x_i \\ 0\,, & \text{if } x = x_j\,,\ j \neq i\,. \end{cases} \quad (2.73)$$

An example of linear basis functions are:

$$\phi_i(x) = \begin{cases} \frac{x-x_{i-1}}{h_i}\,, & \text{if } x \in I_i \\ \frac{x_{i+1}-x}{h_{i+1}}\,, & \text{if } x \in I_{i+1} \\ 0\,, & \text{otherwise}\,. \end{cases} \tag{2.74}$$

The function $u \in V^k_{g,h}$ and the test function $\varphi \in V^k_{0,h}$ can now be defined as a linear combination of the basis functions, i.e.:

$$u(x) = g_0\phi_0(x) + \sum_{i=1}^{N} u_i\phi_i(x)\,, \tag{2.75}$$

and

$$\varphi(x) = \sum_{i=1}^{N} \varphi_i\phi_i(x)\,. \tag{2.76}$$

The contribution $g_0\phi_0(x)$ is added to satisfy the boundary condition $u(0) = g_0$, since all the other basis functions ϕ_i are zero at the boundary. Since each of the global basis functions ϕ_i is only non-zero in the two elements connecting to the node x_i, it is convenient to introduce the element basis functions ψ_1 and ψ_2, which are defined in the interval I_i as:

$$\psi_1(x) = \frac{x_i - x}{h_i}\,, \tag{2.77}$$

and

$$\psi_2(x) = \frac{x - x_{i-1}}{h_i}\,. \tag{2.78}$$

Therefore, $\psi_1(x) = \phi_{i-1}(x)$ and $\psi_2(x) = \phi_i(x)$ for $x_i \in I_i$. For more complex basis functions, and also domains in multiple dimensions it is, however, easier to introduce a reference element $\hat{I} = (0, 1)$, with local coordinates ξ, and use the mapping

$$\begin{aligned} F_{I_i} &: (0,1) \to (x_{i-1}, x_i) \\ &\xi \mapsto x \end{aligned}$$

with $x = h_i\xi + x_{i-1}$. In local coordinates, it is possible to define the basis functions as

$$\hat{\psi}_1(\xi) = 1 - \xi\,, \tag{2.79}$$

and

$$\hat{\psi}_2(\xi) = \xi\,. \tag{2.80}$$

The finite element discretization is now obtained by choosing test functions φ which satisfy the condition $\varphi(x) = \phi_i(x)$, $i = 1, \cdots, N$. Since the basis functions ϕ_i are linearly independent and span the space $V^k_{0,h}$, this will result in N linearly independent equations for the coefficient u_i. The finite element discretization is most simply obtained by splitting

the integrals in the weak formulation into integrals over each element:

$$\begin{aligned}&\int_0^1 \left(a(x)\frac{\mathrm{d}u}{\mathrm{d}x}\frac{\mathrm{d}\varphi}{\mathrm{d}x} + b(x)\frac{\mathrm{d}u}{\mathrm{d}x}\varphi + c(x)u(x)\varphi - f(x)\varphi\right)\mathrm{d}x \;= \\ &\sum_{i=1}^{N}\int_{x_{i-1}}^{x_i} \left(a(x)\frac{\mathrm{d}u}{\mathrm{d}x}\frac{\mathrm{d}\varphi}{\mathrm{d}x} + b(x)\frac{\mathrm{d}u}{\mathrm{d}x}\varphi + c(x)u(x)\varphi - f(x)\varphi\right)\mathrm{d}x\,.\end{aligned} \tag{2.81}$$

Using the mapping F_{I_i} it is possible to define the following element integrals:

$$A^i_{nm} = \int_{x_{i-1}}^{x_i} a(x)\frac{\mathrm{d}\psi_m}{\mathrm{d}x}\frac{\mathrm{d}\psi_n}{\mathrm{d}x}\,\mathrm{d}x \;= \frac{1}{h_i}\int_0^1 a(x(\xi))\frac{\mathrm{d}\hat{\psi_m}}{\mathrm{d}\xi}\frac{\mathrm{d}\hat{\psi_n}}{\mathrm{d}\xi}\,\mathrm{d}\xi\,, \tag{2.82a}$$

$$B^i_{nm} = \int_{x_{i-1}}^{x_i} b(x)\frac{\mathrm{d}\psi_m}{\mathrm{d}x}\psi_n\,\mathrm{d}x \;= \frac{1}{h_i}\int_0^1 b(x(\xi))\frac{\mathrm{d}\hat{\psi_m}}{\mathrm{d}\xi}\hat{\psi_n}\,\mathrm{d}\xi\,, \tag{2.82b}$$

$$C^i_{nm} = \int_{x_{i-1}}^{x_i} c(x)\psi_m\psi_n\,\mathrm{d}x \;= \frac{1}{h_i}\int_0^1 c(x(\xi))\hat{\psi_m}\hat{\psi_n}\,\mathrm{d}\xi\,, \tag{2.82c}$$

$$F^i_n = \int_{x_{i-1}}^{x_i} f(x)\psi_n\,\mathrm{d}x \;= \frac{1}{h_i}\int_0^1 f(x(\xi))\hat{\psi_n}\,\mathrm{d}\xi\,, \tag{2.82d}$$

where $m, n = 1, 2$.

Consider now the test function $\varphi(x) = \phi_i(x)$, $i = 2, \cdots, N-1$. This function is only non-zero in the elements I_i and I_{i+1}, where it is equal to $\varphi(x) = \psi_2(x) = \hat{\psi}_2\left(F^{-1}_{I_i}(x)\right) = \hat{\psi}_2(\xi)$ and $\varphi(x) = \psi_1(x) = \hat{\psi}_1\left(F^{-1}_{I_{i+1}}(x)\right) = \hat{\psi}_1(\xi)$, respectively. The representation of u_h in each element I_i:

$$u_h = u_{i-1}\hat{\psi}_1(\xi) + u_i\hat{\psi}_2(\xi)\,, \tag{2.83}$$

is introduced into the element integrals of the weak formulation. Then non-zero contributions are obtained only from the integrals in the elements I_i and I_{i+1}, because the test function φ is zero in the other elements. The weak formulation for the test function $\varphi(x) = \phi_i(x)$, $(i = 2, \cdots, N-1)$ is now:

$$\begin{aligned}&\int_{x_{i-1}}^{x_i} \left(a(x)\left(u_{i-1}\frac{\mathrm{d}\psi_1}{\mathrm{d}x} + u_i\frac{\mathrm{d}\psi_2}{\mathrm{d}x}\right)\frac{\mathrm{d}\psi_2}{\mathrm{d}x} + b(x)\left(u_{i-1}\frac{\mathrm{d}\psi_1}{\mathrm{d}x} + u_i\frac{\mathrm{d}\psi_2}{\mathrm{d}x}\right)\psi_2(x) + \right. \\ &\qquad \left. c(x)\left(u_{i-1}\psi_1(x) + u_i\psi_2(x)\right)\psi_2(x) - f(x)\psi_2(x)\right)\mathrm{d}x + \\ &\int_{x_i}^{x_{i+1}} \left(a(x)\left(u_i\frac{\mathrm{d}\psi_1}{\mathrm{d}x} + u_{i+1}\frac{\mathrm{d}\psi_2}{\mathrm{d}x}\right)\frac{\mathrm{d}\psi_1}{\mathrm{d}x} + b(x)\left(u_i\frac{\mathrm{d}\psi_1}{\mathrm{d}x} + u_{i+1}\frac{\mathrm{d}\psi_2}{\mathrm{d}x}\right)\psi_1(x) + \right. \\ &\qquad \left. c(x)\left(u_i\psi_1(x) + u_{i+1}\psi_2(x)\right)\psi_1(x) - f(x)\psi_1(x)\right)\mathrm{d}x = 0\,.\end{aligned} \tag{2.84}$$

Substituting (2.82) into (2.84), then the previous relation can be simplified as:

$$\begin{aligned}&\left(A^i_{2,1} + B^i_{2,1} + C^i_{2,1}\right)u_{i-1} + \left(A^i_{2,2} + B^i_{2,2} + C^i_{2,2} + A^{i+1}_{1,1} + B^{i+1}_{1,1} + C^{i+1}_{1,1}\right)u_i + \\ &\left(A^{i+1}_{1,2} + B^{i+1}_{1,2} + C^{i+1}_{1,2}\right)u_{i+1} = F^i_2 + F^{i+1}_1\,, \quad i = 2, \cdots, N-1\,.\end{aligned} \tag{2.85}$$

For the test function $\varphi(x) = \phi_1(x)$, different relations are obtained, because the function u_h in the element I_i must be modified to account for the boundary condition at $x = 0$:

$$u_h = g_0\hat{\psi}_1(\xi) + u_1\hat{\psi}_2(\xi)\,. \tag{2.86}$$

Introducing (2.86) into the weak formulation, the following is obtained:

$$\begin{aligned}
&\int_{x_0}^{x_1}\Bigg(a(x)\left(g_0\frac{\mathrm{d}\psi_1}{\mathrm{d}x}+u_1\frac{\mathrm{d}\psi_2}{\mathrm{d}x}\right)\frac{\mathrm{d}\psi_2}{\mathrm{d}x}+b(x)\left(g_0\frac{\mathrm{d}\psi_1}{\mathrm{d}x}+u_1\frac{\mathrm{d}\psi_2}{\mathrm{d}x}\right)\psi_2(x)+\\
&\qquad c(x)\left(g_0\psi_1(x)+u_1\psi_2(x)\right)\psi_2(x)-f(x)\psi_2(x)\Bigg)\,\mathrm{d}x+\\
&\int_{x_1}^{x_2}\Bigg(a(x)\left(u_1\frac{\mathrm{d}\psi_1}{\mathrm{d}x}+u_2\frac{\mathrm{d}\psi_2}{\mathrm{d}x}\right)\frac{\mathrm{d}\psi_1}{\mathrm{d}x}+b(x)\left(u_1\frac{\mathrm{d}\psi_1}{\mathrm{d}x}+u_2\frac{\mathrm{d}\psi_2}{\mathrm{d}x}\right)\psi_1(x)+\\
&\qquad c(x)\left(u_1\psi_1(x)+u_2\psi_2(x)\right)\psi_1(x)-f(x)\psi_1(x)\Bigg)\,\mathrm{d}x=0\,,
\end{aligned} \tag{2.87}$$

which can be simplified as

$$\begin{aligned}
&\left(A^1_{2,2}+B^1_{2,2}+C^1_{2,2}+A^2_{1,1}+B^2_{1,1}+C^2_{1,1}\right)u_1+\\
&\left(A^2_{1,2}+B^2_{1,2}+C^2_{1,2}\right)u_2=F^1_2+F^2_1-\left(A^1_{2,1}+B^1_{2,1}+C^1_{2,1}\right)g_0\,.
\end{aligned} \tag{2.88}$$

Similarly, for $\varphi(x) = \phi_N(x)$, it is:

$$\begin{aligned}
&\int_{x_{N-1}}^{x_N}\Bigg(a(x)\left(u_{N-1}\frac{\mathrm{d}\psi_1}{\mathrm{d}x}+u_N\frac{\mathrm{d}\psi_2}{\mathrm{d}x}\right)\frac{\mathrm{d}\psi_2}{\mathrm{d}x}+b(x)\left(u_{N-1}\frac{\mathrm{d}\psi_1}{\mathrm{d}x}+u_N\frac{\mathrm{d}\psi_2}{\mathrm{d}x}\right)\psi_2(x)+\\
&\qquad c(x)\left(u_{N-1}\psi_1(x)+u_N\psi_2(x)\right)\psi_2(x)-f(x)\psi_2(x)\Bigg)\,\mathrm{d}x=-g_1\,,
\end{aligned} \tag{2.89}$$

which can be simplified as:

$$\left(A^N_{2,1}+B^N_{2,1}+C^N_{2,1}\right)u_{N-1}+\left(A^N_{2,2}+B^N_{2,2}+C^N_{2,2}\right)u_N=F^N_2-g_1\,. \tag{2.90}$$

By introducing the coefficients:

$$\begin{aligned}
K^1_i &= A^i_{2,1}+B^i_{2,1}+C^i_{2,1}\,,\quad i=2,\cdots,N\,,\\
K^2_i &= A^i_{2,2}+B^i_{2,2}+C^i_{2,2}+A^{i+1}_{1,1}+B^{i+1}_{1,1}+C^{i+1}_{1,1}\,,\quad i=1,\cdots,N-1\,,\\
K^2_N &= A^N_{2,2}+B^N_{2,2}+C^N_{2,2}\,,\\
K^3_i &= A^{i+1}_{1,2}+B^{i+1}_{1,2}+C^{i+1}_{1,2}\,,\quad i=1,\cdots,N-1\,,
\end{aligned}$$

and

$$\begin{aligned} R_i &= F_2^i + F_1^{i+1}\,, \quad i = 2, \cdots, N-1\,, \\ R_1 &= F_2^1 + F_1^2 - \left(A_{2,1}^1 + B_{2,1}^1 + C_{2,1}^1\right) g_0\,, \\ R_N &= F_2^N - g_1\,, \end{aligned}$$

then it is possible to write the equations for the coefficients u_i for $i = 1, \cdots, N$ as the linear system:

$$\mathbf{K}\mathbf{u} = \mathbf{R}\,. \tag{2.91}$$

Here $\mathbf{K}$ is called the stiffness matrix and $\mathbf{R}$ the load vector. The linear system (2.91) has a tri-diagonal matrix and can be solved using standard numerical linear algebra techniques. As stated at the beginning of this section, this method is applied to the one-dimensional model for the stented artery in Chapter 5.

2.6 Mathieu's Equation

Mathieu's equation is a linear second-order differential equation with periodic coefficients and is discussed in various references, including the book by Abramowitz and Stegun [1]. Given $a, q \in \mathbb{R}$ the Mathieu equation is defined as

$$\frac{d^2y}{dz^2} + [a - 2q\cos(2z)]\, y = 0\,. \tag{2.92}$$

The equation (2.92) has two families of independent solutions, namely the even and odd Mathieu functions of the first kind which are denoted by $ce_n(z;q)$ and $se_n(z;q)$, respectively, where $n = 0, 1, 2, \cdots$ is the order. In general, the solutions of Mathieu's equation are not periodic. However, there exist values of q for which periodic solutions exist. These solutions are periodic in z, with period π or 2π. A period π means that the eigenfunction has the property

$$y(z + \pi) = y(z). \tag{2.93}$$

The related antiperiod π means that

$$y(z + \pi) = -y(z). \tag{2.94}$$

For even parity, $y(-z) = y(z)$, and odd parity infers $y(-z) = -y(z)$. As a consequence of the periodicity, the values of a in equation (2.92) are the eigenvalues or characteristic values and are denoted by $a_n(q)$ for $ce_n(z;q)$ and $b_n(q)$ for $se_n(z;q)$.

According to the Sturm-Liouville theory, the eigenvalues form an infinite set of countable real values that have the property $a_0 < b_1 < a_1 < b_2 < \cdots$. Each function ce_n and se_n is associated with an eigenvalue a_n or b_n, which in turn depends on q. In Figure 2.9 the functions ce_n and se_n are plotted for $q = 1$ and $q = 10$.

Basic properties of Mathieu's equation include

Even π-Periodic Solutions

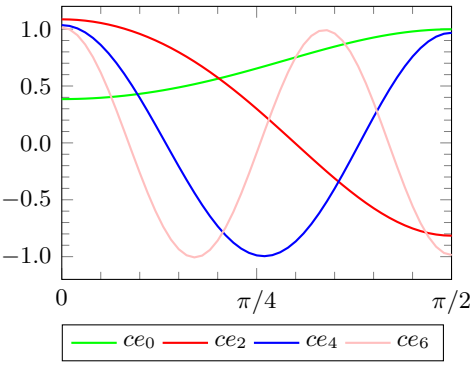

(a) $ce_{2n}(z, 1)$ *for* $0 \leq z \leq \pi/2$, $n = 0, 1, 2, 3$.

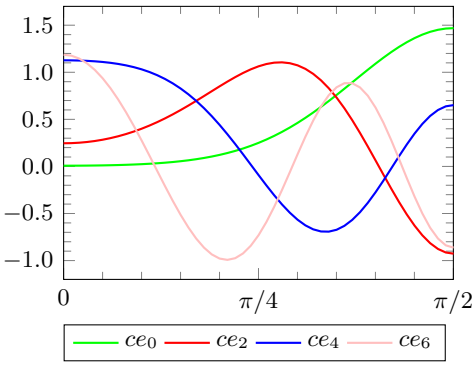

(b) $ce_{2n}(z, 10)$ *for* $0 \leq z \leq \pi/2$, $n = 0, 1, 2, 3$.

Even π-Antiperiodic Solutions

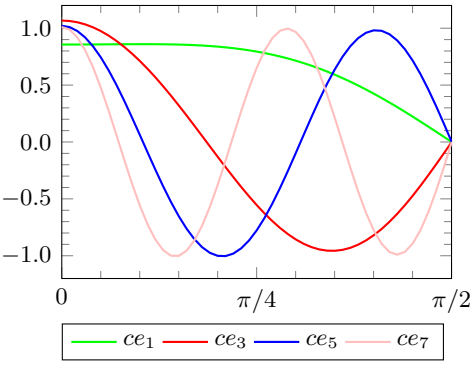

(c) $ce_{2n+1}(z, 1)$ *for* $0 \leq z \leq \pi/2$, $n = 0, 1, 2, 3$.

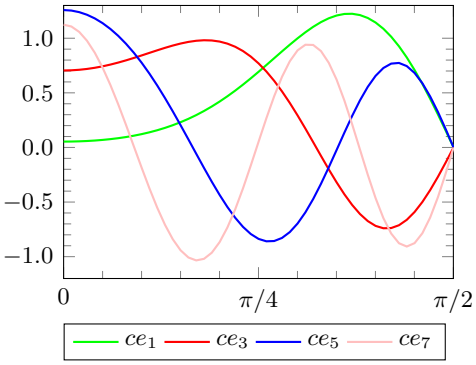

(d) $ce_{2n+1}(z, 10)$ *for* $0 \leq z \leq \pi/2$, $n = 0, 1, 2, 3$.

Odd π-Antiperiodic Solutions

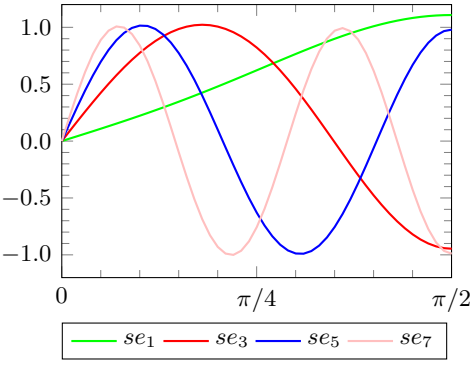

(e) $se_{2n+1}(z, 1)$ *for* $0 \leq z \leq \pi/2$, $n = 0, 1, 2, 3$.

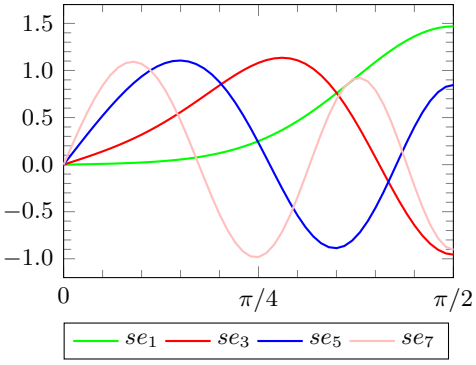

(f) $se_{2n+1}(z, 10)$ *for* $0 \leq z \leq \pi/2$, $n = 0, 1, 2, 3$.

Odd π-Periodic Solutions

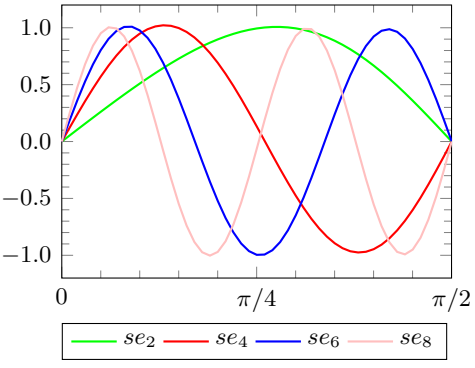

(g) $se_{2n}(z, 1)$ *for* $0 \leq z \leq \pi/2$, $n = 1, 2, 3, 4$.

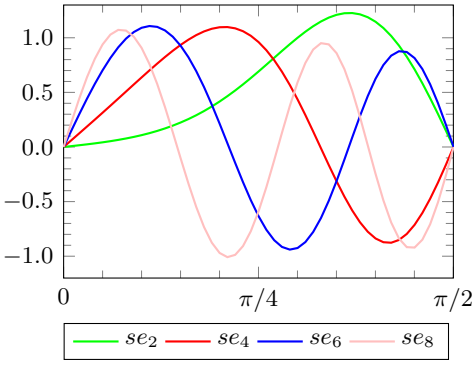

(h) $se_{2n}(z, 10)$ *for* $0 \leq z \leq \pi/2$, $n = 1, 2, 3, 4$.

Figure 2.9: ce_n and se_n plotted for $q = 1$ and $q = 10$.

- The three transformations $z \to -z$; $z \to z \pm \pi$; $z \to z \pm \frac{1}{2}\pi\,, q \to -q$ each leave equation (2.92) unaltered.
- Mathieu's equation (2.92) has two fundamental solutions, $y_1(z;a,q)$ and $y_2(z;a,q)$ with y_1 even and $y_1(0;a,q) = 1\,,\ y_1'(0;a,q) = 0$; y_2 is odd and $y_2(0;a,q) = 0\,,\ y_2'(0;a,q) = 1$.

The fundamental solutions are connected to the Mathieu functions in the following way (see the book by Olver *et al.* [95]):

$$\frac{ce_n(z;q)}{ce_n(0;q)} = y_1(z;a_n(q),q)\,, \quad n \geq 0\,, \tag{2.95a}$$

$$\frac{se_n(z;q)}{se_n'(0;q)} = y_2(z;b_n(q),q)\,, \quad n \geq 1\,. \tag{2.95b}$$

Another important property involves the orthogonality of the Mathieu functions of the first kind, i.e.

$$\int_0^{2\pi} ce_p ce_q\,\mathrm{d}z = \int_0^{2\pi} se_p se_q\,\mathrm{d}z = 0\,, \quad \text{if } p \neq q; \tag{2.96a}$$

$$\int_0^{2\pi} ce_p se_q\,\mathrm{d}z = 0\,. \tag{2.96b}$$

2.6.1 Floquet's Theorem

Floquet's theorem derives from the fact that an arbitrary solution $y(z)$ of a linear homogeneous second-order ODE, such as (2.92), can be expressed as a linear combination of at most two linearly independent solutions $y_1(z)$ and $y_2(z)$, i.e.

$$y(z) = c_1 y_1(z) + c_2 y_2(z)\,. \tag{2.97}$$

Since the Mathieu equation has exactly the same form at $z+\pi$ as it has at z, the solution $y(z+\pi)$ must be a linear combination of $y_1(z)$ and $y_2(z)$, i.e.

$$y(z+\pi) = h_1 y_1(z) + h_2 y_2(z)\,. \tag{2.98}$$

It is also true that

$$y_1(z+\pi) = f_1 y_1(z) + f_2 y_2(z)\,, \tag{2.99a}$$

$$y_2(z+\pi) = g_1 y_1(z) + g_2 y_2(z)\,, \tag{2.99b}$$

and, from equation (2.97) evaluated for $z+\pi$,

$$y(z+\pi) = c_1 y_1(z+\pi) + c_2 y_2(z+\pi)\,. \tag{2.100}$$

Combining equations (2.99) and (2.100) results in

$$y(z+\pi) = (f_1 c_1 + g_1 c_2)\, y_1(z) + (f_2 c_1 + g_2 c_2)\, y_2(z)\,. \tag{2.101}$$

From equations (2.98) and (2.101), it is clear that

$$f_1 c_1 + g_1 c_2 = h_1\,, \tag{2.102a}$$

$$f_2 c_1 + g_2 c_2 = h_2\,. \tag{2.102b}$$

Floquet's analysis now proceeds with the observation that c_1 and c_2 may be chosen in such a way that $h_1 = \mu c_1$ and $h_2 = \mu c_2$. It follows that $y(z+\pi) = \mu y(z)$. This selection is equivalent to imposing that c_1 and c_2 are obtained from a solution of the eigenvalue problem

$$\begin{bmatrix} f_1 & g_1 \\ f_2 & g_2 \end{bmatrix} \begin{pmatrix} c_1 \\ c_2 \end{pmatrix} = \mu \begin{pmatrix} c_1 \\ c_2 \end{pmatrix}\,. \tag{2.103}$$

In summary, Floquet's theorem states that it is possible to choose y such that it satisfies the condition $y(z+\pi) = \mu y(z)$, where μ is a root of

$$\begin{vmatrix} f_1 - \mu & g_1 \\ f_2 & g_2 - \mu \end{vmatrix} = 0\,, \tag{2.104}$$

with the c_i given as eigenvectors, corresponding to μ, of the system (2.103). A solution to the Mathieu equation in the form consistent with Floquet's theorem is often called a Floquet solution, as stated in [1], and its qualitative behaviour is associated with the eigenvalue μ. A Floquet solution is only periodic for special values of μ, with $|\mu| = 1$ being a necessary condition for periodicity.

It is useful to gain more understanding of the Floquet solutions, and this can be done by firstly assuming that y is a solution corresponding to μ. Then the quantities ν and Φ are defined such that $\mu = \exp(\pi\,\mathrm{i}\,\nu)$ and $\Phi(z) = \exp(-\,\mathrm{i}\,\nu z) y(z)$, from which it follows that $y(z+\pi) = \exp(\pi\,\mathrm{i}\,\nu) y(z)$. These definitions have the effect that

$$\Phi(z+\pi) = e^{-\,\mathrm{i}\,\nu(z+\pi)} y(z+\pi) = e^{-\,\mathrm{i}\,\nu z}\left[e^{-\,\mathrm{i}\,\nu\pi} y(z+\pi)\right] = e^{-\,\mathrm{i}\,\nu z} y(z) = \Phi(z)\,, \tag{2.105}$$

showing that $\Phi(z)$ is a periodic function of z with period π. Furthermore,

$$y(z) = e^{\mathrm{i}\,\nu z}\Phi(z)\,, \tag{2.106}$$

which shows that a Floquet solution $y(z)$ consists of a periodic function of z multiplied by a complex exponential in z. The quantity ν, which controls the exponential behaviour, is referred to as the characteristic exponent of the Floquet solution y.

It is possible to classify various cases dependent upon the characteristic exponent ν. If $\mathrm{Im}(\nu) > 0$, the Floquet solution will asymptotically approach zero as z is increased. In contrast, if $\mathrm{Im}(\nu) < 0$, $y(z)$ will grow as z increases. In addition, the Floquet solution y

has constant magnitude through successive cycles of length π only if ν is real. Since y includes the factor $\Phi(z)$, which is periodic with period π, $y(z)$ is also periodic with the period defined as:

(a) π, if $\nu = 0, 2, \cdots$ (corresponding to $\mu = 1$),

(b) 2π, if $\nu = 1, 3, \cdots$ (corresponding to $\mu = -1$) or

(c) $s\pi$, if $\nu = 2r/s$ where r and $s > 2$ are integers with no common divisor.

In order to illustrate how Floquet's theorem is applied to Mathieu's equation, y_1 is chosen to be an even function of z, such that $y_1(0) = 1$ and $y_1^{'}(0) = 0$, and y_2 is chosen to be an odd function such that $y_2(0) = 0$ and $y_2^{'}(0) = 1$. Then, from equation (2.99), and from the derivatives of equation (2.99) evaluated at $z = 0$, it follows that

$$y_1(\pi) = f_1\,, \tag{2.107a}$$

$$y_2(\pi) = g_1\,, \tag{2.107b}$$

$$y_1^{'}(\pi) = f_2\,, \tag{2.107c}$$

$$y_2^{'}(\pi) = g_2\,. \tag{2.107d}$$

The eigenvalue problem (2.104), then becomes

$$\begin{vmatrix} y_1(\pi) - \mu & y_2(\pi) \\ y_1^{'}(\pi) & y_2^{'}(\pi) - \mu \end{vmatrix} = \mu^2 - \Big[y_1(\pi) + y_2^{'}(\pi)\Big]\,\mu + \mathcal{W} = 0\,, \tag{2.108}$$

where

$$\mathcal{W} = y_1(\pi)y_2^{'}(\pi) - y_2(\pi)y_1^{'}(\pi)\,, \tag{2.109}$$

is the Wronskian of the y_i, evaluated at $z = \pi$. However, the Wronskian of the Mathieu equation is a constant, as given by Arfken *et al.* [4], and therefore it is possible to evaluate $\mathcal{W}$ at $z = 0$, for which $\mathcal{W} = 1$.

Using standard properties of quadratic equations, it is possible to identify $\mathcal{W}$ as the product of two roots, such that

$$\mu_1\mu_2 = 1\,. \tag{2.110}$$

Now, it is possible to enumerate the various possibilities for the eigenvalues μ_i. If $|\mu_1| < 1$, then $|\mu_2| > 1$ and vice versa. In these cases neither solution y_1 nor y_2 is periodic. If $|\mu_1| = |\mu_2| = 1$, by writing the roots in the form $\exp(\mathrm{i}\,\nu_i\pi)$ and observing that equation (2.110) is only satisfied if $\nu_2 = -\nu_1$, then $\mu_2 = \mu_1^*$, where * indicates complex conjugation. Thus, the solutions will have period π if $\mu = 1$, period 2π if $\mu = -1$ and period $s\pi$ $(s > 2)$ if the ν_i are rational fractions. Note that in the cases $\mu = 1$ and $\mu = -1$, there is a double root $\mu_1 = \mu_2 = \pm 1$ but if the μ_i are complex, there will be distinct roots.

The nature of the roots μ_i determines the number of periodic solutions. If the μ_i are distinct, there are two periodic solutions since there must be at least one eigenvector

for each distinct eigenvalue. It follows that the periodic solutions with period $s\pi, s > 2$ are found in pairs. However, if the eigenvalues are degenerate, which corresponds to periodicity π or 2π, there can only be two eigenvectors (i.e. periodic ODE solutions) if the matrix in equation (2.103) is not defective (non-diagonalizable). Although defectiveness may appear to be unlikely, it occurs exactly when one of the solutions, say y_1, is periodic with period π or 2π. For the former case, the coefficients g_1 and g_2, that describe y_2, are both non-zero and the matrix from (2.103) takes the form:

$$\begin{bmatrix} 1 & g_1 \\ 0 & 1 \end{bmatrix}, \tag{2.111}$$

for which the only eigenvector is y_1. For physical reasons, the most important solutions occur when the periods are π or 2π, and these are the even and odd Mathieu functions of the first kind, $ce_n(z;q)$ and $se_n(z;q)$.

2.6.2 Fourier expansions

Since the Mathieu functions of the first kind ce_n and se_n are periodic, they can be expanded in terms of Fourier series. The corresponding expansions fall into four classes, according to their symmetry or antisymmetry, about $z = 0$ and $z = \pi/2$, namely,

$$ce_{2n}(z;q) = \sum_{k=0}^{\infty} A_{2k}^{(2n)}(q)\cos(2kz), \tag{2.112a}$$

$$ce_{2n+1}(z;q) = \sum_{k=0}^{\infty} A_{2k+1}^{(2n+1)}(q)\cos((2k+1)z), \tag{2.112b}$$

$$se_{2n+1}(z;q) = \sum_{k=0}^{\infty} B_{2k+1}^{(2n+1)}(q)\sin((2k+1)z), \tag{2.112c}$$

$$se_{2n+2}(z;q) = \sum_{k=0}^{\infty} B_{2k+2}^{(2n+2)}(q)\sin((2k+2)z), \tag{2.112d}$$

where $n \geq 0$. By insertion of these expansions into equation (2.92), the recurrence relations between the coefficients A and B can be derived. For instance, for the functions

ce_{2n} it is:

$$\left(\frac{\mathrm{d}^2}{\mathrm{d}z^2}+a\right)ce_{2n}(z;q)=\sum_{k=0}^{\infty}\left(-4k^2+a_{2n}(q)\right)A_{2k}^{(2n)}(q)\cos\left(2kz\right), \tag{2.113a}$$

$$\begin{aligned}-2q\cos\left(2z\right)ce_{2n}(z;q) &= -2q\cos\left(2z\right)ce_{2n}(z;q)\sum_{k=0}^{\infty}A_{2k}^{(2n)}(q)\cos\left(2kz\right)\\ &= -2qA_0^{2n}\cos\left(2z\right)-2q\sum_{k=1}^{\infty}A_{2k}^{(2n)}(q)\cos\left(2z\right)\cos\left(2kz\right)\\ &= -2qA_0^{2n}\cos\left(2z\right)-q\sum_{k=1}^{\infty}A_{2k}^{(2n)}(q)\left[\cos\left(\left(2k+2\right)z\right)+\cos\left(\left(2k-2\right)z\right)\right].\end{aligned} \tag{2.113b}$$

Equating coefficients of $\cos\left(2kz\right)$ for $k=0,1,2,\cdots$, and simplifying the notation by using a for $a_{2n}(q)$ and A_{2k} for $A_{2k}^{(2n)}(q)$, it is

$$aA_0-qA_2=0, \tag{2.114a}$$

$$\left(a-4\right)A_2-q\left(A_4+2A_0\right)=0, \tag{2.114b}$$

$$\left(a-4k^2\right)A_{2k}-q\left(A_{2k+2}+A_{2k-2}\right)=0, \quad k\geq 2. \tag{2.114c}$$

A similar procedure is valid for ce_{2n+1}, se_{2n+1} and se_{2n+2}. Again simplifying the notation by using b for $b_n(q)$ and B_k for $B_{2k+1}^{(2n+1)}(q)$ and $B_{2k+2}^{(2n+2)}(q)$ the following recurrence relations yield. For $ce_{2n+1}(q;z)$ it is

$$\left(a-1-q\right)A_1-qA_3=0, \tag{2.115a}$$

$$\left(a-\left(2k+1\right)^2\right)A_{2k+1}-q\left(A_{2k-1}+A_{2k+3}\right)=0, \quad k\geq 1. \tag{2.115b}$$

For $se_{2n+1}(q;z)$ it is

$$\left(b-1+q\right)B_1-qB_3=0, \tag{2.116a}$$

$$\left(a-\left(2k+1\right)^2\right)B_{2k+1}-q\left(B_{2k-1}+B_{2k+3}\right)=0, \quad k\geq 1. \tag{2.116b}$$

For $se_{2n+2}(q;z)$ it is

$$\left(b-4\right)B_2-qB_4=0, \tag{2.117a}$$

$$\left(b-4k^2\right)B_{2k}-q\left(B_{2k-2}+B_{2k+2}\right)=0, \quad k\geq 2. \tag{2.117b}$$

The theory of Mathieu functions is used in Chapter 5, where a special case for the one-dimensional model for a stented artery is shown to be reducible to the Mathieu equation.

Chapter 3

Three-dimensional model for blood vessels reinforced by stents

3.1 Waves in a periodically reinforced blood vessel

In this chapter, based on the paper by Frecentese *et al.* [36], the Bloch-Floquet approach is used to analyse the waves that can propagate through the stented artery system and to determine their dynamic properties. As explained in Section 2.3, this method allows one to derive the relation between the frequency and the wavenumber (or, equivalently, the Bloch-Floquet parameter). This relation is called the *dispersion relation* and its real solutions yield the so-called *dispersion curves*. The dispersion curves provide the group velocity (corresponding to the slope of the curve) and the phase velocity (secant slope) at each frequency. They also indicate the frequency ranges in which waves can physically propagate within the system (called *pass-bands*) and the ranges in which waves cannot propagate (called *stop-bands*). The Bloch-Floquet analysis reduces the problem to the study of a single unit cell which, in this case, includes the artery wall, the stent structure, and the blood. The elementary cell for this problem is more complicated than the illustrative introductory examples described in Section 2.3 but the same principles of reduction to an elementary cell and implementation of quasi-periodicity conditions are applied. Some examples of representative mode shapes are shown in Figure 3.1.

3.1.1 Governing equations

In the following, subscripts 'a', 's', and 'f' in the equations denote the artery, the stent, and the fluid (blood), respectively. Small displacement theory is implemented in this work.

In order to determine the dispersion relation, the artery is modelled as a hollow cylinder composed of a linear elastic isotropic homogeneous material. Accordingly, its equations of motions are

$$\mu_{\mathrm{a}}\,\nabla^2\boldsymbol{u}_{\mathrm{a}} + (\lambda_{\mathrm{a}} + \mu_{\mathrm{a}})\nabla(\nabla\cdot\boldsymbol{u}_{\mathrm{a}}) = \rho_{\mathrm{a}}\frac{\partial^2\boldsymbol{u}_{\mathrm{a}}}{\partial t^2}\,, \tag{3.1}$$

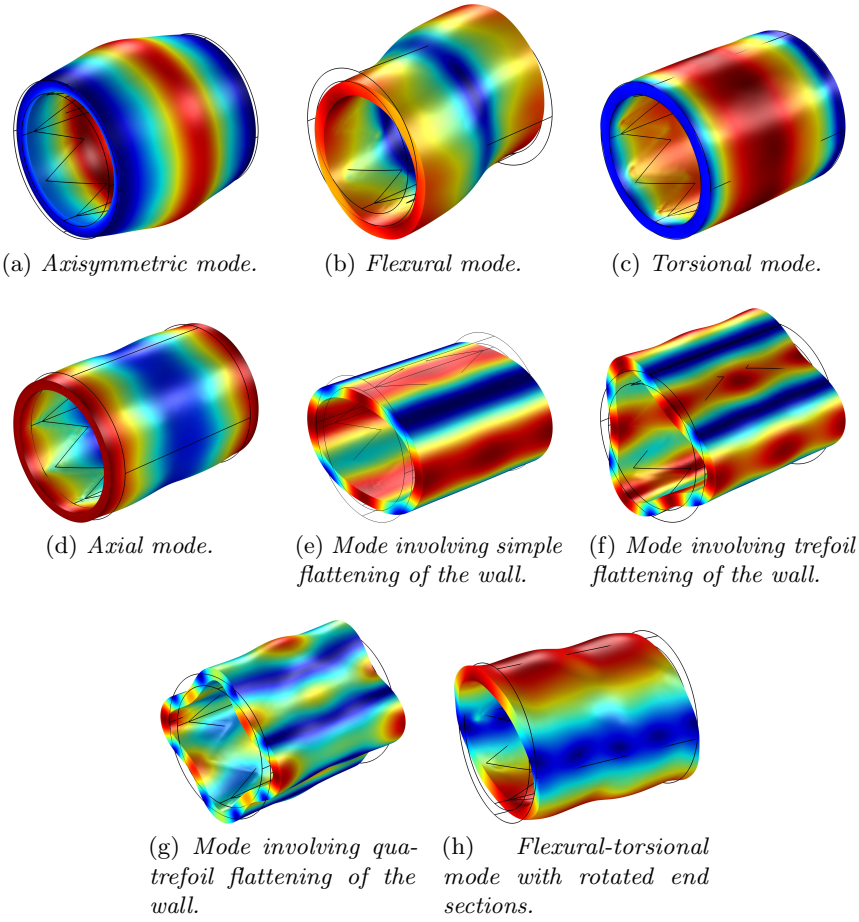

(a) *Axisymmetric mode.* (b) *Flexural mode.* (c) *Torsional mode.*

(d) *Axial mode.* (e) *Mode involving simple flattening of the wall.* (f) *Mode involving trefoil flattening of the wall.*

(g) *Mode involving quatrefoil flattening of the wall.* (h) *Flexural-torsional mode with rotated end sections.*

Figure 3.1: Representative shapes of the deformation modes observed in the unit cell with a stent.

where μ_a and λ_a are the Lamé parameters, ρ_a is the density (mass per unit volume), $\boldsymbol{u}_\mathrm{a}$ is the displacement vector, t is time, and $\nabla = (\partial/\partial x, \partial/\partial y, \partial/\partial z)^\mathrm{T}$ represents the vector differential operator.

The blood is modelled as an acoustic medium, and its equation of motion is

$$K_\mathrm{f}\,\nabla^2 p_\mathrm{f} = \rho_\mathrm{f}\,\frac{\partial^2 p_\mathrm{f}}{\partial t^2}\,, \tag{3.2}$$

where p_f and K_f are the pressure and the bulk modulus of the fluid, respectively, and ρ_f is the density of the fluid. This approximation yields accurate results within the framework of eigenfrequency analysis, as previously shown in the literature, see for example the study of fluid-filled containers in the recent paper by Carta *et al.* [18].

Since the fluid is modelled as an acoustic medium, the coupling at the fluid-solid interface is obtained by means of the following relation for the stresses

$$\boldsymbol{\sigma}_\mathrm{a}\,\boldsymbol{n} = -p_\mathrm{f}\,\boldsymbol{n}\,, \tag{3.3}$$

where $\boldsymbol{\sigma}_\mathrm{a}$ is the stress tensor in the artery wall and $\boldsymbol{n}$ is the unit outward normal vector. The exterior boundary of the artery wall is free and this is expressed using the relation

$$\boldsymbol{\sigma}_\mathrm{a}\,\boldsymbol{n} = \boldsymbol{0}\,. \tag{3.4}$$

It should be noted that the simplified time-harmonic computations are accompanied by the full transient analysis of the fluid-structure interaction in the presence of the viscous Newtonian fluid in Section 3.4. The most interesting wave regimes identified in the linearised time-harmonic model are given special attention in the transient computations.

In the linearised time-harmonic computations, the stent is modelled as a curved wire with a circular cross-section; the material is assumed to be linearly elastic, isotropic and homogeneous. The stents are considered to be already deployed and in contact with the artery wall. In this work the connection between the stent and the artery wall is assumed to be bilateral, which means that the stents are tied to the inner artery wall. Hence, continuity of displacements and tractions is assumed at the interface. No other constraints are applied in the model in order to allow for a broad class of deformation of the vessel. In fact, arteries themselves can be mobile with the movement of the body, including elongation and twisting, as observed by Scheinert *et al.* [104] and Cheng *et al.* [27].

3.1.2 Bloch-Floquet waves

As is standard for Bloch-Floquet analysis, the time-harmonic regime is assumed. Hence, the displacement field in the artery, the pressure field in the blood, and the displacement field in the stent are expressed as

$$\boldsymbol{u}_\mathrm{a}(\boldsymbol{x},t) = \boldsymbol{U}_\mathrm{a}(\boldsymbol{x})e^{\mathrm{i}\,\omega t}\,, \tag{3.5a}$$

$$p_\mathrm{f}(\boldsymbol{x},t) = P_\mathrm{f}(\boldsymbol{x})e^{\mathrm{i}\,\omega t}\,, \tag{3.5b}$$

$$\boldsymbol{u}_\mathrm{s}(\boldsymbol{x},t) = \boldsymbol{U}_\mathrm{s}(\boldsymbol{x})e^{\mathrm{i}\,\omega t}\,, \tag{3.5c}$$

where $\boldsymbol{U}_\mathrm{a}$ and $\boldsymbol{U}_\mathrm{s}$ denote, respectively, the displacement amplitude vectors for the artery wall and for the stent, P_f is the pressure amplitude, and ω is the radian frequency.

Bloch-Floquet quasi-periodicity conditions are imposed, as shown in Figure 3.2a, and they are given by

$$\boldsymbol{U}_\mathrm{a}(x+L_\mathrm{a},y,z) = \boldsymbol{U}_\mathrm{a}(x,y,z)e^{\mathrm{i}\,kL_\mathrm{a}}\,, \tag{3.6a}$$

$$P_\mathrm{f}(x+L_\mathrm{a},y,z) = P_\mathrm{f}(x,y,z)e^{\mathrm{i}\,kL_\mathrm{a}}\,, \tag{3.6b}$$

$$\boldsymbol{U}_\mathrm{s}(x+L_\mathrm{a},y,z) = \boldsymbol{U}_\mathrm{s}(x,y,z)e^{\mathrm{i}\,kL_\mathrm{a}}\,, \tag{3.6c}$$

where L_a is the length of the unit cell, k is the wavenumber, which is inversely proportional to the wavelength $\lambda = 2\pi/k$, and (x,y,z) is a point in the elementary cell, which includes the boundary.

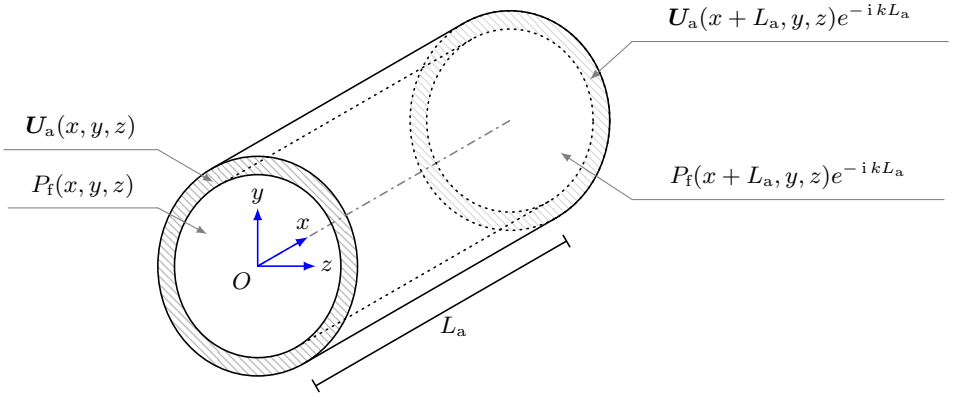

(a) *Scheme of the Bloch-Floquet quasi-periodic conditions.*

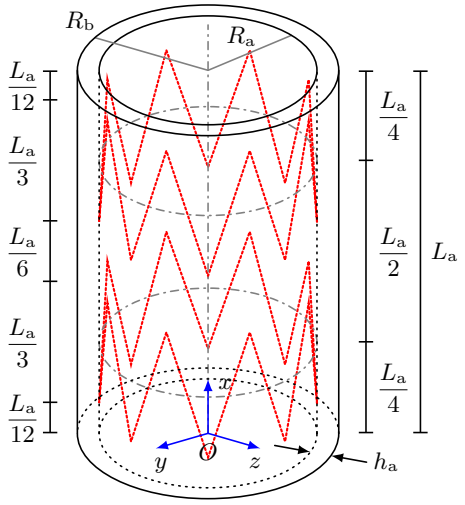

(b) *Scheme of the unit cell.*

Figure 3.2: Representation of the geometry and of the quasi-periodic boundary conditions of the unit cell employed in the numerical simulations. The middle lines of the coils are represented by red dotted lines in (b). The dash-dotted circumferences shown in (b) represent the intersection between the inner wall of the artery and the transverse planes containing the centroids of the two coils.

3.1.3 Definition of the three-dimensional geometries

The unit cell for the stented artery is composed of a hollow cylinder (representing the wall of the vessel), two zigzag-shaped coils (representing the stent pattern), and a cylindrical fluid domain enclosed by the hollow cylinder (representing the blood), as sketched in Figure 3.2b. The artery wall is modelled as a three-dimensional solid, having a length L_a of 10 mm, a lumen diameter $2R_\mathrm{a}$ of 7.3 mm, and a thickness h_a of 0.7 mm. Therefore, the outer diameter $2R_\mathrm{b}$ is equal to 8.7 mm and the average radius is equal to 4 mm, reproducing representative values available in the literature (see, for example, [32, Tab. 4.2, p. 187]). The zigzag-shaped coils are characterised by 8 crowns (16 segments) and are modelled as beams with a constant circular cross-section (0.1 mm diameter). The distance between the opposite crowns is equal to one third of the unit cell length (≈ 3.333 mm), whereas the distance between the centroids of the two coils is equal to

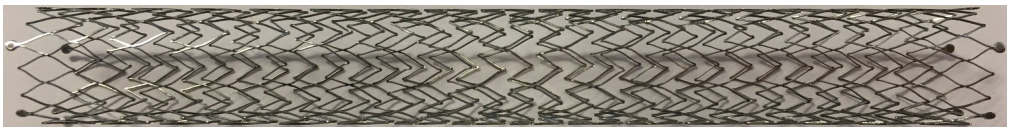

(a) *Example of a Cook zilver stent structure.*

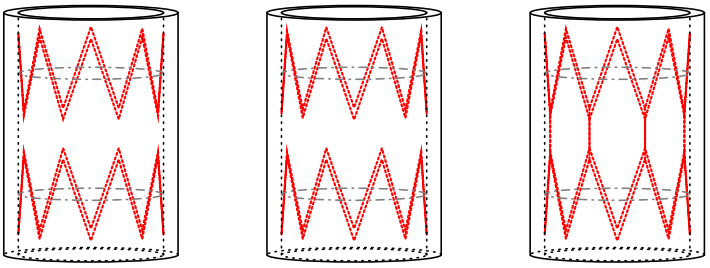

(b) *Unit cell with type A stents.*

(c) *Unit cell with type B stents.*

(d) *Unit cell with type A connected stents.*

Figure 3.3: Examples of unit cells with different stent configurations employed in the numerical simulations. Part (a) illustrates one of many stent geometries. Parts (b)-(d) represent different typical patterns for coils.

half the unit cell length (5 mm), as indicated in Figure 3.2b (on the left and right sides, respectively).

The dynamic response of the stented artery with three different configurations of the coils, shown in Figure 3.3, is investigated. In particular, the following cases are analysed: a symmetric unit cell (type A), where the coils are symmetric with respect to the middle cross-section of the cell (see Figure 3.3b); a unit cell with unidirectional stents (type B), obtained by translation of the coils (see Figure 3.3c); a unit cell with connected type A stents, where some of the crowns are linked with additional beam elements (see Figure 3.3d). It is possible to note that for the cases of Type A and Type B stents, the coils may be connected either by fabric or by very soft and less dense material, such as nylon, and these components may be neglected in the model as they will not affect the overall system. The computations for both Bloch-Floquet and reflection-transmission are performed using the University of Liverpool licensed COMSOL Multiphysics ® versions 5.3 and 5.4.

3.1.4 Material parameters

Arteries are characterised by nonlinear behaviour, for which nonlinear elastic constitutive models (including the description as a heterogeneous material) are reported in the literature as well as their calibration based on experiments by several research groups including Holzapfel *et al.* [51, 53], Lally and co-workers [99, 124], Gastaldi *et al.* [40] and Zhang *et al.* [127]. However, it has been reported, by Back *et al.* [8] for instance, that unhealthy or stented arteries lose much of their flexibility and so linearised approaches can provide useful insights.

Table 3.1: Elastic properties of the materials employed in the simulations.

Properties	Materials	
	Artery	Stent
Young Modulus	$E_{\mathrm{a}} = 800\,\mathrm{kPa}$	$E_{\mathrm{s}} = 210\,\mathrm{GPa}$
Poisson ratio	$\nu_{\mathrm{a}} = 0.49$	$\nu_{\mathrm{s}} = 0.3$
Density	$\rho_{\mathrm{a}} = 1200\,\mathrm{kg\,m^{-3}}$	$\rho_{\mathrm{s}} = 7800\,\mathrm{kg\,m^{-3}}$

Regarding stents, nonlinear constitutive models for shape memory alloys are generally used to describe the behaviour of balloon-expandable and self-expanding stents. Some references include the papers by Azaouzi *et al.* [7] and by Nematzadeh and Sadrnezhaad [93]. Some authors prefer to employ linear elastic constitutive models, see for example the works of Lally *et al.* [66], Walke *et al.* [119] and Schiavone *et al.* [105]. It is worth noting that nonlinear constitutive models are often employed for atherosclerotic tissue and restenosis, as reported in 1994 [74] and more recently by Lally and colleagues [66, 124].

The aim of this study is to identify possible pass-bands and stop-bands for the coupled system composed of the stented artery and the blood by means of the Bloch-Floquet approach. The components of the coupled system are modelled as linear elastic isotropic homogeneous materials. The elastic parameters for the artery tissue and the stents employed in this work are summarised in Table 3.1, and they correspond to typical average values for the carotid artery [32, 94] and for metals commonly used for stents, as reported by Tambaca *et al.* [111]. The blood is modelled as an acoustic medium of bulk modulus $K_{\mathrm{f}} = 2.4\,\mathrm{GPa}$ and density $\rho_{\mathrm{f}} = 1050\,\mathrm{kg\,m^{-3}}$.

3.1.5 Dispersion curves

In this section, the dispersion properties of the Bloch-Floquet elastic waves propagating along the walls of the artery are discussed. The results are presented as dispersion curves in the wavenumber-frequency plane. The dispersion curves are even and $2\pi/L_{\mathrm{a}}$-periodic functions. The interval $[-\pi/L_{\mathrm{a}}, \pi/L_{\mathrm{a}}]$ is known as the *irreducible Brillouin zone*, as defined in Section 2.3. Owing to their symmetry and periodicity, the dispersion curves are illustrated for the range $0 \leq k \leq \pi/L_{\mathrm{a}}$. The dispersion diagrams presented in Figures 3.4-3.10 identify ω as a multi-valued function of the Bloch-Floquet parameter k. The dispersion diagrams show the presence of stop-bands and standing waves (concepts introduced here in Section 2.3) in stented blood vessels. The stop-bands represent the intervals of frequencies for which only evanescent waveforms occur. Standing waves are characterized by zero group velocity and they are observed at the boundaries of stop-bands.

As a first step, the comparison between the case of a healthy artery and the case of an artery with type A stents (Figure 3.3b) is provided. Subsequently, a comparison of the three types of stents depicted in Figure 3.3 is presented to show the influence of the stent geometry on the dispersion properties of the system.

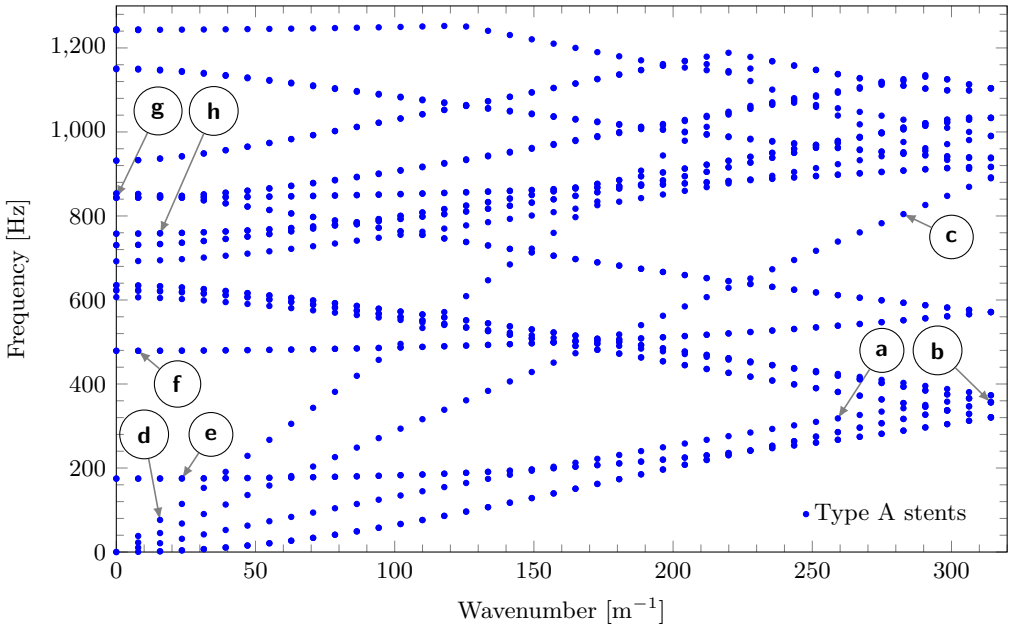

Figure 3.4: Dispersion curves in the wavenumber-frequency plane representing different vibration modes for the symmetric unit cell shown in Figure 3.3b. The shapes of the deformation modes associated with the points highlighted with arrows are depicted in Figure 3.1, where the same letters are used.

3.1.5.1 Vibrational modes: type A stents

Figure 3.4 presents the complete dispersion diagram for type A stents. The labels (a)-(h), which mark the individual dispersion curves in this figure, correspond to representative vibrational modes shown in Figure 3.1. In particular, the four curves corresponding to modes (a)-(d) begin at the origin and are referred to as "acoustic" dispersion curves. Recall that acoustic dispersion curves were introduced in Section 2.3. These curves are dominated by flexural motion (b), axially symmetric expansion/contraction deformation (a), torsional motion (c) and longitudinal motion (d). As the frequency is increased, the individual dispersion curves represent mixed-modes, which incorporate elastic deformations of different types, like the mode represented by curve (h). Here only 8 modes are illustrated because at higher frequencies, the modes become mixed to such a degree that it becomes very difficult to distinguish features and the dispersion properties. It should be noted that there are no common stop-bands. However, it is possible to investigate stop-band formation for each individual vibrational mode separately, by splitting Figure 3.4 into a set of different curves representing different modes. In the following, a selection of representative vibrational modes are discussed.

Figure 3.5 considers the case of type A stents, with the unit cell shown in Figure 3.5a. From Figures 3.5b and 3.5c, it can be noted that the group velocities for the axisymmetric mode are slightly different, with an increase observed in the case of the stented artery. Furthermore, there are no stop-bands at low frequencies, and hence no blockages in transmission are observed. Conversely, at high frequencies the appearance of a stop-band

in the stented artery is noted. The same observations hold true for the flexural mode shown in Figures 3.5d and 3.5e.

A different behaviour is detected for the mode involving simple flattening of the wall, shown in Figures 3.5f and 3.5g. In fact, for the stented artery, the stop-band at low frequencies is much wider in comparison with the unstented artery, and an additional stop-band appears at high frequencies. The stop-band at low frequencies in Figure 3.5f indicates that this mode cannot propagate within the typical frequency range of the blood vessels in human beings. When a type A stent is installed in the artery, this stop-band is wider, which prevents the propagation of the simple wall flattening mode within a larger frequency range, compared to the one that may have been activated without stents.

In Figure 3.6, additional modes for the type A stents are considered. In particular, the dispersion diagrams corresponding to modes involving trefoil and quatrefoil flattening of the wall, and to the flexural-torsional mode with rotation of the end sections, are shown. Large stop-bands are observed for lower frequencies, hence it is unlikely that these modes occur within the standard pulsatile flow regime of the human body. In Figure 3.7, the dispersion properties of torsional and axial modes are illustrated. In these cases, no stop-bands appear.

3.1.5.2 Vibrational modes: comparisons of different types of stents

Comparing Figures 3.5 and 3.8, it can be noted that the behaviour of the system with type A stents and type B stents is very similar. Connected type A stents show a slightly different group velocity at low frequencies compared with type A and B stents, and an additional stop-band appears between the first two dispersion curves associated with each mode. Furthermore, when connected type A stents are installed, the stop-band between the second and the third dispersion curves appears at higher frequencies compared with type A and B stents. In Figure 3.9 the dispersion diagrams corresponding to modes involving trefoil and quatrefoil flattening of the wall and to the flexural-torsional mode with rotation of the end sections are shown. Large stop-bands are observed for lower frequencies, hence it is unlikely that these modes occur within the standard pulsatile flow regime of human body. In Figure 3.10 the dispersion properties of torsional and axial modes are illustrated. In these cases no stop-bands appear.

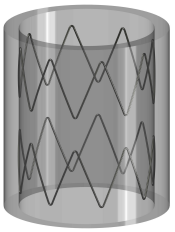

(a) *Unit cell with type A stents.*

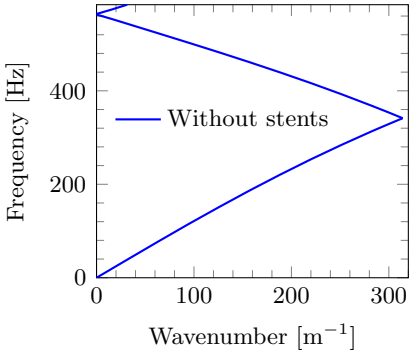

(b) *Unit cell without stents, axisymmetric mode.*

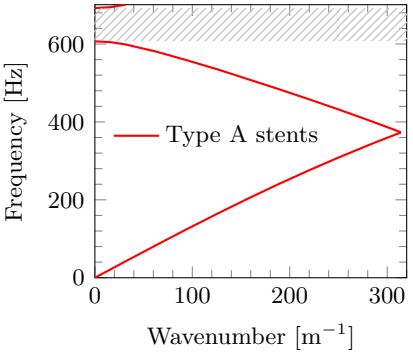

(c) *Unit cell with type A stents, axisymmetric mode.*

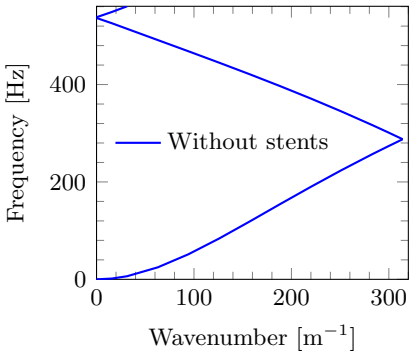

(d) *Unit cell without stents, flexural mode.*

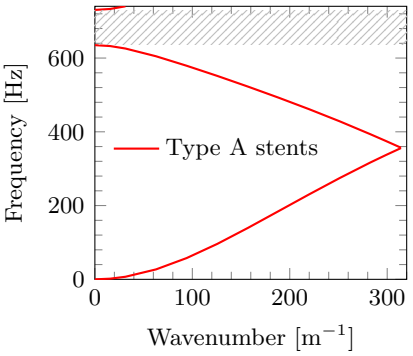

(e) *Unit cell with type A stents, flexural mode.*

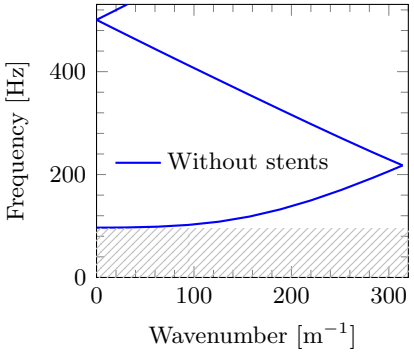

(f) *Unit cell without stents, mode involving simple flattening of the wall.*

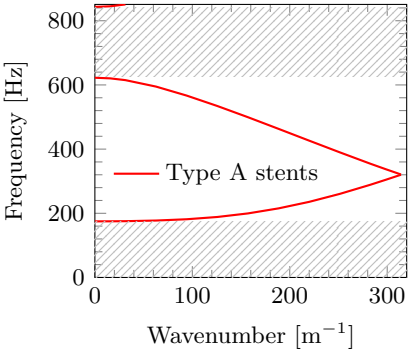

(g) *Unit cell with type A stents, mode involving simple flattening of the wall.*

Figure 3.5: Dispersion curves for the axisymmetric mode (b)-(c), the flexural mode (d)-(e), and for the mode involving simple flattening of the wall (f)-(g), for the unit cell without stents and with type A stents shown in part (a). The shaded zones denote the stop-bands.

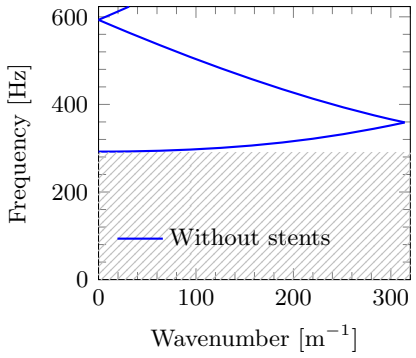

(a) *Unit cell without stents, mode involving trefoil flattening of the wall.*

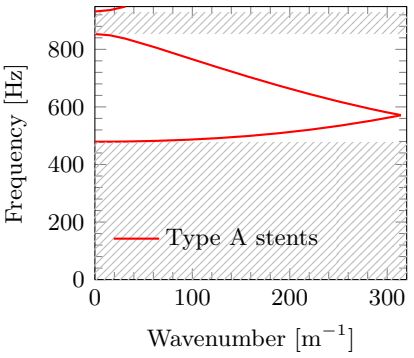

(b) *Unit cell with type A stents, mode involving trefoil flattening of the wall.*

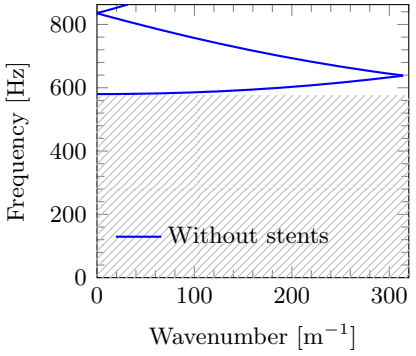

(c) *Unit cell without stents, mode involving quatrefoil flattening of the wall.*

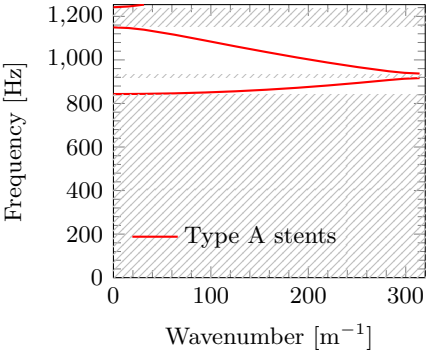

(d) *Unit cell with type A stents, mode involving quatrefoil flattening of the wall.*

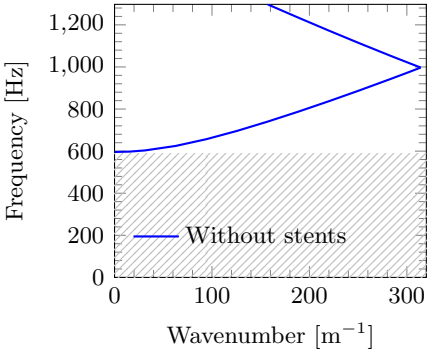

(e) *Unit cell without stents, flexural-torsional mode with rotation of the end sections.*

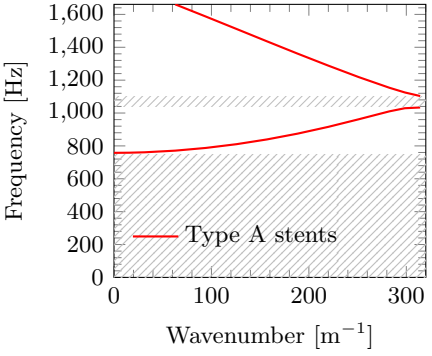

(f) *Unit cell with type A stents, flexural-torsional mode with rotation of the end sections.*

Figure 3.6: Dispersion curves for the mode involving trefoil (a)-(b), and quatrefoil (c)-(d), and for the flexural-torsional modes with rotation of the end sections (e)-(f), for the unit cell without stents and with type A stents. The shaded zones denote the stop-bands.

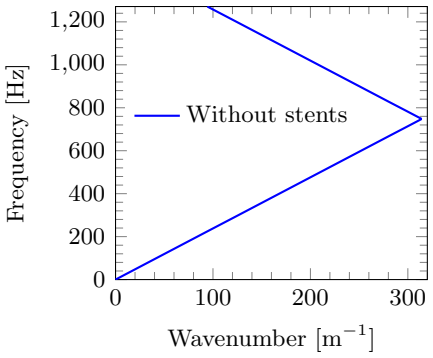

(a) *Unit cell without stents, torsional mode.*

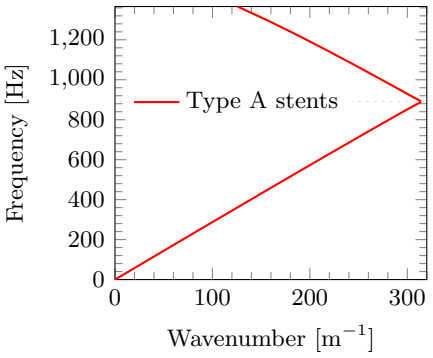

(b) *Unit cell with type A stents, torsional mode.*

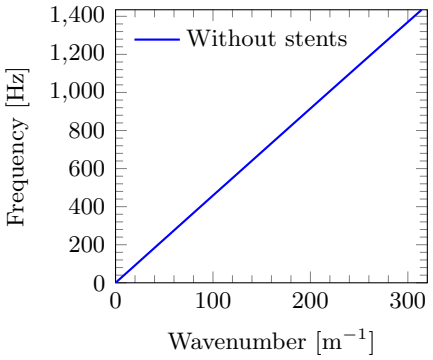

(c) *Unit cell without stents, axial mode.*

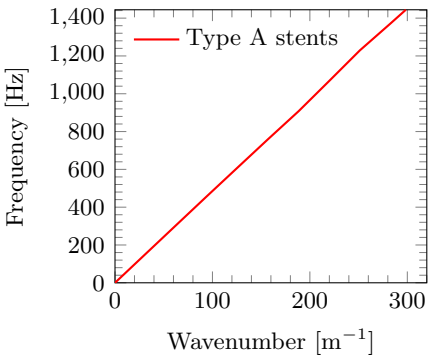

(d) *Unit cell with type A stents, axial mode.*

Figure 3.7: Dispersion curves for the torsional mode (a)-(b), and the axial mode (c)-(d), for the unit cell without stents and with type A stents.

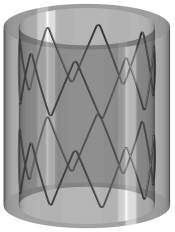

(a) *Unit cell with type B stents.*

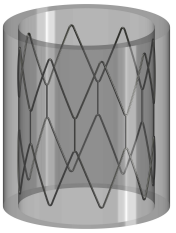

(b) *Unit cell with connected type A stents.*

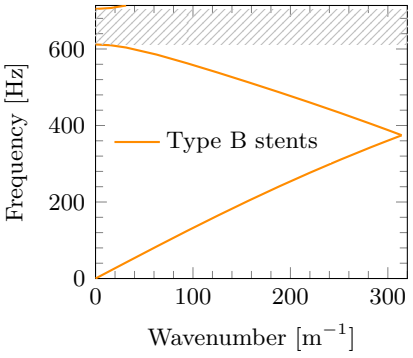

(c) *Unit cell with type B stents, axisymmetric mode.*

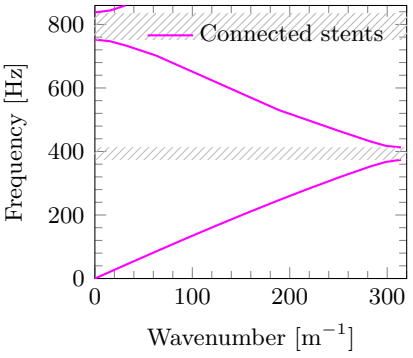

(d) *Unit cell with connected type A stents, axisymmetric mode.*

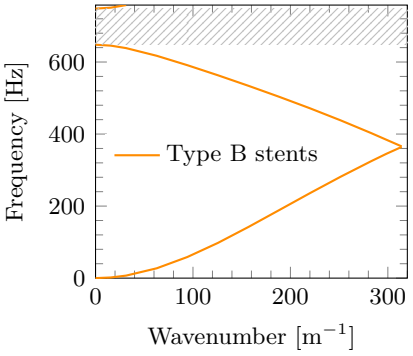

(e) *Unit cell with type B stents, flexural mode.*

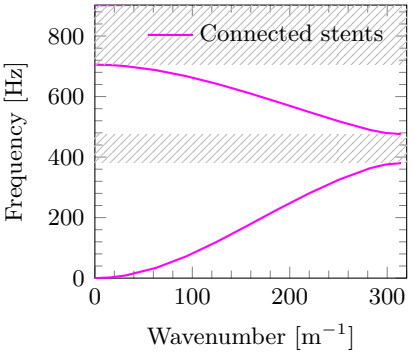

(f) *Unit cell with connected type A stents, flexural mode.*

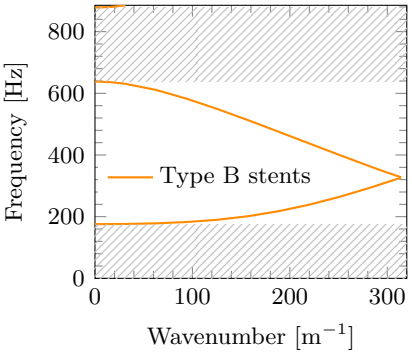

(g) *Unit cell with type B stents, mode involving simple flattening of the wall.*

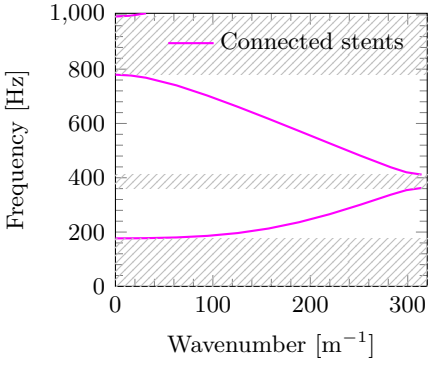

(h) *Unit cell with connected type A stents, mode involving simple flattening of the wall.*

Figure 3.8: Comparison of the dispersion curves for the axisymmetric mode (c)-(d), the flexural mode (e)-(f), and for the mode involving simple flattening of the wall (g)-(h), for the unit cell with different types of stents, (a) type B and (b) type A connected. The shaded zones denote the stop-bands.

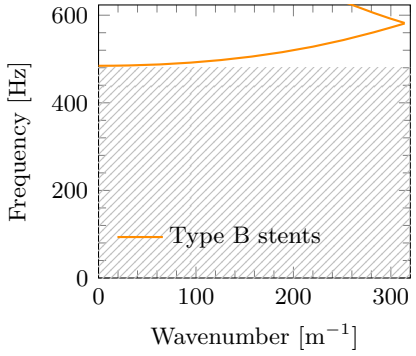

(a) *Unit cell with type B stents, mode involving trefoil flattening of the wall.*

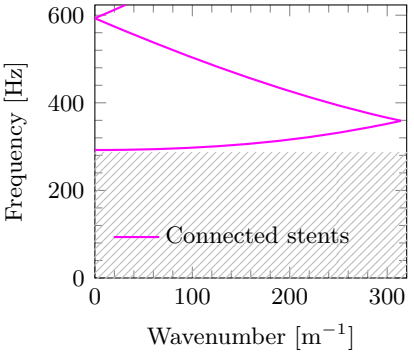

(b) *Unit cell with connected type A stents, mode involving trefoil flattening of the wall.*

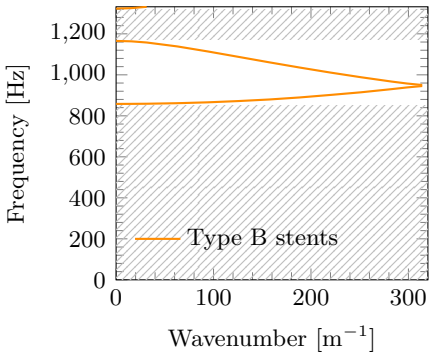

(c) *Unit cell with type B stents, mode involving quatrefoil flattening of the wall.*

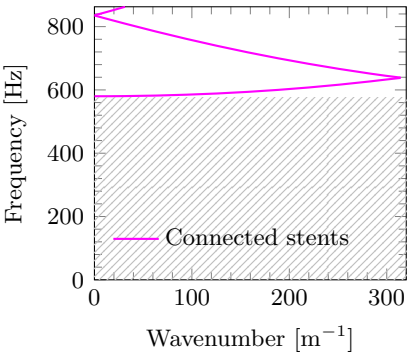

(d) *Unit cell with connected type A stents, mode involving quatrefoil flattening of the wall.*

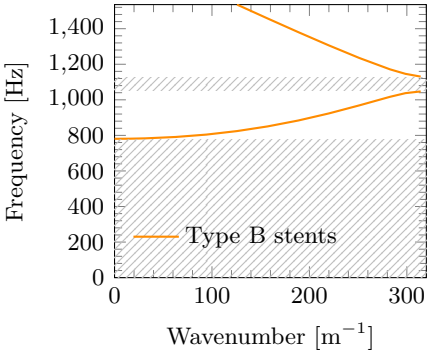

(e) *Unit cell with type B stents, flexural-torsional mode with rotation of the end sections.*

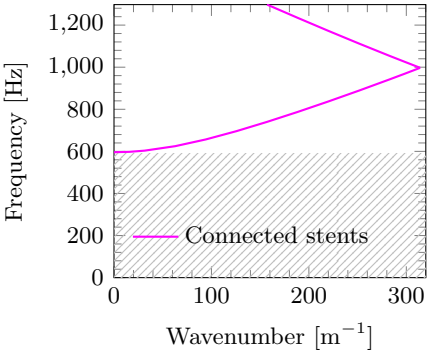

(f) *Unit cell with connected type A stents, flexural-torsional mode with rotation of the end sections.*

Figure 3.9: Comparison of the dispersion curves for the mode involving trefoil (a)-(b), and quatrefoil (c)-(d), and for the flexural-torsional modes with rotation of the end sections (e)-(f), for the unit cell with different types of stents. The shaded zones denote the stop-bands.

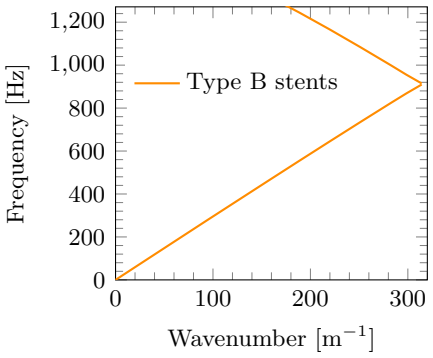

(a) *Unit cell with type B stents, torsional mode.*

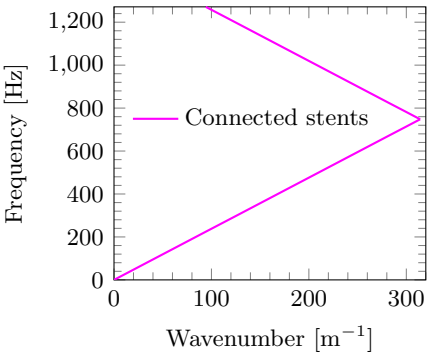

(b) *Unit cell with connected type A stents, torsional mode.*

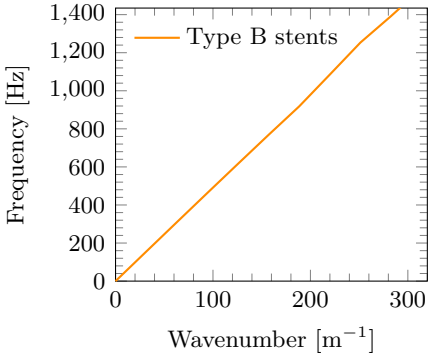

(c) *Unit cell with type B stents, axial mode.*

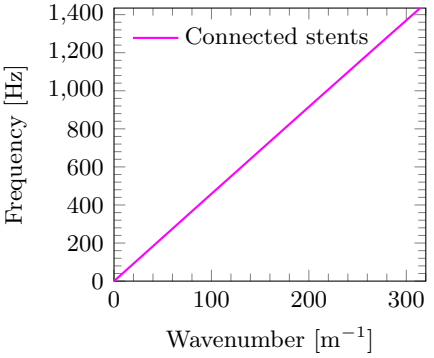

(d) *Unit cell with connected type A stents, axial mode.*

Figure 3.10: Comparison of the dispersion curves for the torsional mode (a)-(b), and for the axial mode (c)-(d), for the unit cell with different types of stents.

3.2 Bloch-Floquet formulation for the cluster of stents

The cases analysed in the previous section are representative of common stent designs, where a single stent is installed in the artery. Periodicity and geometry of the reinforcements in the vessel can affect the dynamic response of the system in terms of wave propagation. Hence, the question of finding particular geometries and patterns inducing stop-bands at low frequency regimes arises. Clinical experience shows that it is extremely rare for just one area of a diseased artery to be affected. It is not unusual for several small areas within one artery to have profound luminal reduction or a much longer segment affected. This raises the question as to whether it is better to put in multiple small stents or one long stent to treat several areas of disease at once. The case of multiple stents provides a different and very interesting pattern of the reinforcement of the vessel, linked to the periodicity of the structure, as shown by Papathanasiou *et al.* [96].

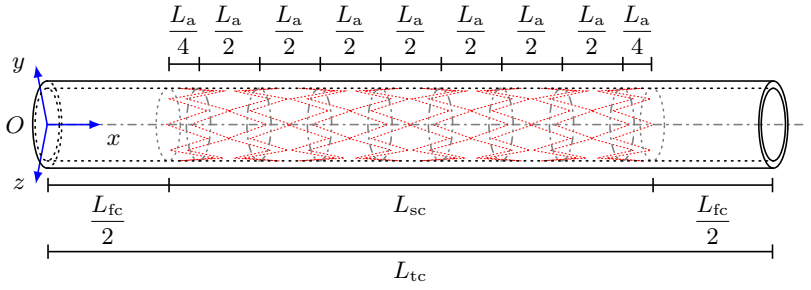

(a) *Unit cell employed in the computations.*

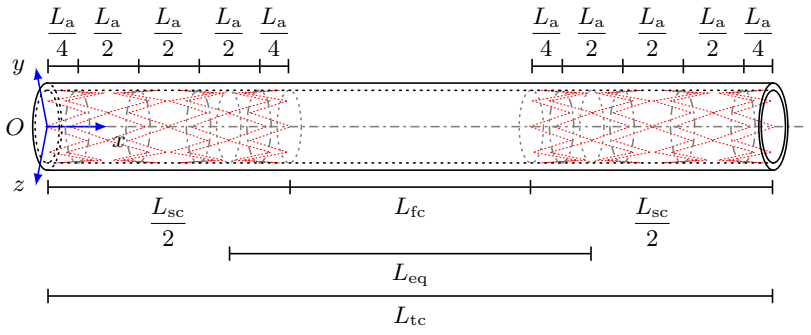

(b) *Alternative unit cell, equivalent to (a).*

Figure 3.11: Geometry of the unit cell for the cluster of type A stents. Part (b) shows clearly the spacing between the groups of coils, whereas part (a) shows the length of the repeated stented zone. Part (b) illustrates the length L_{eq} of the shell employed in the semi-analytical model shown in Figure 3.13a.

In this section, an in-depth investigation of the case in which more stents are installed in different sections of the arteries is provided for the three-dimensional model, thus generalising the one-dimensional analysis by Papathanasiou *et al.* [96]. To this purpose, a unit cell is composed of a finite-length stent (denoted by L_{sc}) and unstented section of the artery, which is then repeated periodically with a specific spacing L_{fc}. The geometry of this system is shown in detail in Figure 3.11, where type A stents are used. The total length L_{tc} of such a unit cell is equal to 60 mm and the length L_{fc} of the stent free zone

is equal to 20 mm. Two equivalent unit cells can be employed, and these are shown in Figures 3.11a and 3.11b.

3.2.1 Numerical simulations

The dispersion curves obtained from the Bloch-Floquet analysis are shown in Figure 3.12. It can be noted that for the axisymmetric mode (Figure 3.12a) there are two additional stop-bands appearing in the low frequency regime, but the width of these stop-bands is much smaller compared with those determined for type A, type B, and type A connected stents (see Figures 3.5c, 3.8c, and 3.8d). Similarly, a narrow stop band appears in the low frequency regime for the flexural mode (Figure 3.12b), which is smaller than the first stop-band appearing for type A, type B, and type A connected stents (see Figures 3.5e, 3.8e, and 3.8f).

For the simple flattening of the wall (Figure 3.12c), the dispersion curves have a slope close to zero, so they represent standing waves and/or waves with a very small group velocity. This means that energy is not transmitted through the system. The deformation modes corresponding to the standing waves, illustrated in Figure 3.12c, show that the deformation occurs only within the zones separating the groups of stents (Figure 3.12d). Therefore, the system behaves similarly to a simplified system composed of a fluid-filled cylinder with a length $L_{\text{eq}} = 30\,\text{mm}$, indicated in Figure 3.11b. Appropriate boundary conditions need to be applied at the end sections of this equivalent system. In particular, the deformation modes associated with the (quasi-)zero slope dispersion curves for the cluster of stents suggest the application of simply supported boundary conditions. The resonant frequencies of the equivalent system, corresponding to the standing waves for the cluster of stents, can be determined analytically as discussed in the next section.

Figure 3.12d shows that exponential localization and flattening of the arterial wall can occur in the unstented section. This can lead to slight change in the shape of the lumen and subsequently influences the blood flow at higher frequencies.

3.2.2 Semi-analytical model

The frequencies corresponding to standing waves and to small group velocity waves, determined numerically in Section 3.2.1, can be also estimated analytically by approximating the arterial wall as a finite elastic shell with the simply supported boundary conditions at the ends. The thin shell theory is employed here, together with the assumption of small displacements. The fluid exerts pressure on the artery wall. The equivalent cylindrical shell has thickness h_{eq}, radius of the middle surface R_{eq}, and length L_{eq}. The reference system (x, θ, r) is depicted in Figure 3.13, where the x-axis is the axis of the shell. The components of the displacement field $\boldsymbol{u} = u\boldsymbol{e}_x + v\boldsymbol{e}_\theta + w\boldsymbol{e}_r$ of the middle surface of the shell are aligned with the local x, θ, r directions respectively.

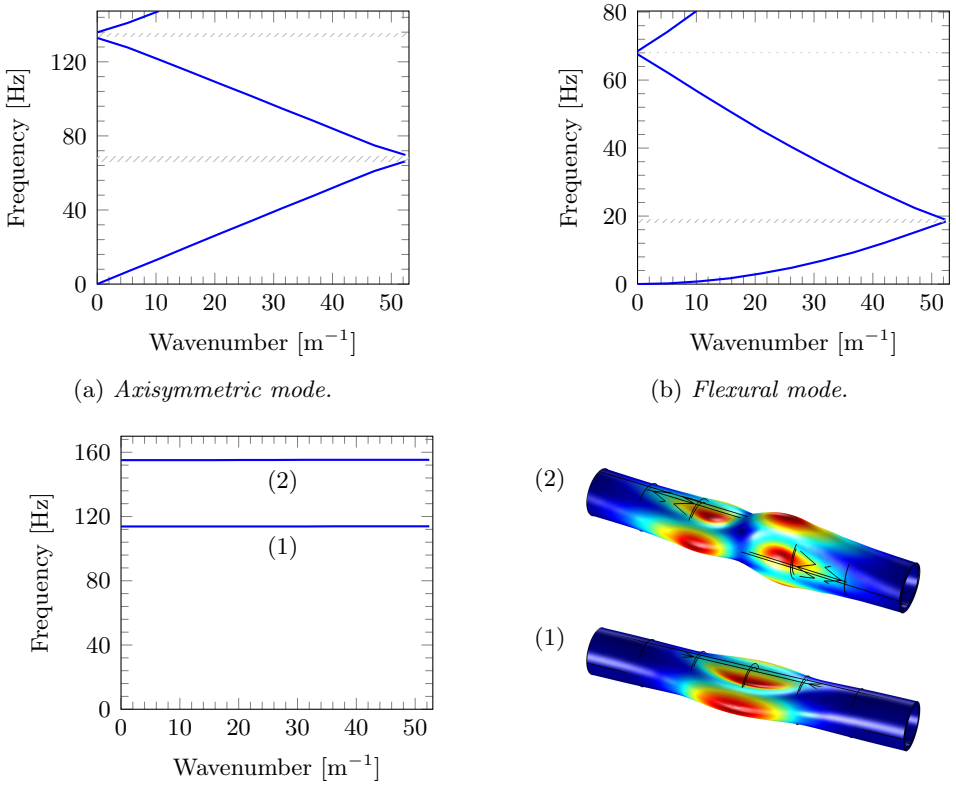

(a) *Axisymmetric mode.*

(b) *Flexural mode.*

(c) *Modes corresponding to standing waves.*

(d) *Localised modes occurring within the arterial wall between the stents.*

Figure 3.12: Dispersion curves for the cluster of stents.

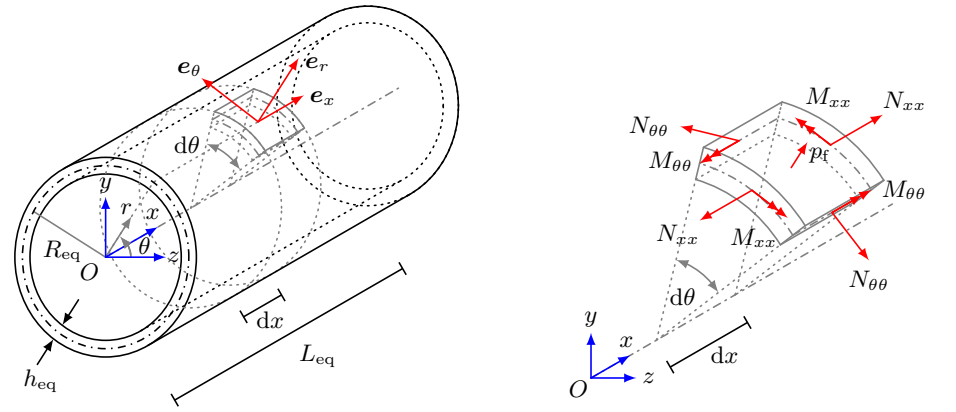

(a) *Cylindrical shell and its reference system.*

(b) *Generalised stresses acting on the middle surface of the shell.*

Figure 3.13: Scheme of the unit cell modelled as a cylindrical shell (a) and of the generalised stresses acting on its middle surface (b). The length L_{eq} of the cylindrical shell is shown in Figure 3.11b.

3.2.2.1 Framework of the thin shell theory

The equations of motions for a cylindrical thin shell are found in numerous references including the books by Soedel [109] and Rao [101], and have the form

$$\frac{\partial N_{xx}}{\partial x} + \frac{1}{R_{\text{eq}}}\frac{\partial N_{x\theta}}{\partial \theta} = \rho_{\text{a}} h_{\text{eq}} \frac{\partial^2 u}{\partial t^2}\,, \tag{3.7a}$$

$$\frac{\partial N_{x\theta}}{\partial x} + \frac{1}{R_{\text{eq}}}\frac{\partial N_{\theta\theta}}{\partial \theta} + \frac{1}{R_{\text{eq}}}\frac{\partial M_{x\theta}}{\partial x} + \frac{1}{R_{\text{eq}}^2}\frac{\partial M_{\theta\theta}}{\partial \theta} = \rho_{\text{a}} h_{\text{eq}} \frac{\partial^2 v}{\partial t^2}\,, \tag{3.7b}$$

$$\frac{\partial M_{xx}}{\partial x^2} + \frac{2}{R_{\text{eq}}}\frac{\partial^2 M_{x\theta}}{\partial x \partial \theta} + \frac{1}{R_{\text{eq}}^2}\frac{\partial^2 M_{\theta\theta}}{\partial \theta^2} - \frac{N_{\theta\theta}}{R_{\text{eq}}} + f_r = \rho_{\text{a}} h_{\text{eq}} \frac{\partial^2 w}{\partial t^2}\,, \tag{3.7c}$$

where the external load f_r represents the fluid pressure at the fluid-solid interface, whereas the generalised stresses are given by

$$(N_{xx}, N_{\theta\theta}, N_{x\theta}) = \int_{-h_{\text{eq}}/2}^{h_{\text{eq}}/2} (\sigma_{xx}, \sigma_{\theta\theta}, \sigma_{x\theta})\, \mathrm{d}r\,, \tag{3.8a}$$

$$(M_{xx}, M_{\theta\theta}, M_{x\theta}) = \int_{-h_{\text{eq}}/2}^{h_{\text{eq}}/2} (\sigma_{xx}, \sigma_{\theta\theta}, \sigma_{x\theta}) r\, \mathrm{d}r\,. \tag{3.8b}$$

The moments are represented by M, and the forces by N. The constitutive equations for a linear elastic isotropic homogeneous material, relating the stress tensor $\boldsymbol{\sigma}$ in equation (3.8) to the strain tensor $\boldsymbol{\varepsilon}$, have the form

$$\begin{pmatrix} \sigma_{xx} \\ \sigma_{\theta\theta} \\ \sigma_{x\theta} \end{pmatrix} = \begin{pmatrix} Q_{11} & Q_{12} & 0 \\ Q_{12} & Q_{22} & 0 \\ 0 & 0 & Q_{66} \end{pmatrix} \begin{pmatrix} \varepsilon_{xx} \\ \varepsilon_{\theta\theta} \\ \varepsilon_{x\theta} \end{pmatrix}\,. \tag{3.9}$$

The non-zero components of the elastic matrix $\boldsymbol{Q}$ are

$$Q_{11} = Q_{22} = \frac{E_{\text{a}}}{1-\nu_{\text{a}}^2}\,, \quad Q_{12} = \frac{E_{\text{a}}\nu_{\text{a}}}{1-\nu_{\text{a}}^2}\,, \quad Q_{66} = \frac{Q_{11}-Q_{12}}{2} = \frac{E_{\text{a}}}{2(1+\nu_{\text{a}})}\,, \tag{3.10}$$

where E_{a} and ν_{a} are the Young modulus and the Poisson ratio of the shell's material (the artery), respectively. Following Love's theory, the components of the strain tensor $\boldsymbol{\varepsilon}$ introduced in equation (3.9) are defined in terms of the displacement field $\boldsymbol{u}$ as

$$\varepsilon_{xx} = \frac{\partial u}{\partial x} - \frac{\partial^2 w}{\partial x^2} r\,, \tag{3.11a}$$

$$\varepsilon_{\theta\theta} = \frac{1}{R_{\text{eq}}}\left(\frac{\partial v}{\partial \theta} + w\right) + \frac{1}{R_{\text{eq}}^2}\left(\frac{\partial v}{\partial \theta} - \frac{\partial^2 w}{\partial \theta^2}\right) r\,, \tag{3.11b}$$

$$\varepsilon_{x\theta} = \frac{\partial v}{\partial x} + \frac{1}{R_{\text{eq}}}\frac{\partial u}{\partial \theta} + \frac{1}{R_{\text{eq}}}\left(\frac{\partial v}{\partial x} - 2\frac{\partial^2 w}{\partial x \partial \theta}\right) r\,. \tag{3.11c}$$

Substituting equations (3.8)-(3.11) into equation (3.7) yields the following form for the equations of motions:

$$\begin{pmatrix} L_{11} & L_{12} & L_{13} \\ L_{21} & L_{22} & L_{23} \\ L_{31} & L_{32} & L_{33} \end{pmatrix} \begin{pmatrix} u \\ v \\ w \end{pmatrix} = \begin{pmatrix} 0 \\ 0 \\ -f_r \end{pmatrix}, \tag{3.12}$$

where L_{ij} $(i,j = 1,2,3)$ are the differential operators with respect to x, θ and t, given by

$$L_{11} = \frac{E_\mathrm{a} h_\mathrm{eq}}{(1-\nu_\mathrm{a}^2)} \frac{\partial^2}{\partial x^2} + \frac{E_\mathrm{a} h_\mathrm{eq}}{2(1+\nu_\mathrm{a}) R_\mathrm{eq}^2} \frac{\partial^2}{\partial \theta^2} - \rho_\mathrm{a} h_\mathrm{eq} \frac{\partial^2}{\partial t^2}, \tag{3.13a}$$

$$L_{12} = L_{21} = \frac{E_\mathrm{a} h_\mathrm{eq}}{2(1-\nu_\mathrm{a}) R_\mathrm{eq}} \frac{\partial^2}{\partial x \partial \theta}, \tag{3.13b}$$

$$L_{13} = -L_{31} = \frac{\nu_\mathrm{a} E_\mathrm{a} h_\mathrm{eq}}{(1-\nu_\mathrm{a}^2) R_\mathrm{eq}} \frac{\partial}{\partial x}, \tag{3.13c}$$

$$L_{22} = \frac{E_\mathrm{a} h_\mathrm{eq}}{2(1+\nu_\mathrm{a})} \left(1 + \frac{h_\mathrm{eq}^2}{12 R_\mathrm{eq}^2}\right) \frac{\partial^2}{\partial x^2} + \frac{E_\mathrm{a} h_\mathrm{eq}}{(1-\nu_\mathrm{a}^2) R_\mathrm{eq}^2} \left(1 + \frac{h_\mathrm{eq}^2}{12 R_\mathrm{eq}^2}\right) \frac{\partial^2}{\partial \theta^2} - \rho_\mathrm{a} h_\mathrm{eq} \frac{\partial^2}{\partial t^2}, \tag{3.13d}$$

$$L_{23} = -L_{32} = \frac{E_\mathrm{a} h_\mathrm{eq}}{(1-\nu_\mathrm{a}^2) R_\mathrm{eq}^2} \frac{\partial}{\partial \theta} - \frac{E_\mathrm{a} h_\mathrm{eq}^3}{12(1-\nu_\mathrm{a}^2) R_\mathrm{eq}^2} \frac{\partial^3}{\partial x^2 \partial \theta} - \frac{E_\mathrm{a} h_\mathrm{eq}^3}{12(1-\nu_\mathrm{a}^2) R_\mathrm{eq}^4} \frac{\partial^3}{\partial \theta^3}, \tag{3.13e}$$

$$L_{33} = -\frac{E_\mathrm{a} h_\mathrm{eq}^3}{12(1-\nu_\mathrm{a}^2)} \left(\frac{\partial^2}{\partial x^2} + \frac{1}{R_\mathrm{eq}^2} \frac{\partial^2}{\partial \theta^2}\right)^2 - \frac{E_\mathrm{a} h_\mathrm{eq}}{(1-\nu_\mathrm{a}^2) R_\mathrm{eq}^2} - \rho_\mathrm{a} h_\mathrm{eq} \frac{\partial^2}{\partial t^2}. \tag{3.13f}$$

The fluid is modelled as an acoustic medium, hence the equations of motions of the fluid can be expressed in the cylindrical coordinate system (x, θ, r) as

$$\frac{1}{r} \frac{\partial}{\partial r} \left(r \frac{\partial p_\mathrm{f}}{\partial r}\right) + \frac{1}{r^2} \frac{\partial^2 p_\mathrm{f}}{\partial \theta^2} + \frac{\partial^2 p_\mathrm{f}}{\partial x^2} = \frac{1}{C_\mathrm{f}^2} \frac{\partial^2 p_\mathrm{f}}{\partial t^2}, \tag{3.14}$$

where p_f is the fluid pressure, and C_f is the speed of sound in the fluid ($C_\mathrm{f} = \sqrt{K_\mathrm{f}/\rho_\mathrm{f}}$).

3.2.2.2 Time-harmonic regime

In the framework of the time-harmonic regime, the displacement field $\boldsymbol{u}$ of the shell can be expressed in the form of a travelling wave, associated with an axial wavenumber k_m and circumferential mode number n. The expression of the displacement field $\boldsymbol{u}$ is

$$u(x,\theta,t) = U e^{-k_m x} \cos(n\theta) \cos(\omega t), \tag{3.15a}$$

$$v(x,\theta,t) = V e^{-k_m x} \sin(n\theta) \cos(\omega t), \tag{3.15b}$$

$$w(x,\theta,t) = W e^{-k_m x} \cos(n\theta) \cos(\omega t), \tag{3.15c}$$

where ω is the radian frequency, and U, V, W are the wave amplitudes in the x, θ, r directions respectively. The associated form of the acoustic pressure field is expressed as

$$p_{\mathrm{f}} = P_{\mathrm{f}}\, e^{-k_m x} \cos(n\theta)\, \mathrm{J}_n(k_r r) \cos(\omega t)\,, \tag{3.16}$$

where P_{f} is the pressure amplitude of the acoustic fluid, k_r is the radial wavenumber, and $\mathrm{J}_n(k_r r)$ is the Bessel function of the first kind of order n. The radial wavenumber is related to the axial wavenumber by the relation

$$k_r = \sqrt{\frac{\omega^2}{C_{\mathrm{f}}^2} - k_m^2}\,. \tag{3.17}$$

3.2.2.3 Approximation of the trapped waveforms

The fluid-solid interaction is taken into account by imposing the following boundary condition in terms of equivalence between the acceleration of the fluid and the shell:

$$\left.\frac{\partial^2 w}{\partial t^2}\right|_{r=R_{\mathrm{eq}}} = \left.\frac{\partial v_{\mathrm{f}}}{\partial t}\right|_{r=R_{\mathrm{eq}}} = -\frac{1}{\rho_{\mathrm{f}}}\left.\frac{\partial p_{\mathrm{f}}}{\partial r}\right|_{r=R_{\mathrm{eq}}} \tag{3.18}$$

where v_{f} is the velocity of the fluid. Substituting equations (3.15c) and (3.16) into the boundary conditions (3.18) yields the pressure amplitude P_{f} of the acoustic fluid in the form

$$P_{\mathrm{f}} = \frac{\omega^2 \rho_{\mathrm{f}}}{k_r\, \mathrm{J}_n'(k_r R_{\mathrm{eq}})} W\,. \tag{3.19}$$

The displacement field (3.15) and the pressure amplitude (3.19) can be substituted into the equations of motions (3.12), so that the equations of motions of the coupled system can be written as

$$\begin{pmatrix} C_{11} & C_{12} & C_{13} \\ C_{21} & C_{22} & C_{23} \\ C_{31} & C_{32} & C_{33} \end{pmatrix} \begin{pmatrix} U \\ V \\ W \end{pmatrix} = \begin{pmatrix} 0 \\ 0 \\ 0 \end{pmatrix}\,, \tag{3.20}$$

where the elements C_{ij} are given by

$$C_{11} = \frac{E_\mathrm{a} h_\mathrm{eq}}{1-\nu_\mathrm{a}^2} k_m^2 + \frac{E_\mathrm{a} h_\mathrm{eq}}{2(1+\nu_\mathrm{a}) R_\mathrm{eq}^2} n^2 - \rho_\mathrm{a} h_\mathrm{eq}\, \omega^2 \,, \tag{3.21a}$$

$$C_{12} = \mathrm{i}\, \frac{E_\mathrm{a} h_\mathrm{eq}}{2(1-\nu_\mathrm{a}) R_\mathrm{eq}} n k_m = -C_{21} \,, \tag{3.21b}$$

$$C_{13} = \mathrm{i}\, \frac{E_\mathrm{a} h_\mathrm{eq} \nu_\mathrm{a}}{(1-\nu_\mathrm{a}^2) R_\mathrm{eq}} k_m = -C_{31} \,, \tag{3.21c}$$

$$C_{22} = \left(1 + \frac{h_\mathrm{eq}^2}{12 R_\mathrm{eq}^2}\right) \left[\frac{E_\mathrm{a} h_\mathrm{eq}}{(1-\nu_\mathrm{a}^2) R_\mathrm{eq}^2} n^2 + \frac{E_\mathrm{a} h_\mathrm{eq}}{2(1+\nu_\mathrm{a})} k_m^2\right] - \rho_\mathrm{a} h_\mathrm{eq}\, \omega^2 \,, \tag{3.21d}$$

$$C_{23} = C_{32} = \frac{E_\mathrm{a} h_\mathrm{eq} n}{(1-\nu_\mathrm{a}^2) R_\mathrm{eq}^2} \left[\frac{h_\mathrm{eq}^2}{12} \left(k_m^2 + \frac{n^2}{R_\mathrm{eq}^2}\right) + 1\right] \,, \tag{3.21e}$$

$$C_{33} = \frac{E_\mathrm{a} h_\mathrm{eq}}{(1-\nu_\mathrm{a}^2)} \left[\frac{1}{R_\mathrm{eq}^2} + \frac{h^2}{12} \left(k_m^2 + \frac{n^2}{R_\mathrm{eq}^2}\right)^2\right] - \rho_\mathrm{a} h_\mathrm{eq}\, \omega^2 + f_r \,, \tag{3.21f}$$

and the fluid loading term takes the form

$$f_r = -\frac{\rho_\mathrm{f}}{k_r} \frac{\mathrm{J}_n(k_r R_\mathrm{eq})}{\mathrm{J}_n'(k_r R_\mathrm{eq})} \omega^2 \,. \tag{3.22}$$

The assumption of simply supported ends (at $x = 0$ and $x = L_\mathrm{eq}$) yields the following boundary conditions

$$v = 0 \,, \quad w = 0 \,, \quad N_{xx} = 0 \,, \quad M_{xx} = 0 \,, \quad \text{at} \quad x = 0 \quad \text{and} \quad x = L_\mathrm{eq} \,. \tag{3.23}$$

In order to satisfy the boundary conditions (3.23), the axial wavenumber k_m is taken as

$$k_m = \frac{\pi m}{L_\mathrm{eq}} \,. \tag{3.24}$$

For (3.20) to have non-trivial solutions, the determinant of $\boldsymbol{C}$ must be equal to 0, so that the characteristic equation takes the form

$$F(m, n, \omega) = 0 \,. \tag{3.25}$$

3.2.2.4 Frequency comparison for the simplified structure

The term "simplified structure" is used here for a finite section of the blood vessel, of length L_eq between the stents. To observe the trapped waveforms, finite element analysis is also performed for the case when the appropriate boundary conditions are set at the edges of the finite section. These computations are compared with the results obtained from the semi-analytical shell model described above.

Equation (3.25) is used to obtain the natural frequencies of the fluid-filled shell that approximate the frequencies corresponding to the dispersion curves for the cluster of stents with zero or small slope. The second column of Table 3.2 summarises the first three frequencies for standing waves evaluated by means of the semi-analytical model. The

Table 3.2: Comparative results in terms of frequency between the semi-analytical model and the finite element analysis for the determination of the standing waves within the cluster of stents. In the semi-analytical model, the results refer to the case $n = 2$ assuming length $L_{\text{eq}} = 30\,\text{mm}$, radius $R_{\text{eq}} = 4\,\text{mm}$, and thickness $h_{\text{eq}} = 0.7\,\text{mm}$.

m	Bloch-Floquet approach [Hz]	Finite structure		
		Semi-analytical model [Hz]	Simplified structure (solid) [Hz]	Simplified structure (shell) [Hz]
1	113.82	120.94	107.23	121.01
2	155.08	156.29	146.61	160.35
3	206.77	225.96	216.98	226.29

results are compared with the frequencies obtained through two finite element models of the simplified structure described in this section. In particular, in the first model the artery is modelled as a three-dimensional solid, whereas in the second model the artery is modelled as a shell.

The first column in Table 3.2 corresponds to standing waves, with quasi-periodicity boundary conditions set on the edges of the elementary cell. The third column corresponds to a finite hollow cylinder, whose displacements at the edge boundaries are equal to zero. The fourth column is produced from the finite element computations for the elastic shell in the framework of the Kirchhoff-Love shell theory, with the simply supported edges of the finite section of the blood vessel.

A comparison between the semi-analytical model and the simplified structure where the artery is modelled as a shell (columns 2 and 4 of the Table 3.2) shows that there is a good agreement between the two models. On the other hand, the model in which the artery is treated as a three-dimensional solid shows a small difference (compared with the approximation based on the shell theory in column 4 of Table 3.2) in the values of the frequencies corresponding to standing waves. This difference is associated with the choice of the fixed displacement boundary conditions at the edges of the thin-walled solid used in the calculations. Furthermore, it can be noted that the values obtained from the finite three-dimensional structure are closer to those obtained from the Bloch-Floquet analysis for the cluster of stents (column 1 of the Table 3.2). The values of the frequencies estimated using the semi-analytical model provide a good approximation for the standing waves frequency characterised by exponential localisation within the unstented arterial wall.

3.3 Transmission problem

In this section, the transmission problem for the single stent and for the cluster of stents of finite-length is presented. The material properties employed for the models discussed in this section are reported in Table 3.1. In both cases, a pressure with amplitude $p_0 = 2.6\,\text{kPa} \approx 20\,\text{mmHg}$ is applied at $x = 0$, and it generates a wave which propagates from the left-hand side to the right-hand side of the finite-length system (see Figures 3.14a

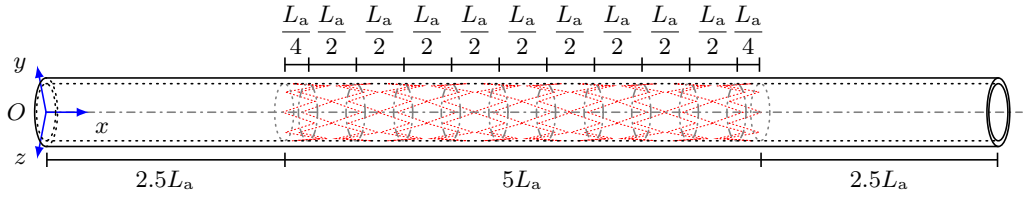

(a) *Scheme of the finite-length structure.*

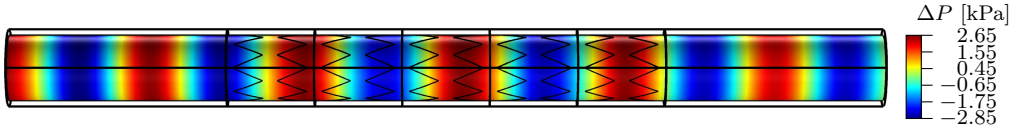

(b) *Map of the pressure within a pass-band at* 400 Hz.

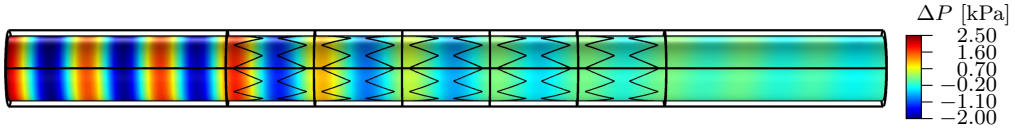

(c) *Map of the pressure within a stop-band at* 650 Hz.

Figure 3.14: Scheme of the finite-length structure employed in frequency response analysis for type A stents. The system is based on the repetition of five unit cells of type A stents illustrated in Figure 3.3b, where two sections of unstented artery are present at the left and at right ends. The pressure field is shown in (b) and (c).

and 3.15a). Zero displacement boundary conditions are applied to the end sections of the artery.

The analysis is performed in the following way. In the first step, the response of the system is investigated within the frequency range corresponding to a pass-band. In the second step, the investigation is restricted to a frequency range corresponding to the first stop-band of the system related to the axisymmetric mode, which was determined in Section 3.1.5 (see Figure 3.5c).

3.3.1 Single type A stent

The geometry for the case of a single type A stent is represented in Figure 3.14a, where the total length of the artery is equal to 100 mm. A type A stent composed of 10 coils spaced by a distance $L_a/2 = 5$ mm is inserted in the middle of the artery, so that the left end and the right end are not supported by stents.

From Figure 3.14b, it can be noted that within the pass-band regime for the axisymmetric mode, waves can propagate without dissipation of energy and no reflection is detected; in this figure, the pressure field at the frequency of 400 Hz is shown. Conversely, waves having a frequency within the stop-band regime for the axisymmetric mode (ranging from 606.9 Hz to 692.1 Hz) cannot propagate through the system (Figure 3.14c).

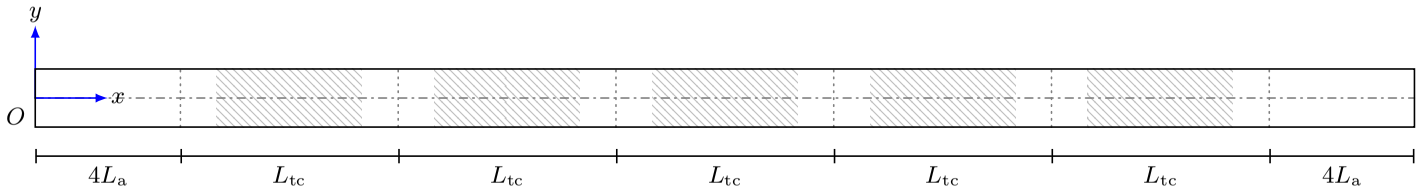

(a) *Scheme of the finite-length structure.*

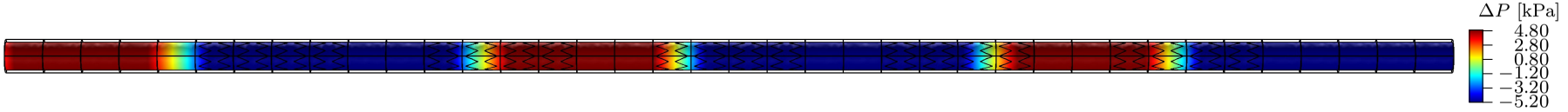

(b) *Map of the pressure within a pass-band at* 61 Hz.

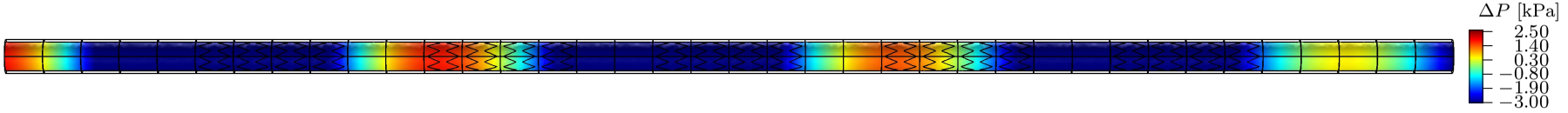

(c) *Map of the pressure within a stop-band at* 68 Hz.

Figure 3.15: Scheme of the finite-length structure employed in frequency response analysis. The system is based on the repetition of five unit cells of clusters of type A stents illustrated in Figure 3.11a, where two portions of artery without stents are positioned at the left and right ends. The pressure field is shown in (b) and (c).

3.3.2 Cluster of type A stents

The geometry for the case of a cluster of type A stents is represented in Figure 3.15a, where the total length of the artery is equal to 380 mm. The system is composed of five unit cells (each of length $L_{\mathrm{tc}} = 60\,\mathrm{mm}$) described in Figure 3.11a, where type A stents are employed. Additional sections of stent-free artery (length equal to $4L_{\mathrm{a}}$) are present at the left and at the right ends of the assembly of unit cells.

Similar to the case of a single stent, Figure 3.15b shows that waves can propagate without dissipation within the pass-band regime for the axisymmetric mode and no reflection is detected; in this figure, the effect of a wave of frequency 61 Hz is illustrated. Conversely, waves having a frequency inside the stop-band regime cannot propagate through the system (Figure 3.15c). In the latter case, where the frequency of the wave is equal to 68 Hz, the decrease in pressure amplitude is less evident because the stop-band width for the axisymmetric mode of this system (ranging from 66.3 Hz to 69.7 Hz) is narrower compared with that of the single stent (606.9 Hz to 692.1 Hz).

3.4 Response of the system in the transient regime

The pulsatile nature of flow varies in the arterial tree with a dependence on the anatomical position and the resistance in its draining arterial bed (organs supplied). The vessel calibre (diameter of the lumen) differs depending upon anatomical location and the blood flow required at times of activity or rest. The arteries are also subjected to the effects of human activities including low frequency walking or running, as well as higher frequencies such as riding in vehicles. This means that evolution of the pulsatile flow can play an important role in the behaviour of a stented artery. Therefore, a further investigation in the framework of the transient regime is required to complete the dynamic analysis of the stented artery. This can improve the understanding of failure when changes in the wave propagation and stress occur, and can help to explain the observed tissue reactions to the stent placements reported by Schillinger *et al.* [106, 107].

3.4.1 Computational transient framework

A computational model is developed for the analysis of a finite-length artery in the transient regime. In the first step, transient regime analysis is performed for an idealised straight artery without stents; in the second step, the analysis is performed for the same artery where type B stents are installed, and a comparison of the results is provided.

The artery is modelled as a hollow cylinder, whose length is 100 mm, with inner and outer diameters equal to 7.3 mm and 8.7 mm, respectively. Zero displacement boundary conditions are applied to the end sections of the artery. In the case of a stented artery, the vessel is reinforced with 10 coils, whose spacing is equal to 5 mm, placed in the centre of the system, thus providing the geometry represented in Figure 3.14a, where type A stents are replaced with type B stents. In a change from the previous section of this text, the stents are modelled as three-dimensional solids with square cross-section

($0.1\,\mathrm{mm} \times 0.1\,\mathrm{mm}$). Therefore, equations of motions (3.1) are used for the artery and for the stents, whereas the complete Navier-Stokes equations are employed to model the fluid (blood). The Navier-Stokes equations are written as

$$\frac{\partial \boldsymbol{v}_\mathrm{f}}{\partial t} + (\boldsymbol{v}_\mathrm{f} \cdot \nabla)\, \boldsymbol{v}_\mathrm{f} + \frac{\nabla p_\mathrm{f}}{\rho_\mathrm{f}} - \frac{\mu_\mathrm{f}}{\rho_\mathrm{f}} \nabla^2 \boldsymbol{v}_\mathrm{f} = \boldsymbol{0}\,, \tag{3.26}$$

where $\boldsymbol{v}_\mathrm{f}$ is the velocity field of the fluid and μ_f is the dynamic viscosity.

3.4.1.1 Material properties and boundary conditions

Consistent with the analysis reported in the previous sections, linear elastic isotropic homogeneous materials are employed for the artery and the stents. The material properties of the artery and of the stents are reported in Table 3.1. The blood is modelled as a viscous incompressible fluid of density $1050\,\mathrm{kg\,m^{-3}}$ and of dynamic viscosity $0.003\,\mathrm{Pa\,s}$.

The continuity of the displacements and tractions between the stents and the artery is applied at the interface corresponding to the external surface of the stent and the inner surface of the artery. It is assumed that the inlet and the outlet surfaces of the fluid are positioned at $x = 0\,\mathrm{mm}$ and at $x = 100\,\mathrm{mm}$, respectively.

Full coupling between the fluid and the structure is taken into account. Coupling is provided by means of condition (3.3), which involves a relation between the fluid pressure and the stress in the artery, together with the following relation between the velocity of the fluid and the displacement of the artery

$$\boldsymbol{v}_\mathrm{f} = \frac{\partial \boldsymbol{u}_\mathrm{a}}{\partial t}\,, \tag{3.27}$$

representing the no-slip boundary condition for the viscous fluid.

3.4.1.2 Initial conditions

At the initial time $t = 0\,\mathrm{s}$, the whole system is at rest. Furthermore, a velocity field $\boldsymbol{v}_0$ is applied to the fluid at the inlet. The magnitude of the initial inlet mean velocity $v_{\mathrm{m},0}$ is equal to $0.2\,\mathrm{m\,s^{-1}}$ and laminar flow regime is assumed, whereas the outlet pressure is assumed to equal zero. In a first phase, representing the initialisation of the flow, the inlet velocity is assumed constant (namely, $\boldsymbol{v}(t) = \boldsymbol{v}_0$, hence $v_\mathrm{m}(t) = v_{\mathrm{m},0}$) in order to reach the steady-state condition at a certain time t_0. During this phase, the velocity profile of the flow takes the form of a circular paraboloid, corresponding to the Poiseuille flow. The maximum velocity of this profile is equal to $0.4\,\mathrm{m\,s^{-1}}$. A distribution p_c, representing the shape of a circular paraboloid, is applied to the inlet velocity field in order to facilitate the system to reach the steady-state regime. In particular, for the system depicted in Figure 3.14a the distribution p_c is expressed as

$$p_\mathrm{c} = 1 - \frac{y^2 + z^2}{R_\mathrm{a}^2}\,, \tag{3.28}$$

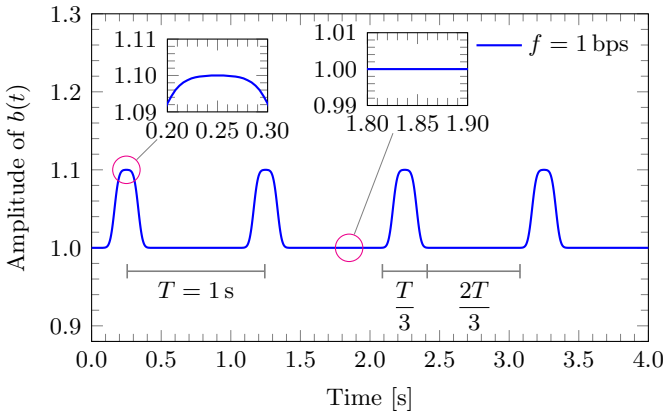

Figure 3.16: Graph of the function $b(t)$ expressed by (3.31) for $A_0 = 1$, $\Delta A = 0.1$, and $n = 20$.

where R_a is the inner radius of the artery, y and z are the Cartesian coordinates describing the inlet surface at $x = 0\,\mathrm{mm}$. Therefore, the initial inlet velocity field can be expressed as

$$\boldsymbol{v}_0 = 2v_{\mathrm{m},0}\, p_\mathrm{c}\, \boldsymbol{e}_x\,, \tag{3.29}$$

where $\boldsymbol{e}_x$ is the unit vector oriented along the x-axis, which is the axis of the artery.

3.4.1.3 Pulsating flow

After reaching the steady-state regime, pulsating flow inlet conditions are assumed ($\boldsymbol{v}(t) \neq \boldsymbol{v}_0$ for $t \geq t_0$) as follows. An idealised pulsation representing the variation of inlet velocity is expressed in terms of Gaussian approximations and corresponds to 4 beats per second. This beat-rate, corresponding to 240 bpm, is representative of patients affected by tachycardia. It should be noted that the interest is focussed on some of the frequencies composing the pulsation signal, which might be attenuated by the stent structure. The idealised pulsation is chosen as a continuous function approximating the velocity profile in an artery (see for instance Figure 1 in the paper by Li and Kleinstreuer [71]).

In the time-amplitude plane, the shape of this pulsation profile is flat (corresponding to the initial inlet mean velocity $v_{\mathrm{m},0}$) for approximately two thirds of the period, whereas, in the remaining part of the period, there is the variation from $v_{\mathrm{m},0}$ to the maximum peak (assumed to be equal to $1.1v_{\mathrm{m},0}$), and back again to $v_{\mathrm{m},0}$ (the same holds for the velocity field), thus representing the beat.

The pulsation is defined by a smooth function, which is periodically extended for all values of the time variable t. On a fixed interval, this function is approximated by a linear combination of "shifted" Gaussians. In particular, it can be noted that for a sufficiently large N the function

$$\mathrm{Const} \sum_{k=-2N}^{2N} e^{-(t-k)^2} \tag{3.30}$$

approximates a function, which is constant in the interval $t \in (-N/2, N/2)$, and decays exponentially fast when $|t| > 2N$. This function is infinitely differentiable and is fully suitable for approximating smooth pulses in the transient model. The desired pulsation is obtained by means of a distribution $b(t)$ applied to the constant velocity field $\boldsymbol{v}_0$. The expression employed for the pulsating inlet velocity profile is

$$b(t) = A_0 + \Delta A \left(\sum_{k=-n}^{n} \exp\left(-\frac{k^2}{72}\right) \right)^{-1} \sum_{j=0}^{m} \sum_{k=-n}^{n} \exp\left\{ -\frac{1}{72} \left[240 \left(ft - j - \frac{1}{4} \right) - k \right]^2 \right\}, \tag{3.31}$$

where A_0 is the initial amplitude (unit value is assumed), ΔA is the variation of the amplitude (assumed equal to 0.1), f is the number of beats per second, m denotes the total number of beats, and n corresponds to the number of the series elements approximating the flat zone ($n = 20$ provides a good approximation and has been used in the simulations). The function $b(t)$ in equation (3.31) is plotted in Figure 3.16. The inlet velocity field is expressed as

$$\boldsymbol{v}(t) = \begin{cases} \boldsymbol{v}_0 & t < t_0\,, \\ b(t)\boldsymbol{v}_0 & t \geq t_0\,. \end{cases} \tag{3.32}$$

Equation (3.32) provides the inlet condition that is applied in the computational model for the whole duration of the analysis.

The inlet velocity field $\boldsymbol{v}(t)$ provided in equation (3.32) is smooth in the time domain (b is infinitely differentiable with respect to time) and therefore more suitable for transient analysis computations. The analysis is performed for a total of 30 beats after the initialisation of the flow, which takes place at approximately 2.8 s.

The velocity field $\boldsymbol{v}(t)$ can potentially promote different vibration modes of the system, because it includes several harmonics. From the spectral analysis of the distribution $b(t)$ it can be noted that the amplitudes of the harmonics with a frequency higher than 32 Hz are already one tenth of the amplitude of the first harmonic. Similarly, the amplitudes of higher harmonics having a frequency above 60 Hz are already two orders of magnitude below that of the first harmonic. Hence, the inlet velocity field excites a broad range of frequencies, although only a few of them can be considered in practice, since the effect of the others becomes negligible.

In the case of a pulsation corresponding to 3 Hz but with a variation of amplitude ΔA equal to 0.5, the spectral analysis shows that harmonics having a frequency above 40 Hz are nearly two orders of magnitude below that of the first harmonic.

3.4.2 Computations of the fluid velocity and elastic deformation of the blood vessel

Figures 3.17 and 3.18 illustrate the speed of the fluid flow on the axis of the cylindrical vessel as a function of time for different inlet frequencies. A comparison between unstented

and stented blood vessels emphasises the different transient response of these systems to a pulsating flow. The computations are presented for the case of type B stents.

It is observed that in the pass-band region the overall transient response of the stented artery does not show localisation, and it converges to the time-harmonic mode slightly faster than in the case of the unstented softer system. It can be noted that for the case of the higher frequency shown in Figure 3.17, the profile of the displacement curve varies in transition from the unstented to stented case. This profile clearly indicates the variation of the velocity of the flow due to the presence of stents in the system.

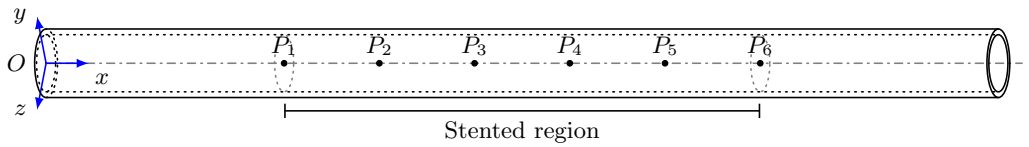

(a) *Scheme of the points in which the maximum fluid velocity is measured.*

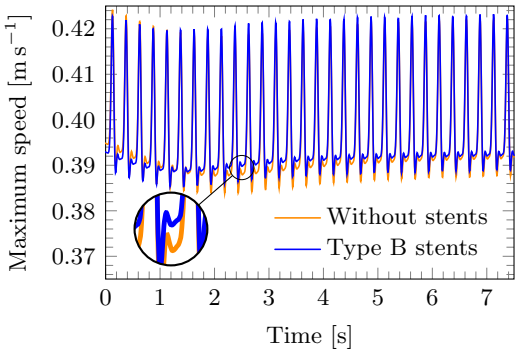

(b) *Point* P_1 *at* $x = 25\,\text{mm}$.

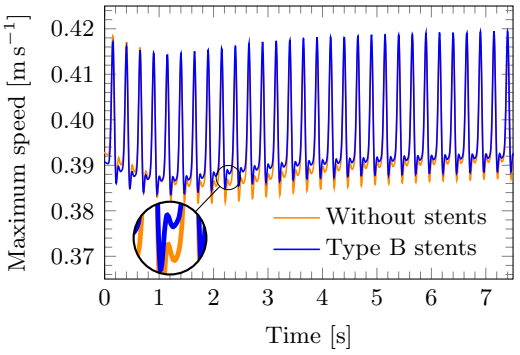

(c) *Point* P_2 *at* $x = 35\,\text{mm}$.

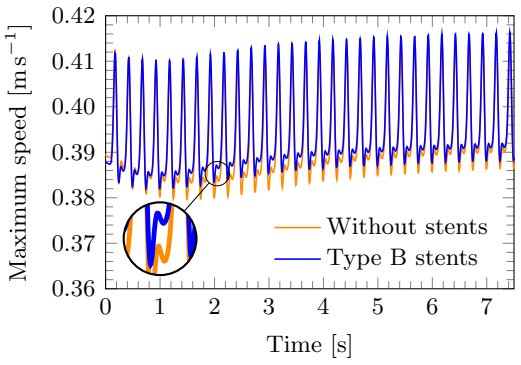

(d) *Point* P_3 *at* $x = 45\,\text{mm}$.

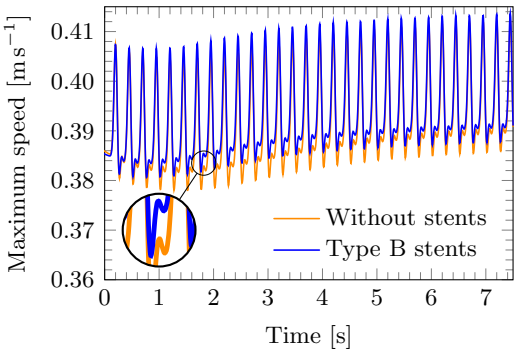

(e) *Point* P_4 *at* $x = 55\,\text{mm}$.

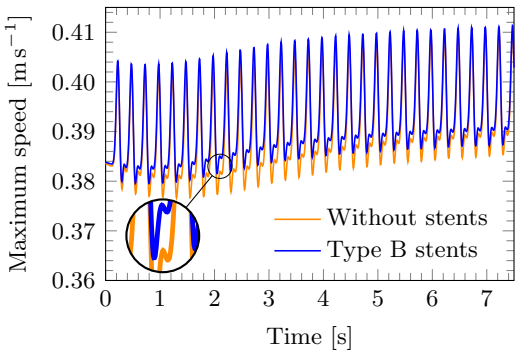

(f) *Point* P_5 *at* $x = 65\,\text{mm}$.

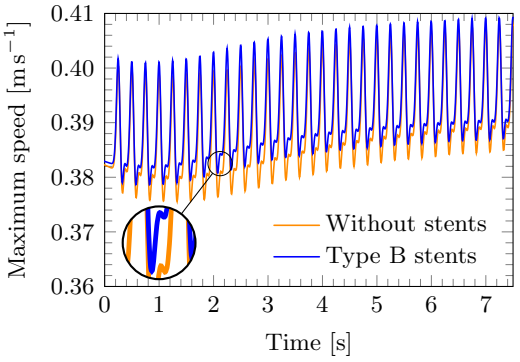

(g) *Point* P_6 *at* $x = 75\,\text{mm}$.

Figure 3.17: Evolution of the maximum fluid velocity at different points along the axis of the unstented artery and comparison with the case of a stented artery at 240 bpm, where the variation of amplitude ΔA is assumed equal to 0.1.

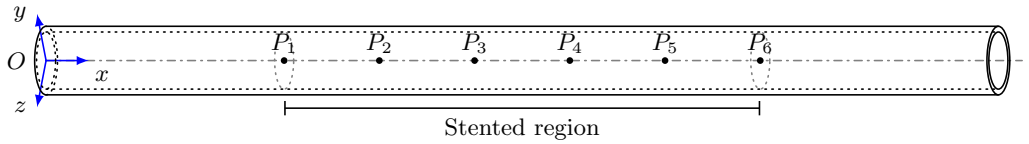

(a) *Scheme of the points in which the maximum fluid velocity is measured.*

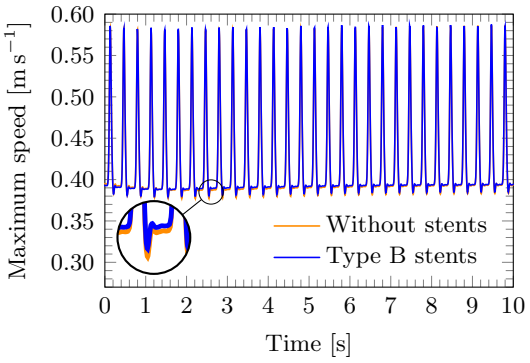

(b) *Point* P_1 *at* $x = 25\,\text{mm}$.

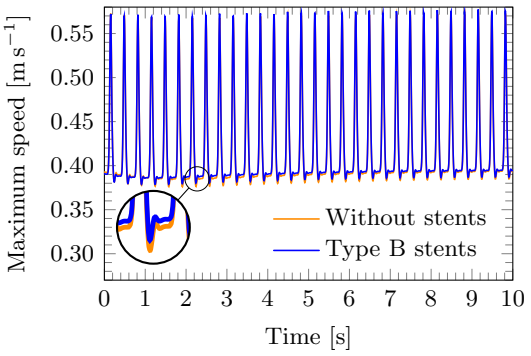

(c) *Point* P_2 *at* $x = 35\,\text{mm}$.

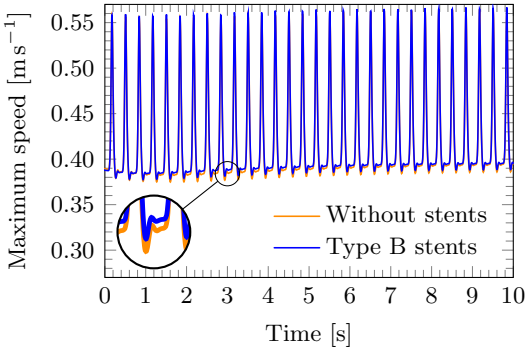

(d) *Point* P_3 *at* $x = 45\,\text{mm}$.

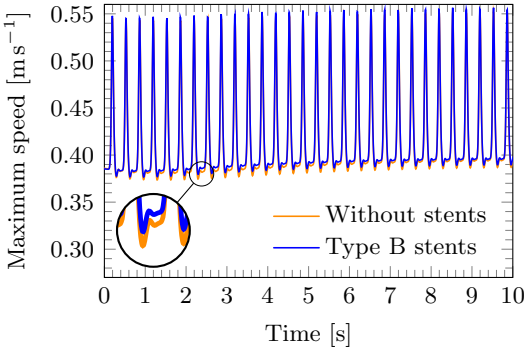

(e) *Point* P_4 *at* $x = 55\,\text{mm}$.

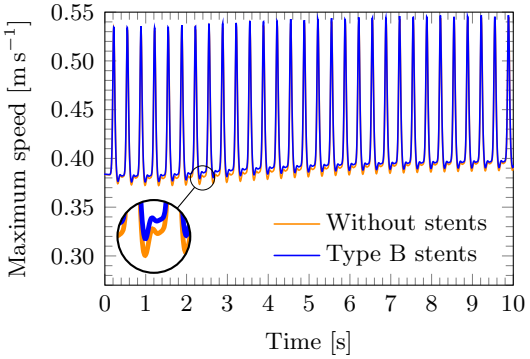

(f) *Point* P_5 *at* $x = 65\,\text{mm}$.

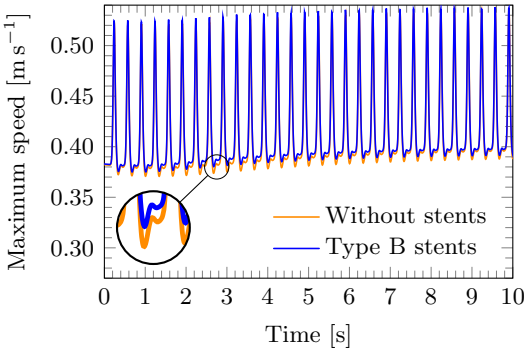

(g) *Point* P_6 *at* $x = 75\,\text{mm}$.

Figure 3.18: Evolution of the maximum fluid velocity at different points along the axis of the unstented artery and comparison with the case of a stented artery at 180 bpm, where the variation of amplitude ΔA is assumed equal to 0.5.

Chapter 4

Bloch-Floquet waves for a stented artery with plaque

The three-dimensional model presented in Chapter 3 is extended to the case of a stented artery in which the plaque is also considered. Generally, healthy arteries have smooth inner walls and blood flows through them easily. Some people, however, develop occluded (or clogged) vessels due to the build up of a substance called atherosclerotic plaque on the inner walls of the arteries. This arterial plaque is made from various substances that circulate in the blood including calcium, fat, cholesterol, cellular waste, and fibrin, a material involved in blood clotting as noted in the review by Topoleski and Stephen [113]. The plaque can reduce blood flow or, in some instances, block it altogether. In response to plaque build-up, cells in artery walls multiply and secrete additional substances that can cause the state of clogged arteries to deteriorate. As the plaque deposits grow, a condition that causes the arteries to narrow and harden called atherosclerosis results.

The aim of this chapter is to provide a preliminary analysis of the effect of plaque on the propagation of pressure waves in the artery before and after stent deployment. Various plaque geometries are considered. As explained by [113], atherosclerotic plaque is an extremely complex and highly variable tissue. Plaques may be broadly characterised as one of three types: cellular, hypocellular or calcified as described by Pericevic *et al.* [97], with stiffness increasing accordingly. Material parameters and geometries vary from one example to the next, and so their determination, and corresponding mechanical properties, are difficult to ascertain [113]. The calcified case is considered here and the observations of [113] are used to provide guidance for material property values for the models and simulations. Note that some equations from Chapter 3 are repeated here for the convenience of the reader.

4.1 Governing equations for the flow in a stented artery with plaque

In the following, subscripts 'a', 's', 'p', and 'f' in the equations denote the artery, the stent, the plaque and the fluid (blood), respectively. The arterial wall and the plaque are modelled using full three-dimensional linear elasticity equations of motion

$$\mu_{\mathrm{a}}\,\nabla^2\boldsymbol{u}_{\mathrm{a}} + (\lambda_{\mathrm{a}} + \mu_{\mathrm{a}})\nabla(\nabla\cdot\boldsymbol{u}_{\mathrm{a}}) = \rho_{\mathrm{a}}\frac{\partial^2\boldsymbol{u}_{\mathrm{a}}}{\partial t^2}\,, \tag{4.1}$$

$$\mu_{\mathrm{p}}\,\nabla^2\boldsymbol{u}_{\mathrm{p}} + (\lambda_{\mathrm{p}} + \mu_{\mathrm{p}})\nabla(\nabla\cdot\boldsymbol{u}_{\mathrm{p}}) = \rho_{\mathrm{p}}\frac{\partial^2\boldsymbol{u}_{\mathrm{p}}}{\partial t^2}\,, \tag{4.2}$$

where μ_{a}, λ_{a}, μ_{p} and λ_{p} are the Lamé parameters, ρ_{a} and ρ_{p} are the densities (mass per unit volume) of the artery and the plaque respectively, $\boldsymbol{u}_{\mathrm{a}}$ and $\boldsymbol{u}_{\mathrm{p}}$ are the displacement vectors, t is time, and $\nabla = (\partial/\partial x, \partial/\partial y, \partial/\partial z)^{\mathrm{T}}$ represents the vector differential operator.

As in Chapter 3 the blood is modelled as an acoustic medium, with the pressure p_{f}, which satisfies the wave equation

$$K_{\mathrm{f}}\,\nabla^2 p_{\mathrm{f}} = \rho_{\mathrm{f}}\,\frac{\partial^2 p_{\mathrm{f}}}{\partial t^2}\,, \tag{4.3}$$

where K_{f} is the bulk modulus of the fluid. The density of the blood is represented by ρ_{f}.

The coupling at the fluid-solid interface is given by the following relations for the tractions:

$$\boldsymbol{\sigma}_{\mathrm{a}}\,\boldsymbol{n} = -p_{\mathrm{f}}\,\boldsymbol{n}\,, \tag{4.4}$$

and

$$\boldsymbol{\sigma}_{\mathrm{p}}\,\boldsymbol{n} = -p_{\mathrm{f}}\,\boldsymbol{n}\,, \tag{4.5}$$

where $\boldsymbol{\sigma}_{\mathrm{a}}$ and $\boldsymbol{\sigma}_{\mathrm{p}}$ are the stress tensors in the artery wall and in the plaque, respectively, and $\boldsymbol{n}$ is the unit outward normal vector. The exterior boundary of the artery wall is free, which is defined by the condition

$$\boldsymbol{\sigma}_{\mathrm{a}}\,\boldsymbol{n} = \boldsymbol{0}\,. \tag{4.6}$$

The transmission conditions at the interface between the plaque and the arterial wall are standard and incorporate the continuity of displacements and tractions as follows:

$$\boldsymbol{\sigma}_{\mathrm{a}}\,\boldsymbol{n} = \boldsymbol{\sigma}_{\mathrm{p}}\,\boldsymbol{n}\,, \tag{4.7}$$

and

$$\boldsymbol{u}_{\mathrm{a}} = \boldsymbol{u}_{\mathrm{p}}\,. \tag{4.8}$$

The geometry of the cross-section of a partially blocked vessel is shown in Figure 4.1, with three examples of different percentages of the plaque cross-sectional areas, typically observed in clinical practice, shown. As discussed in the introduction to this chapter, the

elastic stiffness of the plaque is highly variable. Several models incorporating arterial and plaque material properties have been published, including those of Gleason *et al.* [44, 45] and Holfzapfel and co-workers [50, 52, 53]. As evidenced by the volume of literature dedicated to its study, the material and biomechanical behaviours of plaques are under constant scrutiny. Compressive stiffness depends on the type of plaque, with non-fibrous (atheromatous) plaques being the least stiff [113], followed by fibrous and then calcified plaques being the stiffest as reported by Topoleski *et al.* [114] and Maher *et al.* [75]. A summary of published stiffness ranges is provided by [113]; for cellular (and non-fibrous, atheromatous, haematoma-related), values range from 10kPa up to 1.4MPa; hypocellular (or fibrous) plaques have values ranging from 10 to 900kPa. The calcified cases, considered here, have measured values ranging from 70kPa up to 2.3GPa [113]. The specific calcified case, considered in the current modelling, is higher than the stiffness of the wall of the blood vessel, whereas the mass density of the plaque is significantly lower than the mass density of the arterial wall. Table 4.1 gives the values of the material parameters used in the numerical simulations.

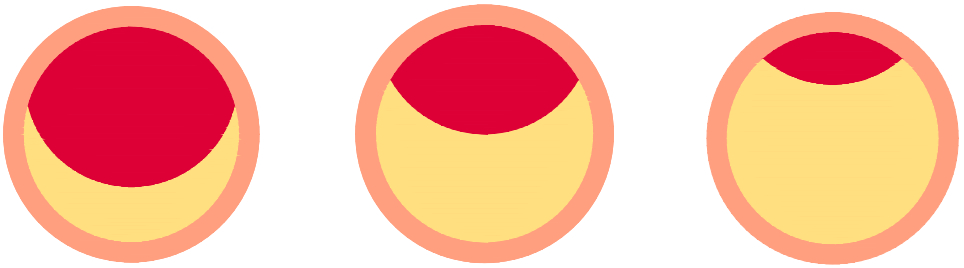

(a) (b) (c)

Figure 4.1: Variation of cross-sectional obstruction. The cross-sectional area of the channel of flow is reduced by (a) 31%,(b) 64%,(c) 85%.

Table 4.1: Materials parameters employed in the simulations of stented arteries in the presence of atherosclerotic plaque.

Properties	Materials		
	Artery	Stent	Plaque
Young Modulus	$E_a = 800\,\text{kPa}$	$E_s = 210\,\text{GPa}$	$E_p = 0.9\,\text{GPa}$
Poisson ratio	$\nu_a = 0.49$	$\nu_s = 0.3$	$\nu_p = 0.35$
Density	$\rho_a = 1200\,\text{kg m}^{-3}$	$\rho_s = 7800\,\text{kg m}^{-3}$	$\rho_p = 500\,\text{kg m}^{-3}$

As in the previous Chapter 3, the stent is modelled as a curved wire with a circular cross-section. The material is assumed to be linearly elastic, isotropic and homogeneous and its physical parameters are given in Table 4.1. The stents are in contact with the arterial wall or plaque and continuity of displacements and tractions is assumed at the corresponding interfaces. It is important to note that the stent has a periodic pattern, and although the mass density of the metal components is relatively large, the actual

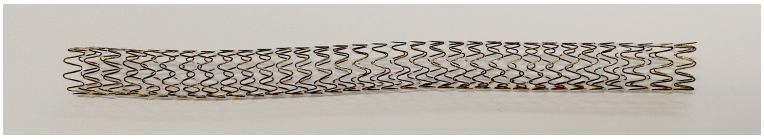

Figure 4.2: Photograph of a peripheral stent.

added inertia may vary for different stent designs. Figure 4.2 gives a typical geometrical design of a stent used in vascular surgery.

As in Section 3.1, the time-harmonic regime is assumed. Hence, the displacement fields in the artery, plaque and the stent, and the pressure field in the blood, are represented by the following equations:

$$\boldsymbol{u}_{\mathrm{a}}(\boldsymbol{x},t) = \boldsymbol{U}_{\mathrm{a}}(\boldsymbol{x})e^{i\omega t}\,, \tag{4.9a}$$

$$\boldsymbol{u}_{\mathrm{p}}(\boldsymbol{x},t) = \boldsymbol{U}_{\mathrm{p}}(\boldsymbol{x})e^{i\omega t}\,, \tag{4.9b}$$

$$\boldsymbol{u}_{\mathrm{s}}(\boldsymbol{x},t) = \boldsymbol{U}_{\mathrm{s}}(\boldsymbol{x})e^{i\omega t}\,, \tag{4.9c}$$

$$p_{\mathrm{f}}(\boldsymbol{x},t) = P_{\mathrm{f}}(\boldsymbol{x})e^{i\omega t}\,, \tag{4.9d}$$

where $\boldsymbol{U}_{\mathrm{a}}$, $\boldsymbol{U}_{\mathrm{p}}$ and $\boldsymbol{U}_{\mathrm{s}}$ denote the amplitude of the displacement vector for, respectively, the artery wall, plaque and stent, P_{f} is the pressure amplitude, and ω is the radian frequency.

Although most of the vascular processes are transient, in the analysis of a dynamic response of elastic systems it is useful to use the time-harmonic framework. Furthermore, resonant and localised waveforms are identified and, if required, the Fourier analysis can follow.

4.2 Bloch-Floquet waves for a partially blocked blood vessel containing plaque

In the time-harmonic regime, the analysis of Bloch-Floquet waves is a highly effective way to characterise the dispersion and localisation in periodic systems. In this section, the methodology developed throughout this research (Chapters 3- 5 here) and the associated publications by Frecentese *et al.* [36, 37, 120], is adopted. Namely, an elementary cell within the system is identified, and conditions at the transition boundaries of the cell are imposed to take into account the phase shift, corresponding to the wave, which has been transmitted through the cell. The implementation of the Bloch-Floquet quasi-periodicity conditions leads to the following equations:

$$\boldsymbol{U}_{\mathrm{a}}(x+L_{\mathrm{a}},y,z) = \boldsymbol{U}_{\mathrm{a}}(x,y,z)e^{iKL_{\mathrm{a}}}\,, \tag{4.10a}$$

$$\boldsymbol{U}_{\mathrm{p}}(x+L_{\mathrm{a}},y,z) = \boldsymbol{U}_{\mathrm{p}}(x,y,z)e^{iKL_{\mathrm{a}}}\,, \tag{4.10b}$$

$$\boldsymbol{U}_{\mathrm{s}}(x+L_{\mathrm{a}},y,z) = \boldsymbol{U}_{\mathrm{s}}(x,y,z)e^{iKL_{\mathrm{a}}}\,, \tag{4.10c}$$

$$P_{\mathrm{f}}(x+L_{\mathrm{a}},y,z) = P_{\mathrm{f}}(x,y,z)e^{ikL_{\mathrm{a}}}\,, \tag{4.10d}$$

where L_a is the length of the unit cell, k is the wavenumber, which is inversely proportional to the wavelength $\lambda = 2\pi/k$, and (x, y, z) is a point in the elementary cell, including the boundary, as for the case without plaque shown in Figure 3.2b.

As for the case with no plaque in Section 3.1.3, the wall of the vessel in the unit cell for the stented artery with plaque, is a hollow cylinder. However, the rest of the unit cell's geometry is far more complicated since the interior of the artery is no longer filled only with fluid representing the blood. As can be seen in Figure 4.1, the model now contains a mixture of blood and atherosclerotic plaque. The various cases are defined using a ratio of plaque to cross-sectional area of the channel; Figure 4.1a shows the case of a 31% reduction, Figure 4.1b shows 64% and Figure 4.1c illustrates the case of 85% cross-sectional area reduction due to the presence of plaque. Note that the obstructed channel of blood flow in these examples no longer has a circular cross-section. Additional cases for which a circular cross-section remains after the accumulation of plaque, which facilitated the deployment of stents in the analysis, were investigated and are shown in Figure 4.3.

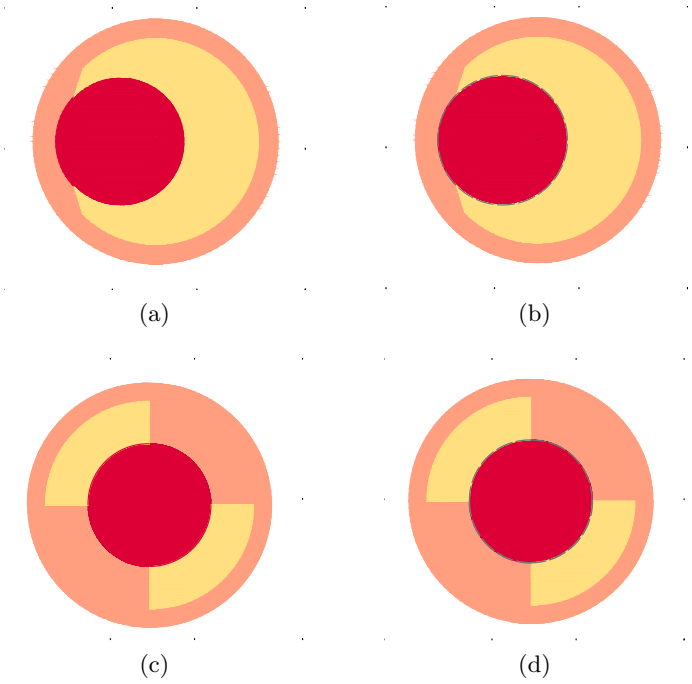

Figure 4.3: Different configurations of plaque for which the cross-sectional area of the channel is reduced to 40%. (a) unstented artery with 55% plaque shifted to one side and 5% arterial wall, (b) stented artery with plaque shifted to one side, (c) unstented artery with 30% plaque broken into two pieces and 30% arterial wall, (d) stented artery with two-piece plaque.

Figures 4.3a 4.3b show cases where the plaque is shifted to one side of the artery, and Figures 4.3c 4.3d illustrate the case of ruptured plaque which has been broken into two pieces. Note also that Figures 4.3b and 4.3d show the stents, which are zigzag-shaped coils characterised by eight crowns (16 segments), which are linked with four additional beam elements as shown in Figure 4.4.

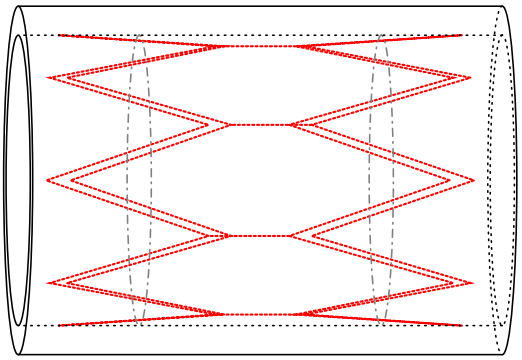

Figure 4.4: Unit cell with type A connected stents with four links.

4.2.1 Unstented arteries with plaque

The aim of this part of the study was to identify possible pass-bands and stop-bands for the coupled system composed of the unstented artery with plaque and the blood, via Bloch-Floquet analysis. The components of the coupled system are modelled as linear elastic isotropic homogeneous materials. As stated earlier, the elastic parameters are summarised in Table 4.1, and they correspond to representative values for the carotid artery and plaque [113, 114] and for metals commonly used for stents as reported by Tambaca *et al.* [111]. The blood is modelled as an acoustic medium of bulk modulus $K_{\mathrm{f}} = 2.4\,\mathrm{GPa}$ and density $\rho_{\mathrm{f}} = 1050\,\mathrm{kg\,m^{-3}}$.

Here the cases illustrated in Figure 4.1 are considered, where the cross-sectional area is reduced by 31%, 64% and 85%, respectively, and the length of the unit cell is L=10 mm. The dispersion diagrams are presented in Figure 4.5. The case of no plaque is shown in Figure 4.5a and this may be compared with the example of 31% plaque shown in Figure 4.5b. It is clear that the pass bands are elevated to higher frequencies in the presence of the plaque, and that there are no stop bands for either 0% or 31% plaque. One interesting feature related to the introduction of plaque is the change in the shape of the dispersion curves; the four curves emanating from the origin have much steeper initial gradients for the 31% plaque case than for the unblocked artery, before flattening at higher wavenumbers in the presence of the plaque. The unblocked arteries also have some curves with low gradients across the whole Brillouin zone, which are not observed for the plaque examples.

As the plaque is increased, similar trends are observed; the dispersion curves move to higher frequency values, as can be seen when comparing Figures 4.5b-4.5d. For highly occluded arteries, there are very few dispersion curves at low frequencies, as is clearly illustrated in Figure 4.5d, where the second point of the steepest dispersion curve emanating from the origin is at 350Hz for 85% plaque, compared with 210Hz for 64% in Figure 4.5c and 90Hz for 31% in Figure 4.5b. The case with no plaque shows a mode at around 30Hz for the corresponding dispersion curve shown in Figure 4.5a. No stop bands are seen at frequencies below 1kHz for these specific calcified plaque cases.

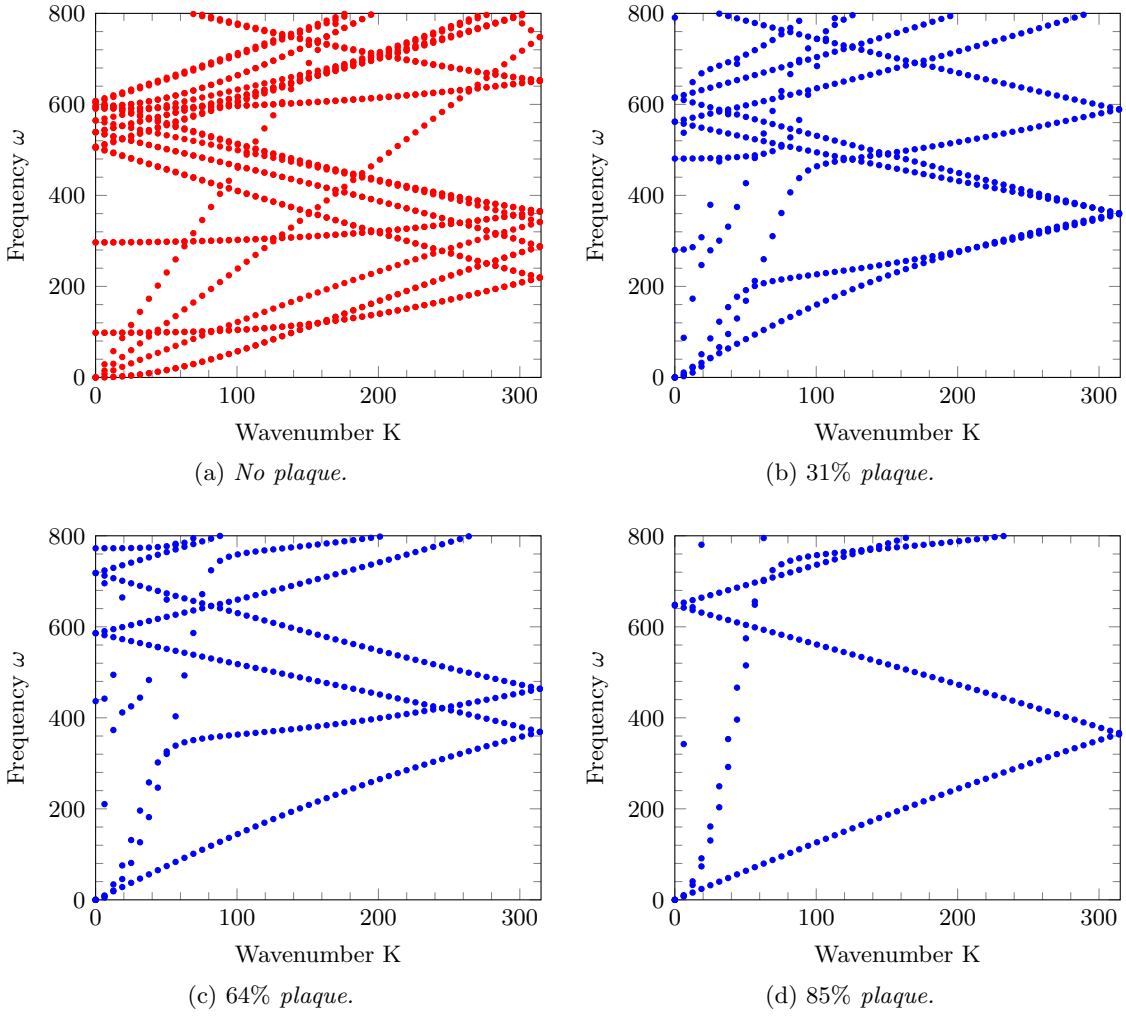

(a) *No plaque.* (b) 31% *plaque.*

(c) 64% *plaque.* (d) 85% *plaque.*

Figure 4.5: Dispersion curves for the cases of (a) no plaque, (b) 31% plaque, (c) 64% plaque and (d) 85% plaque.

Examples of the arterial modes arising for low frequencies are shown in Figure 4.6 for the cases of 31%, 64% and 85% plaque. Figure 4.6a occurs for 10.7Hz, Figure 4.6b corresponds to 9.4Hz and Figure 4.6c is observed for 16.0Hz. The modes are indicative of the arterial type, but as the plaque percentage increases, the surface area over which the mode is observed narrows, as one would expect for the increase in stiffness.

4.2.2 Stented arteries with plaque

The more complicated cases of Figure 4.3 were also analysed for trends in pass bands and stop bands. The circular cross-section of the fluid-filled portion of the unit cell allows for deployment of stents in the simulations. Figure 4.3a shows an artery where the cross-sectional area of the channel of flow has been reduced to 40%, the plaque occupies 55% of the channel, and the remaining 5% is arterial wall. A stent is attached to the inner wall of the channel, as shown in Figure 4.3b. This case is described as the shifted plaque case.

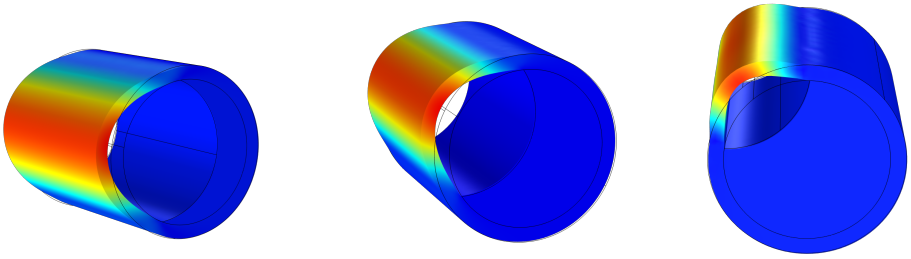

(a) (b) (c)

Figure 4.6: Modes corresponding to different percentage of plaque obstruction. (a) arterial mode at 10.7 Hz when the cross-sectional area is reduced by 31%,(b) arterial mode at 9.4 Hz when the cross-sectional area is reduced by 64%,(c) arterial mode at 16.0 Hz when the cross-sectional area is reduced by 85%.

An alternative geometry, for which the cross-sectional area has also been reduced to 40%, is illustrated in Figures 4.3c 4.3d, where the plaque occupies 30% of the channel of flow and is in two distinct sections. As many researchers have noted, the geometries of atherosclerotic plaques are highly variable [113]. Plaque may rupture, as reported by many authors including Falk [33], so it is possible for a configuration like that shown in Figure 4.3c to occur. This is labelled here as the two-piece plaque case.

The dispersion diagrams for the unstented and stented arteries (both with plaque) are shown in Figure 4.7, with parts (b) and (d) showing the stented system in both cases. The shifted plaque case is illustrated in Figures 4.7a- 4.7b, and a comparison of Figure 4.7a and 4.7b indicates that a stop band opens at around 1kHz upon the stent deployment. The partial stop band is fairly wide at the end of the Brillouin zone, covering a range of approximately 80Hz. The dispersion curves are similar in shape to the cases with more than 60% plaque shown in Figures 4.5c- 4.5d, and in their distribution over the frequency range. A comparison with the unblocked artery shown in Figure 4.5a once again shows that the presence of the plaque causes the bands to move up the frequency spectrum.

A similar observation may be made for the case of the two-piece plaque in Figures 4.7c-4.7d, although there are clearly more pass bands than for the shifted plaque case over the same range of frequencies, since there is only 30% plaque compared with 55%. Another difference is that the partial stop band opened at the end of the Brillouin zone upon stent deployment in Figure 4.7d is much narrower, covering less than 20Hz. Once again, flatter sections of dispersion curves have been moved to higher frequencies in the presence of plaque, when compared with the healthy artery. The two-piece plaque configuration also appears to show some local narrow band opening at around 1.2kHz in the centre of the Brillouin zone, when comparing the curves in Figures 4.7c and 4.7d.

A study on the effect of plaque for the Bloch-Floquet analysis of the stented artery problem has been presented here. The model shows that the plaque significantly affects the wave propagation in blood vessels, and the introduction of stents has an impact at high frequencies. The high variability of material parameters, mechanical properties and

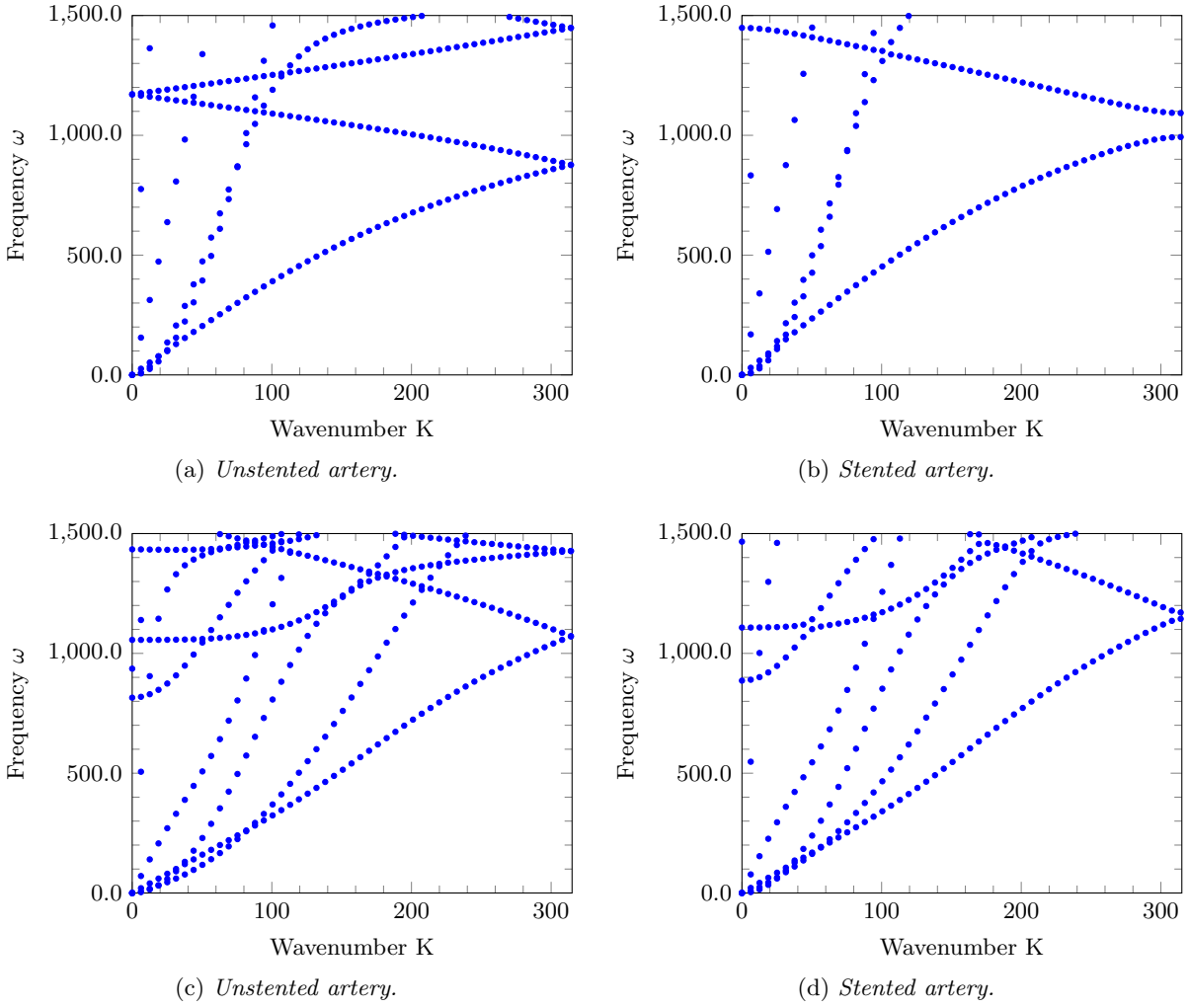

(a) *Unstented artery.* (b) *Stented artery.*

(c) *Unstented artery.* (d) *Stented artery.*

Figure 4.7: Dispersion curves for the cases of (a), (b) shifted plaque, and (c), (d) two-piece plaque.

geometries of plaques, indicates that the models may be refined in the future to provide more insight for clinically relevant cases and for medical practitioners.

Chapter 5

Semi-analytical approximations for waves in a stented artery

A preliminary one-dimensional approach to model wave propagation through a stented artery was developed in [96]. The paper by Papathanasiou *et al.* [96] presented an analytical model that takes into account the fluid-solid interaction in the framework of a transmission problem for a pulsating flow through a stented blood vessel. In the current chapter, based on the paper by Frecentese *et al.* [37], a new study based on Bloch-Floquet analysis is presented, which includes:

(i) calibration against the three-dimensional results of Chapter 3 and [36];

(ii) the modelling of stents with sparse structure;

(iii) the Bloch-Floquet analysis of waves in stented vascular systems.

A big attraction of a one-dimensional analytical model is the capability to quickly identify frequency regimes of interests, which can then be investigated in more detail using the three-dimensional model of Chapter 3, for instance. Techniques explained in the introductory theoretical background Chapter 2 are utilised in what follows, and will be referred to accordingly.

The structure of the chapter is as follows. Section 5.1 presents the one-dimensional model for a stented artery. Section 5.2 includes the calibration procedure for the one-dimensional model versus the three-dimensional blood vessel. The dispersion properties of the waves in stented systems for the one-dimensional model are also presented. The transmission problems for sparse stents are analysed in Section 5.3, with the comparison being made to the dispersion properties discussed in Section 5.2. The proposed model is employed in Section 5.4 extending the analysis to the case of two overlapping stents in an artery.

5.1 Governing equations for blood flow in stented arteries

Referring to the study presented in [96], a low Mach number is assumed and nonlinear effects are neglected. A flat velocity profile within each circular cross-section ensures that the pressure $p(x,t)$, and the velocity $u(x,t)$, are assumed to be constant over the cross-sectional area A of the blood vessel.

In the simplified approach, an inviscid fluid interacting with a linear cylindrical shell is considered. The linearised one-dimensional wave propagation model incorporates the mass and momentum conservation equations (see Chapter 2, Section 2.2 for more details), as follows:

$$\frac{\partial p}{\partial t} + c^2 \frac{\rho}{A} \frac{\partial q}{\partial x} = 0\,, \tag{5.1a}$$

$$\frac{\partial q}{\partial t} + \frac{A}{\rho} \frac{\partial p}{\partial x} = 0\,. \tag{5.1b}$$

Here x is the axial coordinate along the vessel, t is the time, A is the cross-sectional area, $q = Au$ is the volumetric flow, c is the speed of propagation of the pulse wave, and ρ is the fluid density, approximately constant for a nearly incompressible fluid.

The system (5.1a)- (5.1b) is reduced to the wave equation

$$\frac{\partial^2 q}{\partial t^2} - \frac{\partial}{\partial x}\left(c^2 \frac{\partial q}{\partial x}\right) = 0\,, \tag{5.2}$$

where c is constant in the homogeneous unstented artery, and $c = c(x)$ is variable in the stented region. In particular, for a cylindrical homogeneous artery, the value c_0 of the wave speed can be approximated (see, for example, the book by Tullis [115] and the paper by Tijsseling and Anderson [112]) as

$$c_0^2 \approx \frac{Eh}{2R\rho\psi}\,, \tag{5.3}$$

where E is the Young's modulus of the artery, h is the thickness of the arterial wall, R is the internal radius of the artery and ψ is a constant depending on the artery constraint.

For the stented region, alternative material properties must be considered. An additional wall stiffness due to the stent and the plaque is included in the model. Referring to (5.3), E, h and A are subject to variation. Assuming a reference wave speed c_0 for the healthy (unstented) artery, the wave speed $c(x)$ in the stented region is taken to be

$$c(x) = c_0 + c_A + c_B f(x)\,, \tag{5.4}$$

as proposed in [96]. Here c_A, c_B are constants, and $f(x)$ is a periodic function of period L:

$$f(x+L) = f(x)\,, \quad 0 \le f(x) \le 1\,. \tag{5.5}$$

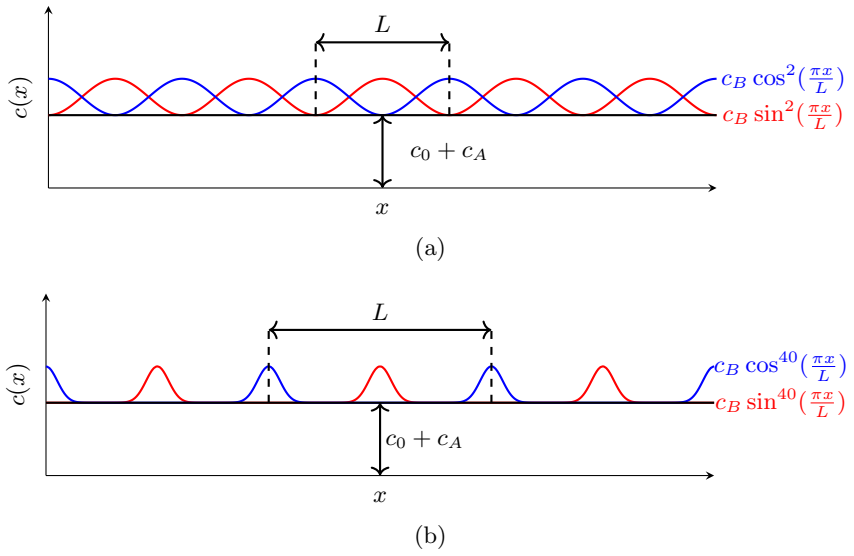

Figure 5.1: Examples of velocity profiles in a stented artery for different values of the exponent s in (5.6) and (5.7): (a) $s = 1$, (b) $s = 20$.

The constant c_A is the minimum variation from the healthy region value due to the stent and/or plaque, and c_B is associated with the maximum deviation, measured from the state $c_0 + c_A$, which occurs in the elementary cell.

Following the model proposed in [96], $c(x)$ is assumed to be either

$$c(x) = c_0 + c_A + c_B \sin^{2s}\left(\frac{\pi x}{L}\right), \tag{5.6}$$

or

$$c(x) = c_0 + c_A + c_B \cos^{2s}\left(\frac{\pi x}{L}\right), \tag{5.7}$$

which are illustrated in Figure 5.1 for two values of s. The exponent $s \in \mathbb{N}$ is a new feature of the model and characterises the sparse structure of the stent; it is considered for the first time here.

The non-dimensional variables are introduced as follows:

$$\xi = \frac{x}{L}, \quad \eta = \frac{c_0 t}{L}, \quad Q = \frac{q}{q_0}, \tag{5.8}$$

where L is the length of the periodic cell and q_0 is the reference value of the volumetric flow. Equation (5.2) becomes

$$\frac{\partial^2 Q}{\partial \eta^2} - \frac{\partial}{\partial \xi}\left(\left(\frac{c}{c_0}\right)^2 \frac{\partial Q}{\partial \xi}\right) = 0. \tag{5.9}$$

Using equations (5.6) and (5.7), in the stented area we have that

$$\frac{c(\xi)}{c_0} = \begin{cases} 1, & \xi \in (-\infty, 0) \\ 1 + A^2 + B^2 \sin^{2s}(\pi\xi) \text{ or } 1 + A^2 + B^2 \cos^{2s}(\pi\xi), & \xi \in (0, n) \\ 1, & \xi \in (n, +\infty), \end{cases} \tag{5.10}$$

where $A^2 = c_A/c_0$, $B^2 = c_B/c_0$, and n is the number of periodic cells constituting the stent.

The solution of equation (5.9) is sought in the form $Q = y(\xi)e^{-i\omega\eta}$, where the function $y(\xi)$ and the angular frequency ω satisfy the equation

$$\frac{d}{d\xi}\left(\left[1 + A^2 + B^2 f(\xi)\right]^2 \frac{dy}{d\xi}\right) + \omega^2 y = 0\,. \tag{5.11}$$

Introducing Y such that

$$Y = \left[1 + A^2 + B^2 f(\xi)\right]^2 \frac{dy}{d\xi}\,, \tag{5.12}$$

equation (5.11) can be rearranged as follows:

$$\frac{d^2Y}{d\xi^2} + \left[\frac{\omega}{1 + A^2 + B^2 f(\xi)}\right]^2 Y = 0\,. \tag{5.13}$$

For the stented region, the mean non-dimensional speed C in the unit cell can be evaluated as

$$C = \int_0^1 \frac{c(\xi)}{c_0} d\xi \; = \int_0^1 \left(1 + A^2 + B^2 f(\xi)\right) d\xi \; = 1 + A^2 + \frac{\Gamma\left(\frac{1}{2} + s\right)}{\sqrt{\pi}\Gamma\left(1 + s\right)} B^2\,, \tag{5.14}$$

for both choices $f(\xi) = \sin^{2s}(\pi\xi)$ or $f(\xi) = \cos^{2s}(\pi\xi)$.

5.2 Dispersion curves and stop-bands

In this section, the dispersion properties of the Bloch-Floquet waves propagating along the walls of the stented blood vessel are presented. Equation (5.11) is solved numerically using the Galerkin method with Finite Element discretisation (see Chapter 2, Section 2.5 for more details on the background of this technique) together with the following Bloch-Floquet conditions applied at the ends of the unit cell $\xi = 0$ and $\xi = 1$:

$$y(1) = y(0)e^{iK}\,, \tag{5.15a}$$

$$\left.\frac{d^j y}{d\xi^j}\right|_{\xi=1} = \left.\frac{d^j y}{d\xi^j}\right|_{\xi=0} e^{iK}\,, \tag{5.15b}$$

where K is the one-dimensional Bloch-Floquet parameter, and only $j = 1$ is required in the derivations below.

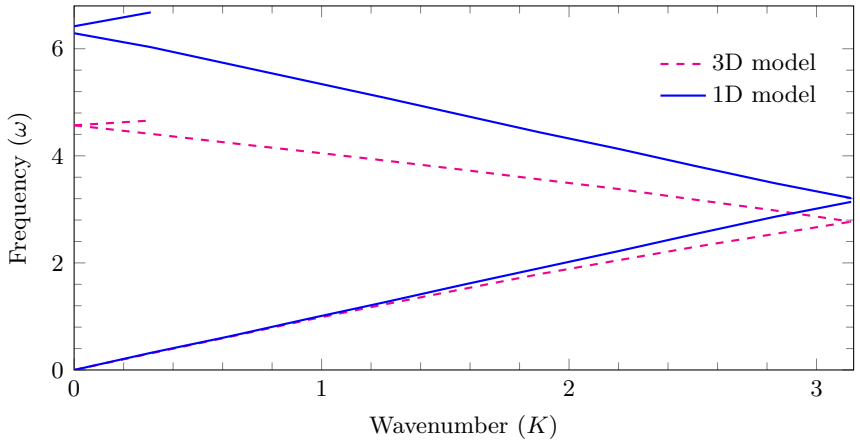

Figure 5.2: Dispersion curves for the unit cell without stent. The dashed line represents the dispersion curves obtained using the 3D model of Chapter 3 and [36], while the solid line represents the results of the 1D model presented in this chapter.

5.2.1 Effective wave speed

The dispersion curves are plotted in the first Brillouin zone, specifically in the interval $[0, \pi]$, in Figure 5.2. A comparison of the dispersion curves for an artery without stent ($C = 1$) corresponding to the one-dimensional model presented here and in [37], and the three-dimensional model of Chapter 3 and [36], is provided by Figure 5.2. Note the difference in frequencies between the one-dimensional and three-dimensional models that arises due to the lower dimensional assumptions. The actual frequency v_d (in Hz) in the three-dimensional model is related to the non-dimensional frequency ω according to

$$v_d = \frac{\omega c_0}{2\pi L}\,. \tag{5.16}$$

The reference pulse wave speed c_0 is obtained from the dispersion diagram of the three-dimensional model of Chapter 3 for an unstented artery. Specifically c_0 is the group velocity $c_0 = \omega/K$ calculated near $K = 0$.

As shown in Figure 5.2, the one-dimensional model provides an upper bound (see the region in the neighbourhoods of $K = \pi$ or $K = 0$) for the stop-band frequencies. This applies both to the first and second stop-bands. It is also noted that the one-dimensional model correctly reflects important features, including, for example, the growth in the magnitude of the group velocity along the acoustic band. The mean value of the normalised wave speed in the stented artery is evaluated using equation (5.14).

The parameters A^2, B^2, and s are calibrated such that the group velocity near the origin for the one-dimensional model matches the group velocity of the axisymmetric mode in the three-dimensional model of Chapter 3. For the types of stents considered in Chapter 3, the mean non-dimensional speed in each unit cell is $C \simeq 1.12$. In Figure 5.3a, the surface (5.14) is plotted for this value of C for $A^2 \in [0, 0.13]\,, B^2 \in [0, 1.3]\,, s \in [0, 30]$. Figures 5.3b-5.3d describe the behaviour of the three parameters used in the definition of the mean non-dimensional velocity. For fixed A^2 it can be noted that B^2 increases

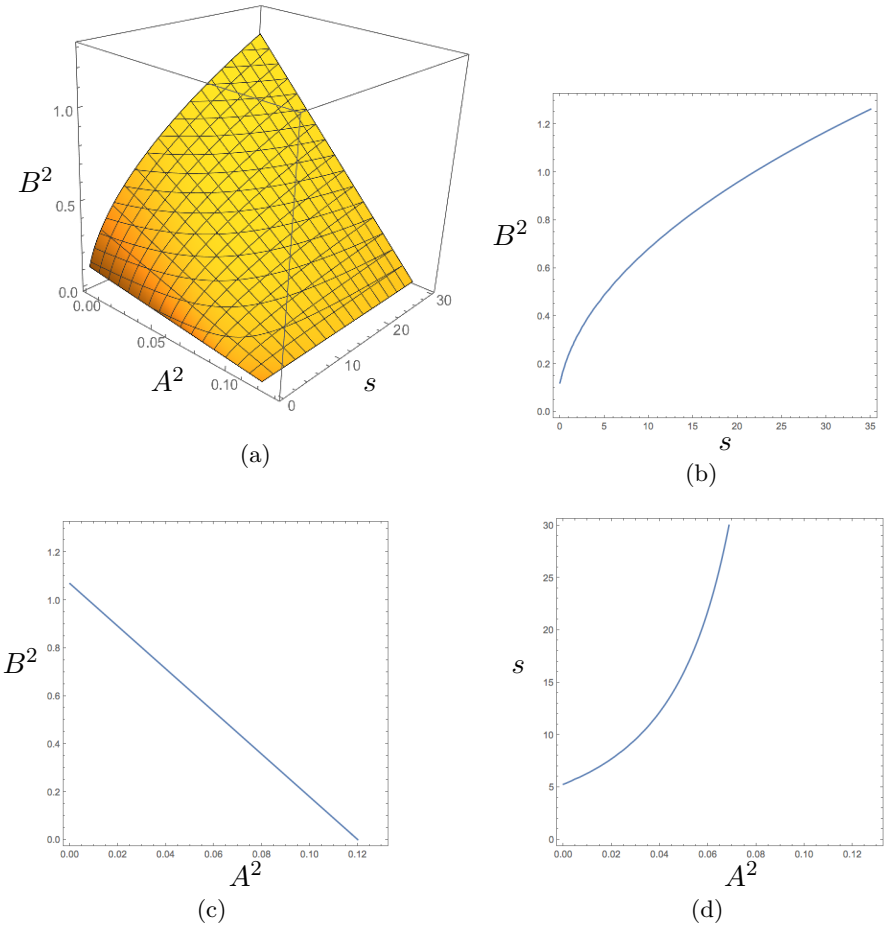

Figure 5.3: The effect of the parameters A^2, B^2, and s in (5.14) on the mean non-dimensional speed for a stented unit cell. Here $C = 1.12$. Part (a): implicit solution of equation (5.14) for $A^2 \in [0, 0.13]$, $B^2 \in [0, 1.3]$, $s \in [0, 30]$. Part (b): contour plot for $A^2 = 0$. Part (c): contour plot for $s = 25$. Part (d): contour plot for $B^2 = 0.5$.

with s (see Figure 5.3b). For fixed s, if B^2 increases then A^2 decreases (see Figure 5.3c). Finally, for fixed B^2, s increases with A^2 (see Figure 5.3d).

5.2.2 Stop-bands for waves in structured arteries

Here, the case of $A^2 = 0$, which corresponds to an artery without a plaque, is considered. The choices $s = 1$, $s = 2$, $s = 5$, $s = 10$, $s = 15$, $s = 20$ and $s = 30$ are substituted into equation (5.11) to obtain the position and width of the stop-bands for the dispersion curves at $K = 0$ and $K = \pi$ for the stented case. The results are illustrated in Figure 5.4a. The width of the stop-band is considered to be an important parameter when comparing the one-dimensional approximation with the full three-dimensional model of Chapter 3 and [36].

A better approximation is to be expected for the first stop-band at $K = \pi$, since it is in the low frequency regime. It is noted that, in general, higher values of s ($s > 15$) produce better results, with the best result in Figure 5.4a being for $s = 20, B^2 = 0.97$ (shown in Figure 5.4b). There is extremely good correspondence at $K = \pi$ between

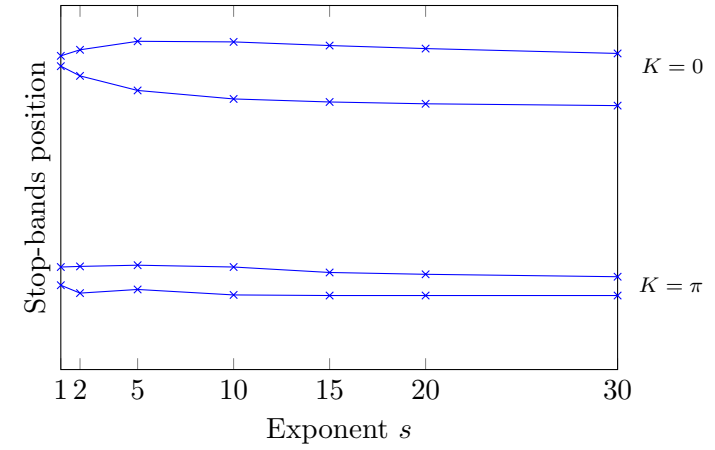

(a)

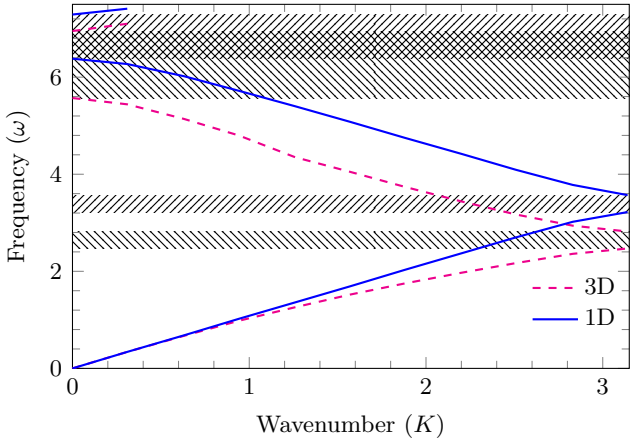

(b)

Figure 5.4: The first two stop-bands for the one-dimensional model discussed in Section 5.1 and the three-dimensional simulation of the pulsating wave. Part (a) shows the boundaries of the first two stop-bands (for $K = 0$ and $K = \pi$) as functions of s for the one-dimensional model. Here $A^2 = 0$, and $f(\xi) = \sin^{2s}(\pi\xi)$. B^2 varies with s according to (5.11) (see also Figure 5.3b). Part (b) illustrates the dispersion curves for $A^2 = 0$, $B^2 = 0.97$, $f(\xi) = \sin^{40}(\pi\xi)$. The dashed line represents the three-dimensional model of Chapter 3, while the solid line corresponds to the one-dimensional model.

the stop-band widths, with 0.36 for both the one-dimensional (solid line) and three-dimensional (dashed line) models. For the higher value of $s = 30$, there again appears to be a good correspondence between the stop-bands, with the one-dimensional model predicting a somewhat smaller band-width compared to the three-dimensional model.

Interestingly, the extreme case of small parameter values ($s = 1, A^2 = 0, B^2 = 0.24$) in Figure 5.4a results in a narrower stop-band for the one-dimensional model. The overlapping of the second stop-bands (illustrated by the cross-hatched areas in Figure 5.4b) does not occur for $s = 1$. The new model proposed here allows for higher values of s to be incorporated into the analysis showing a significant improvement in agreement for sufficiently large s.

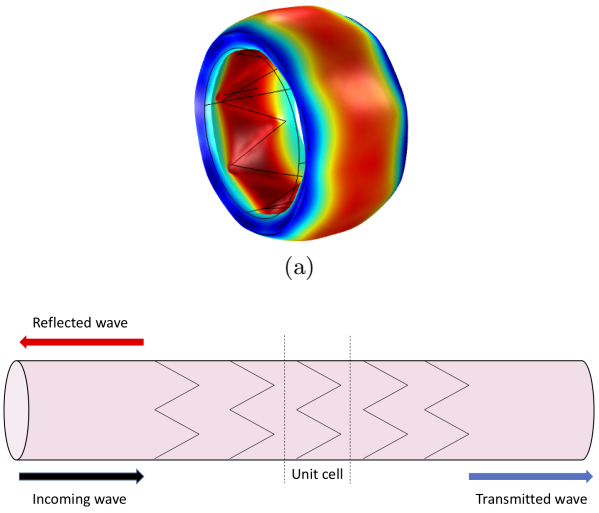

(a)

(b)

Figure 5.5: Part (a) illustrates the axisymmetric mode obtained using the three-dimensional model of Chapter 3 and [36]. Part (b) shows reflected and transmitted waves in a stented artery.

5.3 Transmission problem

In this section the transmission problem for a stented blood vessel is considered. The volumetric flow rates in the reflection region, stented region, and transmission region are assumed to be of the form

$$Q_R = q_R(\xi)e^{-i\omega\eta}\,, \quad -\infty < \xi < 0\,, \tag{5.17a}$$

$$Q = y(\xi)e^{-i\omega\eta}\,, \quad 0 < \xi < n\,, \tag{5.17b}$$

$$Q_T = q_T(\xi)e^{-i\omega\eta}\,, \quad n < \xi < \infty\,, \tag{5.17c}$$

respectively, where ω is the angular frequency.

A diagram for the reflection-transmission problem is shown in Figure 5.5b. The flow rate in the reflection region consists of the original incoming wave, with unit amplitude, and the reflected wave which has amplitude R,

$$q_R(\xi) = e^{i\omega\xi} + Re^{-i\omega\xi}\,. \tag{5.18}$$

In the transmission region, the outgoing wave is of amplitude T,

$$q_T(\xi) = Te^{i\omega\xi}\,. \tag{5.19}$$

The four interface conditions are

$$q_R(0) = y(0) \quad \text{and} \quad \left.\frac{dq_R}{d\xi}\right|_{\xi=0} = Y(0)\,, \tag{5.20a}$$

$$q_T(n) = y(n) \quad \text{and} \quad \left.\frac{dq_T}{d\xi}\right|_{\xi=n} = Y(n)\,, \tag{5.20b}$$

where $y(\xi)$ and $Y(\xi)$ are defined in (5.11) and (5.12). Equation (5.11) is solved numerically using the Galerkin method with Finite Element discretisation (see Section 2.5) together with the interface conditions (5.20).

5.3.1 Reduction to the Mathieu equation for the case $s = 1$

When s is chosen to be 1, the mean non-dimensional speed in each cell is given by

$$C = 1 + A^2 + \frac{B^2}{2}\,, \tag{5.21}$$

for both functions $f(\xi) = \sin^2(\pi\xi)$ and $f(\xi) = \cos^2(\pi\xi)$. Furthermore, using the formulae $2\sin^2(\xi) = 1 - \cos(2\xi)$ and $2\cos^2(\xi) = 1 + \cos(2\xi)$, and calling

$$\epsilon = \frac{B^2}{2C} = \frac{B^2}{2 + 2A^2 + B^2} < 1\,, \tag{5.22}$$

leads to the equation

$$\frac{d^2Y}{d\xi^2} + \frac{\omega^2}{C^2\left(1 \mp \epsilon\cos\left(2\pi\xi\right)\right)^2}Y = 0\,, \tag{5.23}$$

where the minus sign corresponds to the choice $f(\xi) = \sin^2(\pi\xi)$ and the plus sign to $f(\xi) = \cos^2(\pi\xi)$. Assuming now $\epsilon \ll 1$ and noticing that $|\cos(2\pi\xi)| \leq 1$, the expansion

$$\left(1 \mp \epsilon\cos(2\pi\xi)\right)^{-2} = 1 \pm 2\epsilon\cos(2\pi\xi) + O(\epsilon^2) \approx 1 \pm 2\epsilon\cos(2\pi\xi)\,, \tag{5.24}$$

can be used. Substituting (5.24) into (5.23) and using the change of variable $\pi\xi = z$ we obtain the following standard Mathieu equation

$$\frac{d^2Y}{dz^2} + \left[a \pm 2q\cos(2z)\right]Y = 0\,, \tag{5.25}$$

with

$$a = \left(\frac{\omega}{\pi C}\right)^2\,, \tag{5.26a}$$

$$q = \epsilon\left(\frac{\omega}{\pi C}\right)^2 = \epsilon a\,. \tag{5.26b}$$

The general solution for the Mathieu equation (see Chapter 2, Section 2.6 and also the book by McLachlan [77]) is given by

$$Y(\xi) = C_1 M_S\left(a, -q, \pi\xi\right) + C_2 M_C\left(a, -q, \pi\xi\right)\,, \tag{5.27}$$

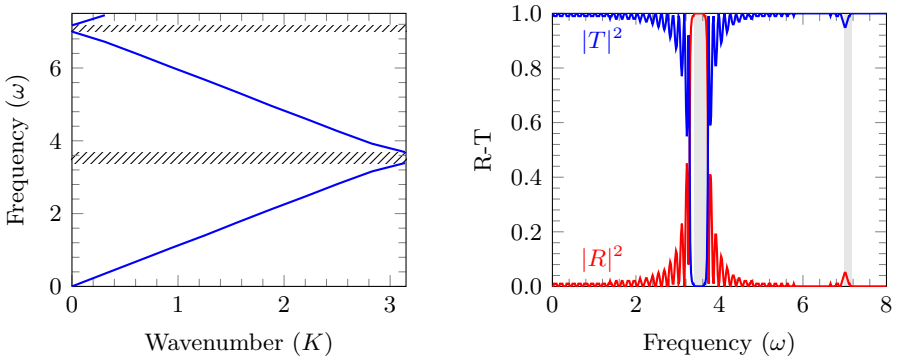

(a) (b)

Figure 5.6: Part (a) shows the dispersion curves for the Mathieu equation. Part (b) illustrates the corresponding transmission problem for the Mathieu equation with $n = 24$ cells. The parameters defining the velocity are chosen to be $A^2 = 0\,, B^2 = 0.24\,, f(\xi) = \sin^2(\pi\xi)$, so that $C = 1.12$.

for $f(\xi) = \sin^2(\pi\xi)$, and

$$Y(\xi) = C_1 M_S\left(a, q, \pi\xi\right) + C_2 M_C\left(a, q, \pi\xi\right)\,, \tag{5.28}$$

for $f(\xi) = \cos^2(\pi\xi)$, where M_S and M_C are the Mathieu functions, linearly independent solutions of (5.25) with the property that $M_S(a, q, 0) = 0$ and $M_C^{'}(a, q, 0) = 0$. In what follows, the case $f(\xi) = \sin^2(\pi\xi)$, which corresponds to a periodic cell that is more compliant at its edges, is considered. Applying the Bloch-Floquet conditions (5.15) to the Mathieu equation the following dispersion relation is obtained:

$$\begin{aligned}&\left[M_C\left(a, -q, \pi\right) M_S^{'}\left(a, -q, 0\right) + M_C\left(a, -q, 0\right) M_S^{'}\left(a, -q, \pi\right)\right] e^{iK}\\ &+ M_S\left(a, -q, \pi\right) M_C^{'}\left(a, -q, \pi\right) = M_S^{'}\left(a, -q, \pi\right) M_C\left(a, -q, \pi\right)\\ &+ M_C\left(a, -q, 0\right) M_S^{'}\left(a, -q, 0\right) e^{2iK}\,.\end{aligned} \tag{5.29}$$

The choice of parameters A^2 and B^2 is determined by the effective wave speed, as explained in Section 5.2.1.

As expected, the reflection at frequencies corresponding to the stop band is high, as illustrated in Figure 5.6b, which shows the reflection and transmission coefficients $|R|^2$ and $|T|^2$ versus the frequency of the incident wave. We also note a relatively high reflection within the first pass-band region, especially in the neighbourhood of the stop-band boundary. Such reflection can be altered by changing the rate of localisation within the structured stent. Note that in Figure 5.6b, the second stop-band is not visible as it requires more cells to be considered.

5.3.2 Transmission for the higher-order sparse stent structure

At higher values of the exponent s characterising the sparse stent structure, the transmission diagrams are shown in Figures 5.7b, 5.7d. The choice of parameters is the same as

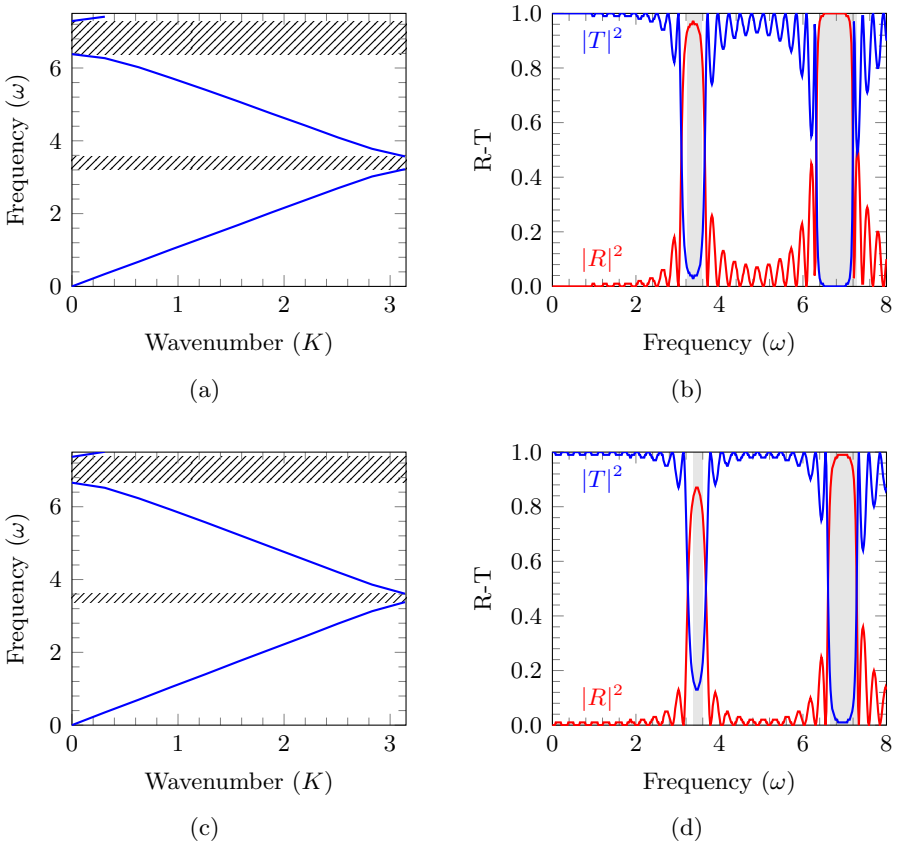

Figure 5.7: Dispersion curves (a), (c) and corresponding reflection-transmission diagrams (b), (d) for a stented artery, with $f(\xi) = \sin^{40}(\pi\xi)$ and A^2, B^2 defined from (5.14) for $C = 1.12$. Part (a): dispersion curves for $A^2 = 0\,, B^2 = 0.97$. Part (c): dispersion curves for $A^2 = 0.05\,, B^2 = 0.58$. Part (b): transmission-reflection diagram for $A^2 = 0\,, B^2 = 0.97\,, n = 12$. Part (d): transmission-reflection diagram for $A^2 = 0.05\,, B^2 = 0.58\,, n = 12$.

in the dispersion diagrams of Figures 5.7a, 5.7c. In Figure 5.7b the shaded areas match the hatched areas in Figure 5.7a, as expected. Accordingly, the stop-bands correspond to the high reflection of the incident wave.

The reflection at frequencies corresponding to the first pass-band appears to be smaller for highly localised structured stents compared with the case of $s = 1$. Also, the secondary stop-band in diagrams 5.7a and 5.7c corresponds to a higher reflection, if the frequency of the incident wave includes higher-order harmonics, this is likely to be the case in the transition regimes or abnormalities leading to an irregular heart beat.

Transmission diagrams for the case of $s = 20$ are shown in Figures 5.7b, 5.7d for the value of $C = 1.12$; they correspond to different values of A^2 and B^2 evaluated using (5.14), which represent an alteration in the stiffness of the artery and of the stent. This is shown to have an effect on reflection in the second pass-band, while the reflection in the first pass-band remains low.

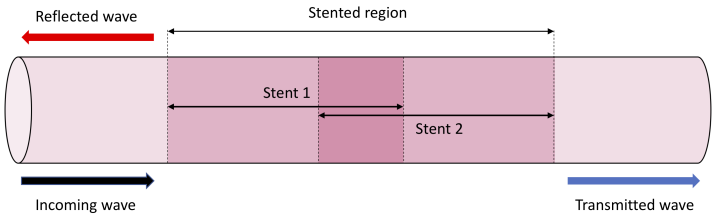

Figure 5.8: Scheme representing an artery with two overlapping stents.

5.4 Dispersion curves and transmission problem for overlapping stents

Stent overlapping is a common procedure in vascular surgery, especially in the femoral artery where two or three overlapping stents may be needed to cover the whole area affected by stenosis. Some references include the work by Raber *et al.* [100], Leybovitch *et al.* [70], Lee *et al.* [68], Xu *et al.* [123] and Rikhtegar *et al.* [102]. However, this procedure is often associated with increased risk in the clinical outcome.

In this section, the Bloch-Floquet analysis and the trasmission problem for a stented artery with overlapping stents will be discussed. The problem is represented in Figure 5.8. The non-dimensional velocity in the artery is assumed to be

$$\frac{c(\xi)}{c_0} = \begin{cases} 1, & \xi \in (-\infty, 0) \\ 1 + A^2 + B^2 \sin^{2s}(\pi\xi) \text{ or } 1 + A^2 + B^2 \cos^{2s}(\pi\xi), & \xi \in (0, n) \\ \sqrt{2}(1 + A^2 + B^2 \sin^{2s}(\pi\xi)) \text{ or } \sqrt{2}(1 + A^2 + B^2 \cos^{2s}(\pi\xi)), & \xi \in (n, m) \\ 1 + A^2 + B^2 \sin^{2s}(\pi\xi) \text{ or } 1 + A^2 + B^2 \cos^{2s}(\pi\xi), & \xi \in (m, d) \\ 1, & \xi \in (d, +\infty), \end{cases} \tag{5.30}$$

where n is the number of stent coils constituting the first stent excluding the overlapping region, m is the number of stent coils in the overlapping region, and d is the number of stent coils constituting the second stent excluding the overlapping region.

Assuming that the solution of equation (5.9) is of the form $Q_i = y_i(\xi)e^{-i\omega\eta}$, where ω is the angular frequency and $i = 1, 2, 3$, the functions $y_i(\xi)$ then satisfies the equation

$$\frac{d}{d\xi}\left(\left[\lambda(\xi)(1 + A^2 + B^2 f(\xi))\right]^2 \frac{dy_i}{d\xi}\right) + \omega^2 y_i = 0\,, \tag{5.31}$$

$\lambda(\xi)$ is the piecewise constant function, which is equal to 1 in the stented region without overlapping, and it is equal to $\sqrt{2}$ in the overlapping region. We also introduce the

following notation

$$Y_1 = \left[1 + A^2 + B^2 f(\xi)\right]^2 \frac{dy_1}{d\xi}\,, \tag{5.32a}$$

$$Y_2 = \sqrt{2}\left[1 + A^2 + B^2 f(\xi)\right]^2 \frac{dy_2}{d\xi}\,, \tag{5.32b}$$

$$Y_3 = \left[1 + A^2 + B^2 f(\xi)\right]^2 \frac{dy_3}{d\xi}\,. \tag{5.32c}$$

5.4.1 Stop-bands and reflected energy

The Bloch-Floquet analysis and the transmission problem for a stented artery with an overlapping region is discussed in this section. The total length of the unit periodic cell for the stented artery with an overlapping region is given by $N = n + m + d$. Equation (5.31) is solved numerically using the Galerkin method together with the following Bloch-Floquet conditions applied at the end parts of the unit cell $\xi = 0$ and $\xi = N$:

$$y(N) = y(0)e^{iKN}\,, \tag{5.33a}$$

$$y_\xi(N) = y_\xi(0)e^{iKN}\,, \tag{5.33b}$$

where K, as before, is the one-dimensional Bloch-Floquet parameter. Continuity of the solution between the different regions of the stented artery is also imposed.

For the transmission problem, the volumetric flow rate in the reflected region, stented regions, overlapping region and transmission region are of the form

$$Q_R = q_R(\xi)e^{-i\omega\eta}\,, \quad -\infty < \xi < 0\,, \tag{5.34a}$$

$$Q_1 = y_1(\xi)e^{-i\omega\eta}\,, \quad 0 < \xi < n\,, \tag{5.34b}$$

$$Q_2 = y_2(\xi)e^{-i\omega\eta}\,, \quad n < \xi < n + m\,, \tag{5.34c}$$

$$Q_3 = y_3(\xi)e^{-i\omega\eta}\,, \quad n + m < \xi < n + m + d\,, \tag{5.34d}$$

$$Q_T = q_T(\xi)e^{-i\omega\eta}\,, \quad n + m + d < \xi < \infty\,. \tag{5.34e}$$

The flow rate q_R in the reflected region and q_T in the transmitted region are defined in the same way as the case of a stented artery without overlapping (see (5.18), (5.19)). Recalling (5.31), in the stented region the following equations are valid

$$y_i = -\frac{1}{\omega^2}\frac{dY_i}{d\xi}\,, \quad i = 1, 2, 3\,. \tag{5.35}$$

Consequently, the eight interface conditions are

$$q_R(0) = y_1(0) \quad \text{and} \quad \left.\frac{dq_R}{d\xi}\right|_{\xi=0} = Y_1(0)\,, \tag{5.36a}$$

$$y_2(n) = y_1(n) \quad \text{and} \quad \left.\frac{dy_2}{d\xi}\right|_{\xi=n} = Y_1(n)\,, \tag{5.36b}$$

$$y_2(n+m) = y_3(n+m) \quad \text{and} \quad \left.\frac{dy_2}{d\xi}\right|_{\xi=n+m} = Y_3(n+m)\,, \tag{5.36c}$$

$$q_T(n+m+d) = y_3(n+m+d) \quad \text{and} \quad \left.\frac{dq_T}{d\xi}\right|_{\xi=n+m+d} = Y_3(n+m+d)\,. \tag{5.36d}$$

The dispersion curves resulting from the Bloch-Floquet analysis are plotted in Figure 5.9a. The analysis is representative for the case of two stents composed of 8 coils each, and an overlapping area composed of 4 coils. Observing the dispersion curves in Figure 5.9a it is possible to note that the range of frequencies in the low frequency regime corresponding to pass-band in Figure 5.4b (that is where the wave propagates), now contains a number of stop-bands (where the wave does not propagate). Figures 5.9b- 5.9d represent the reflection-transmission diagrams for a different number of periodic cells.

It can be noted that as more periodic cells are considered (that is stents with multiple overlapping regions), the reflection in the range of frequencies corresponding to the stop-bands becomes higher. Figure 5.10 shows the comparison between a long stent composed of 24 periodic cells and two examples of overlapping stents. The first shown in 5.10b is composed of two stents with 16 periodic cells each with an overlapping region composed of 8 periodic cells. The second shown in 5.10c is composed of two stents with 13 periodic cells each with an overlapping region of 2 periodic cells. It can be observed that in the low frequency regime, the energy reflected is higher for both cases when the stents overlap, which may increase the risk of restenosis if overlapping stents are used.

The connection between dispersion properties and transmission-reflection of waves for a range of stenting parameter values was analysed using a simplified one-dimensional model. An appealing feature of this approach (for both biomechanical researchers and medical practitioners) is that it enables one to quickly obtain approximate values for stenting parameters that may result in the formation of high wave reflection and transmission regimes. Once the ball park ranges have been identified, more detailed investigations may be carried out using more precise and time-consuming simulation tools.

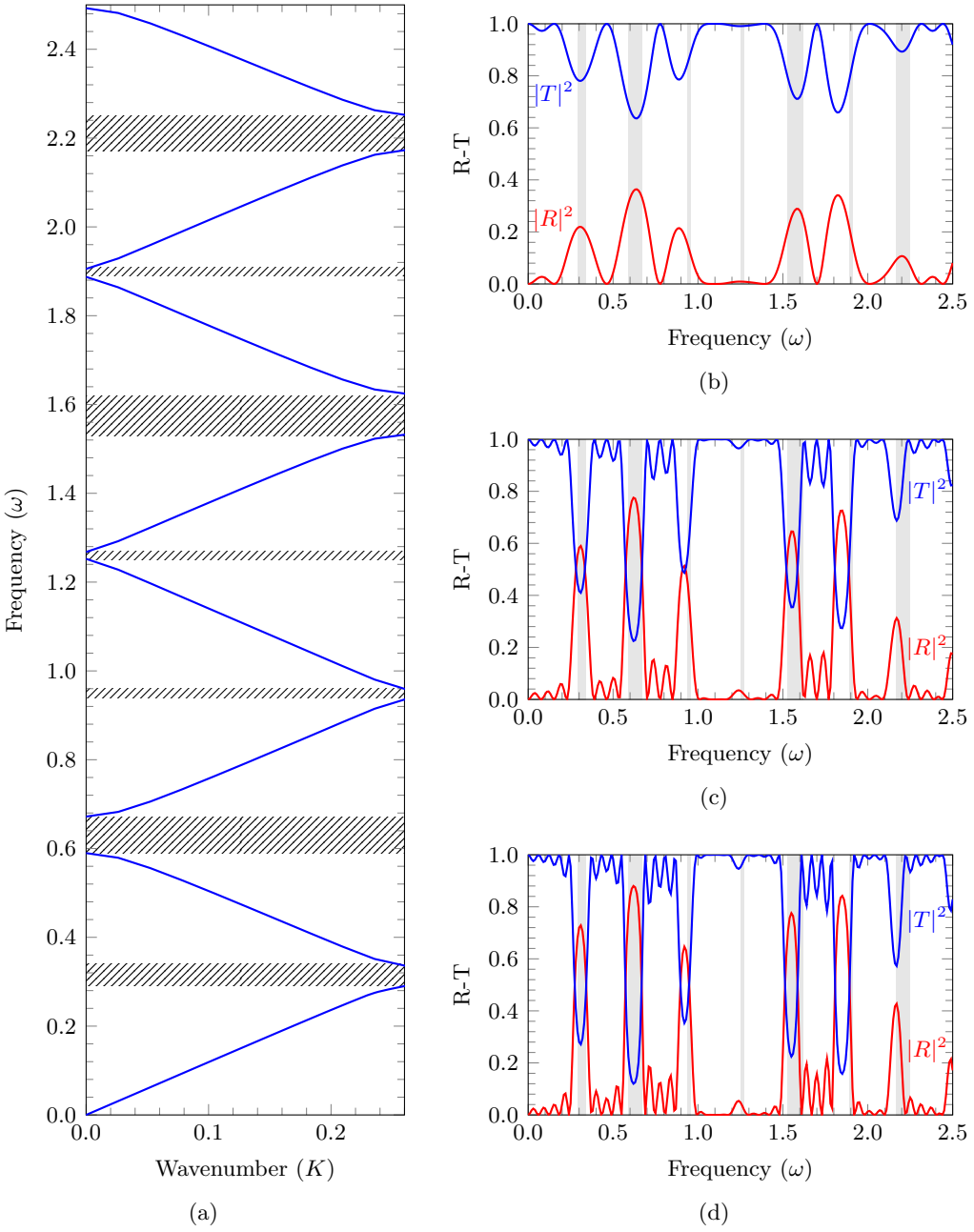

Figure 5.9: Dispersion curves (a) and reflection-transmission diagrams (b), (c), (d) for the problem of overlapping stents. The parameters for the mean non-dimensional speed are chosen to be $A^2 = 0$, $B^2 = 0.97$, $f(\xi) = \sin^{40}(\pi\xi)$, $m = n = d = 4$. Part (a): dispersion curves. The dashed area represents the stop-band regions. Part (b): reflection-transmission diagram with 2 periodic cells. Part (c): reflection-transmission diagram with 4 periodic cells. Part (d): reflection-transmission diagram with 5 periodic cells. In (b)-(d) the shaded areas correspond to the stop-band regions.

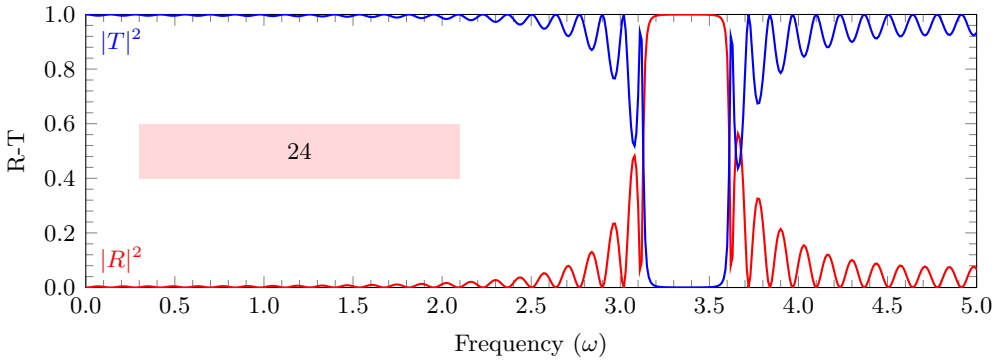

(a)

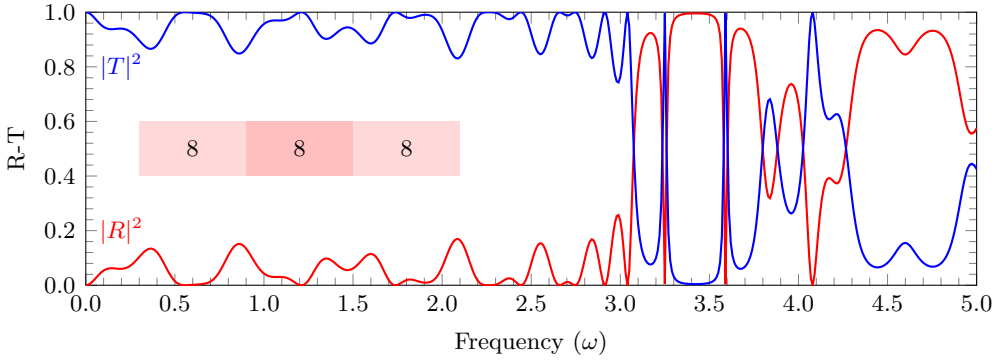

(b)

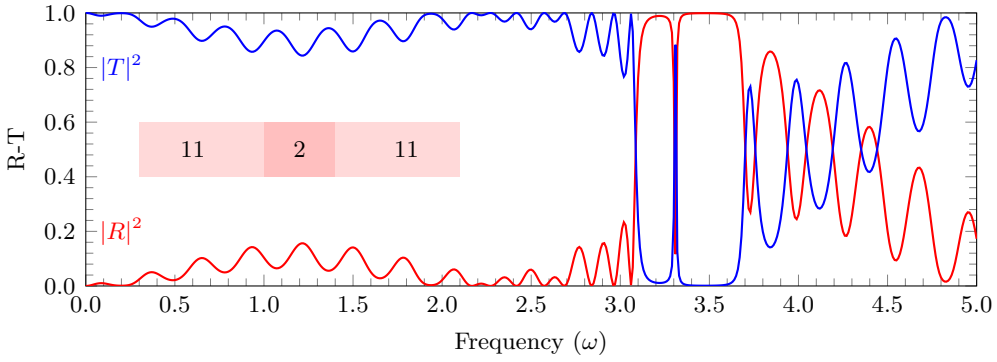

(c)

Figure 5.10: Reflection-transmission diagrams for (a) long stent composed of 24 periodic cells with no overlapping region ($n = 24\,, m = d = 0$), (b) two stents composed of 16 periodic cells each with an overlapping region of 8 cells ($n = m = d = 8$) and (c) two stents composed of 13 periodic cells each with an overlapping region of 2 cells ($n = d = 11, m = 2$). The parameters for the mean non-dimensional speed used in the calculations are $A^2 = 0$, $B^2 = 0.97$, $f(\xi) = \sin^{40}(\pi\xi)$.

Chapter 6

Conclusions and future work

This thesis has presented novel modelling approaches to investigate the dynamics of fluid-structure interaction associated with a stented artery. The main mathematical techniques used are:

- Bloch-Floquet analysis for periodic systems (for both three-dimensional and one-dimensional models);
- Transmission-reflection methods in the frequency domain;
- Transient modelling for three-dimensional case in the time domain.

The main outcome of the research is a capability to describe frequency regimes and deformations of blood vessels, which may have a detrimental effect on transmission of the blood flow. Axisymmetric and non-axisymmetric deformations have been identified, including those that may be associated with so-called stop-bands. Trapped modes are given attention for clusters of stents, separated by a finite distance, and asymptotic approximations have been derived for predictive analysis of the associated waveforms. The work has led to three publications [36, 37, 120], which are listed at the beginning of the thesis, as well as several conference presentations.

Several of this work's outputs have potential benefits for medical practitioners. In particular,

- an approximate one-dimensional model that is capable of rapid identification of frequency ranges for which strong pulse wave reflections may occur;
- overlapping stents appear to carry more risk (stop-bands arise at lower frequencies) than a single stent of the same length;
- links between coils (made of the same material rather than a soft fabric such as nylon) push the stop-band frequencies to lower regimes, so it appears to be preferable to use non-metallic connections;
- standing wave modes are observed for multi-stented regions, which may lead to localisation of energy;

- location, geometry and density of atherosclerotic plaque affect dispersion properties, altering stop-band frequency regimes.

The Bloch–Floquet wave theory is shown to be effective as a framework for time-harmonic modelling of waves in stented blood vessels. The approach proposed here enables one to evaluate, qualitatively and quantitatively, wave reflections from stents. In particular, it was demonstrated that waves of certain frequencies can be blocked by stents placed in arteries. The geometry proved to be an important factor that influences the location of the first stop-band, which is critical for medical practitioners in cardiovascular applications. Specific geometrical factors, such as cross-linking of coils within the stent, leads to the formation of additional stop-bands and may increase the stop-band width. A very recent paper by Sorokin *et al.* [110] implemented Floquet analysis to investigate the case of a periodic fluid-filled shell subject to heavy fluid loading and pre-tension, with attention focused on the axisymmetric wave motion.

The additional transient analysis in the time domain in Chapter 3, involving two-way fluid–structure interaction, was implemented for a stented blood vessel. A comparison with the unstented blood vessel was analysed in terms of blood flow. The improved understanding of the effects of stent design on fluid–solid interaction provides researchers and clinicians with additional insights for the dynamic system. This new modelling capability begins to explain why certain arteries respond well to stenting, while others have less successful outcomes.

One of the major factors leading to stent deployment is the build up of atherosclerotic plaque, which is a complicated biological material consisting of a host of infiltrates such as lipids, calcium, collagen, cellular waste, fibrin and cholesterol [113]. The inclusion of plaque in the modelling here in Chapter 4 shows that it has a major effect on the coupled system's dispersion properties, both before and after the stent deployment. A variety of realistic geometries were analysed, and their dispersion properties illustrated with mode pictures and dispersion diagrams.

In this study, the plaque was assumed to be a linearly elastic isotropic homogeneous material. However, medical studies have shown that the elastic stiffness is highly variable. Several models in the literature incorporate arterial and plaque material properties, including those of Gleason *et al.* [44, 45] and Holfzapfel and co-workers [50, 52, 53]. Compressive stiffness depends on the type of plaque, with non-fibrous (atheromatous) plaques being the least stiff [113], followed by fibrous and then calcified plaques being the stiffest as reported by Topoleski *et al.* [114] and Maher *et al.* [75]. The case of calcified plaque was modelled in Chapter 4 here, but future work may incorporate other classes such as the fibrous and non-fibrous types and more realistic, non-linear assumptions for the plaque.

The simplicity of the one-dimensional model in Chapter 5 and [37] makes it appealing to both researchers and medical practitioners, since it enables one to obtain ballpark ranges for values of stenting parameters that may lead to formation of high wave reflection in the transitional regimes. Practical consequences are secondary vascular blockages

and formation of standing waves in the blood vessels. In particular, the connection between dispersion properties and transmission–reflection of waves for different values of the stenting parameters has been analysed in detail here, and provided valuable material for assessment of the performance of stents in different transitional regimes. The special case of overlapping stents was analysed, where elastic stiffness increases in the regions of overlap; it was demonstrated that such configurations may lead to additional wave reflection and formation of stop-bands in the dispersion diagram.

Areas where the work of this thesis may be built upon on in the future include the analysis of more stent designs:

- vary the number of links and density of coils in the unit cell;
- variation of the size of stent;
- different material parameters for the stents;
- different types of connection between the crowns (e.g. zigzags in place of straight beams).

It is also important to broaden the range of plaques investigated, taking into account the other major classes such as cellular and hypocellular, as well as the stiffer, calcified types considered here. It is clear that the nature of the plaque affects the dispersion properties of the coupled stented artery system. The transmission-reflection methods utilised for the arteries with no plaque, can also be implemented for the atherosclerotic models. Other extensions may feature the inclusion of overlapping stents and radial displacements within the approximate one-dimensional model, for which some of the analysis in [110] may be useful.

Bibliography

[1] M. Abramowitz and I. A. Stegun. *Handbook of Mathematical Functions*. NBS, 10 edition, 1972. ISBN 505-506-509-5.

[2] J. Alastruey, A. W. Khir, K. S. Matthys, P. Segers, S. J. Sherwin, P. R. Verdonck, K. H. Parker, and J. Peiró. Pulse wave propagation in a model human arterial network: assessment of 1-d visco-elastic simulations against in vitro measurements. *Journal of Biomechanics*, 44(12):2250–2258, 2011. doi: 10.1016/j.jbiomech.2011.05.041.

[3] J. Alastruey, T. Passerini, L. Formaggia, and J. Peiró. Physical determining factors of the arterial pulse waveform: theoretical analysis and calculation using the 1-d formulation. *Journal of Engineering Mathematics*, 77(1):19–37, 2012. doi: 10.1007/s10665-012-9555-z.

[4] G. B. Arfken, H. J. Weber, and F. E. Harris. *Mathematical Methods for Physicists, Seventh Edition: A Comprehensive Guide*. Academic Press, 7 edition, 2012. ISBN 0123846544,9780123846549.

[5] L. P. Argani, F. Torella, R. K. Fisher, R. G. McWilliams, M. L. Wall, and A. B. Movchan. Deformation and dynamic response of abdominal aortic aneurysm sealing. *Scientific Reports*, 7(1):17712, 2017. doi: https://doi.org/10.1038/s41598-017-17759-3.

[6] F. Auricchio, A. Constantinescu, M. Conti, and G. Scalet. A computational approach for the lifetime prediction of cardiovascular balloon-expandable stents. *International Journal of Fatigue*, 75:69–79, 2015. doi: 10.1016/j.ijfatigue.2015.02.002.

[7] M. Azaouzi, A. Makradi, and S. Belouettar. Deployment of a self-expanding stent inside an artery: A finite element analysis. *Materials & Design*, 41:410–420, 2012. doi: 10.1016/j.matdes.2012.05.019.

[8] M. Back, G. Kopchok, M. Mueller, D. Cavaye, C. Donayre, R. A. White, et al. Changes in arterial wall compliance after endovascular stenting. *Journal of vascular surgery*, 19(5):905–911, 1994. doi: 10.1016/S0741-5214(94)70017-6.

[9] K. Baik, J. Jiang, and T. G. Leighton. Acoustic attenuation, phase and group velocities in liquid-filled pipes I: Theory, experiment, and examples of water and

mercury. *The Journal of the Acoustical Society of America*, 128(5):2610–2624, 2010. doi: doi.org/10.1121/1.3495943.

[10] K. Baik, J. Jiang, and T. G. Leighton. Acoustic attenuation, phase and group velocities in liquid-filled pipes III: Nonaxisymmetric propagation and circumferential modes in lossless conditions. *The Journal of the Acoustical Society of America*, 133 (3):1225–1236, 2013. doi: 10.1121/1.4773863.

[11] S. R. H. Barrett, M. P. F. Sutcliffe, S. Howarth, Z. Y. Li, and J. H. Gillard. Experimental measurement of the mechanical properties of carotid atherothrombotic plaque fibrous cap. *Journal of Biomechanics*, 42(11):1650–1655, 2009. doi: 10.1016/j.jbiomech.2009.04.025.

[12] L. Brillouin. *Wave Propagation in Periodic Structures*. Dover Publications, Inc., 2 edition, 1953. ISBN 0-444-86199-8.

[13] M. Brun, S. Guenneau, A. B. Movchan, and D. Bigoni. Dynamics of structural interfaces: filtering and focussing effects for elastic waves. *Journal of the Mechanics and Physics of Solids*, 58(9):1212–1224, 2010. doi: 10.1016/j.jmps.2010.06.008.

[14] C. G. Caro, T. J. Pedley, and R. C. Schroter. *The Mechanics of the Circulation*. Cambridge University Press, 2012. ISBN 9781139013406.

[15] G. Carta and M. Brun. Bloch-Floquet waves in flexural systems with continuous and discrete elements. *Mechanics of Materials*, 87:11–26, 2015. doi: 10.1016/j.mechmat.2015.03.004.

[16] G. Carta, M. Brun, and A. B. Movchan. Dynamic response and localization in strongly damaged waveguides. *Proceedings of the Royal Society A: Mathematical, Physical and Engineering Sciences*, 470(2167):20140136, 2014. doi: 10.1098/rspa.2014.0136.

[17] G. Carta, M. Brun, A. B. Movchan, and T. Boiko. Transmission and localisation in ordered and randomly-perturbed structured flexural systems. *International Journal of Engineering Science*, 98:126–152, 2016. doi: 10.1016/j.ijengsci.2015.09.005.

[18] G. Carta, A.B. Movchan, L.P. Argani, and O.S. Bursi. Quasi-periodicity and multi-scale resonators for the reduction of seismic vibrations in fluid-solid systems. *International Journal of Engineering Science*, 109:216–239, 2016. doi: 10.1016/j.ijengsci.2016.09.010.

[19] M. E. Casciaro, M. A. Alfonso, D. Craiem, J. M. Alsac, S. El-Batti, and R. L. Armentano. Predicting the effect on pulse wave reflection of different endovascular repair techniques in abdominal aortic aneurysm using 1d patient-specific models. *Health and Technology*, 6(3):173–179, 2016. doi: 10.1007/s12553-016-0140-8.

[20] J. Chandra and R. Kumar. Axially symmetric vibrations of finite cylindrical shells of various wall thicknesses - ii. *Acustica*, 38(1):24–29, 1977.

[21] J. Chandra and R. Kumar. Flexural vibrations of finite cylindrical shells of various wall thicknesses - i. *Acustica*, 38(4):258–263, 1977.

[22] J. Chandra and R. Kumar. Flexural vibrations of finite cylindrical shells of various wall thicknesses - ii. *Acustica*, 46(3):283–288, 1980.

[23] K. B. Chandran, A. P. Yoganathan, and S. E. Rittgers. *Biofluid Mechanics : The Human Circulation*. CRC/Taylor & Francis, 1 edition, 2007. ISBN 0-8493-7328-X,978-0-8493-7328-2.

[24] J. Charonko, S. Karri, J. Schmieg, S. Prabhu, and P. Vlachos. In vitro, time-resolved piv comparison of the effect of stent design on wall shear stress. *Annals of biomedical engineering*, 37(7):1310–1321, 2009. doi: 10.1007/s10439-009-9697-y.

[25] J. Charonko, S. Karri, J. Schmieg, S. Prabhu, and P. Vlachos. In vitro comparison of the effect of stent configuration on wall shear stress using time-resolved particle image velocimetry. *Annals of biomedical engineering*, 38(3):889–902, 2010. doi: 10.1007/s10439-010-9915-7.

[26] J. J. Charonko, S. A. Ragab, and P. P. Vlachos. A scaling parameter for predicting pressure wave reflection in stented arteries. *Journal of Medical Devices*, 3(1), 2009. doi: 10.1115/1.3089140.

[27] C. P. Cheng, N. M. Wilson, R. L. Hallett, R. J. Herfkens, and C. A. Taylor. In vivo mr angiographic quantification of axial and twisting deformations of the superficial femoral artery resulting from maximum hip and knee flexion. *Journal of vascular and interventional radiology*, 17(6):979–987, 2006. doi: 10.1097/01.RVI.0000220367.62137.E8.

[28] G. C. Cheng, H. M. Loree, R. D. Kamm, M. C. Fishbein, and R. T. Lee. Distribution of circumferential stress in ruptured and stable atherosclerotic lesions. a structural analysis with histopathological correlation. *Circulation*, 87(4):1179–1187, 1993. doi: 10.1161/01.cir.87.4.1179.

[29] S. N. D. Chua, B. J. MacDonald, and M. S. J. Hashmi. Finite element simulation of slotted tube (stent) with the presence of plaque and artery by balloon expansion. *Journal of Materials Processing Technology*, 155:1772–1779, 2004. doi: 10.1016/j.jmatprotec.2004.04.396.

[30] R. M. Cooper and P. M. Naghdi. Propagation of nonaxially symmetric waves in elastic cylindrical shells. *The Journal of the Acoustical Society of America*, 29(12):1365–1373, 1957. doi: 10.1121/1.1908812.

[31] V. A. Del Grosso and R. E. McGill. Remarks on "axially symmetric vibrations of a thin cylindrical elastic shell filled with nonviscous, compressible fluid" by Ram Kumar, Acustica 17. *Acustica*, 20(6):313–314, 1968.

[32] C. R. Ethier and C. A. Simmons. *Introductory Biomechanics: From Cells to Organisms*. Cambridge Texts in Biomedical Engineering. Cambridge University Press, 2007. ISBN 978-0-521-84112-2.

[33] E. Falk. Why do plaques rupture? *Circulation*, 86(6 Suppl):III30–42, 1992.

[34] A. Farshidianfar and P. Oliazadeh. Free vibration analysis of circular cylindrical shells: Comparison of different shell theories. *International Journal of Mechanics and Applications*, 2(5):74–80, 2012. doi: 10.5923/j.mechanics.20120205.04.

[35] L. Formaggia, D. Lamponi, and A. Quarteroni. One-dimensional models for blood flow in arteries. *Journal of Engineering Mathematics*, 47(3-4):251–276, 2003. doi: 10.1023/B:ENGI.0000007980.01347.29.

[36] S. Frecentese, L. P. Argani, A. B. Movchan, N. V. Movchan, G. Carta, and M. L. Wall. Waves and fluid–solid interaction in stented blood vessels. *Proceedings of the Royal Society of London A: Mathematical, Physical and Engineering Sciences*, 474 (2209), 2018. doi: 10.1098/rspa.2017.0670.

[37] S. Frecentese, T. K. Papathanasiou, A. B. Movchan, and N. V. Movchan. Dispersion of waves and transmission–reflection in blood vessels with structured stents. *Proceedings of the Royal Society of London A: Mathematical, Physical and Engineering Sciences*, 475(2223):20180816, 2019. doi: 10.1098/rspa.2018.0816.

[38] C. R. Fuller. The effects of wall discontinuities on the propagation of flexural waves in cylindrical shells. *Journal of Sound and Vibration*, 75(2):207–228, 1981. doi: 10.1016/0022-460X(81)90340-0.

[39] C. R. Fuller and F. J. Fahy. Characteristics of wave propagation and energy distributions in cylindrical elastic shells filled with fluid. *Journal of Sound and Vibration*, 81(4):501–518, 1982. doi: 10.1016/0022-460X(82)90293-0.

[40] D. Gastaldi, S. Morlacchi, R. Nichetti, C. Capelli, G. Dubini, L. Petrini, and F. Migliavacca. Modelling of the provisional side-branch stenting approach for the treatment of atherosclerotic coronary bifurcations: effects of stent positioning. *Biomechanics and Modeling in Mechanobiology*, 9(5):551–561, 2010. doi: 10.1007/s10237-010-0196-8.

[41] D. C. Gazis. Three-dimensional investigation of the propagation of waves in hollow circular cylinders. i. analytical foundation. *The journal of the Acoustical Society of America*, 31(5):568–573, 1959. doi: 10.1121/1.1907753.

[42] D. C. Gazis. Three-dimensional investigation of the propagation of waves in hollow circular cylinders. ii. numerical results. *The journal of the Acoustical Society of America*, 31(5):573–578, 1959. doi: 10.1121/1.1907754.

[43] D. C. Gazis. Errata: Three-dimensional investigation of the propagation of waves in hollow circular cylinders. ii. *The journal of the Acoustical Society of America*, 32 (4):515–515, 1960. doi: 10.1121/1.1908132.

[44] R. L. Gleason, J.-J. Hu, and J. D. Humphrey. Building a functional artery: issues from the perspective of mechanics. *Front Biosci*, 9:2045–2055, 2004. doi: 10.2741/1387.

[45] R. L. Gleason, L. A. Taber, and J. D. Humphrey. A 2-d model of flow-induced alterations in the geometry, structure, and properties of carotid arteries. *Journal of Biomechanical Engineering*, 126(3):371–381, 2004. doi: 10.1115/1.1762899.

[46] S. G. Haslinger, A. B. Movchan, N. V. Movchan, and R. C. McPhedran. Symmetry and resonant modes in platonic grating stacks. *Waves in Random and Complex Media*, 24(2):126–148, 2014. doi: 10.1080/17455030.2014.884733.

[47] G. Herrmann and I. Mirsky. Three-dimensional and shell theory analysis of axially-symmetric motions of cylinders. Technical report, Columbia University. Institute of Air Flight Structures, 1955.

[48] G. Herrmann and I. Mirsky. Three-dimensional and shell theory analysis of axially symmetric motions of cylinders. *Journal of Applied Mechanics*, 23:563–568, 1956.

[49] M. Hirschhorn, V. Tchantchaleishvili, R. Stevens, J. Rossano, and A. Throckmorton. Fluid-structure interaction modeling in cardiovascular medicine - a systematic review 2017–2019. *Medical Engineering & Physics*, 2020. doi: 10.1016/j.medengphy.2020.01.008.

[50] G. A. Holzapfel. Structural and numerical models for the (visco) elastic response of arterial walls with residual stresses. In *Biomechanics of Soft Tissue in Cardiovascular Systems*, pages 109–184. Springer, 2003. doi: 10.1007/978-3-7091-2736-0_4.

[51] G. A. Holzapfel, T. C. Gasser, and R. W. Ogden. Comparison of a multi-layer structural model for arterial walls with a fung-type model, and issues of material stability. *Journal of Biomechanical Engineering*, 126(2):264–275, 2004. doi: 10.1115/1.1695572.

[52] G. A. Holzapfel, G. Sommer, and P. Regitnig. Anisotropic mechanical properties of tissue components in human atherosclerotic plaques. *J. Biomech. Eng.*, 126(5): 657–665, 2004. doi: 10.1115/1.1800557.

[53] G. A. Holzapfel, G. Sommer, T. C. Gasser, and P. Regitnig. Determination of layer-specific mechanical properties of human coronary arteries with nonatherosclerotic intimal thickening and related constitutive modelling. *American Journal of Physiology-Heart and Circulatory Physiology*, 289(5):H2048–H2058, 2005. doi: 10.1152/ajpheart.00934.2004.

[54] T. J. R. Hughes. *The Finite Element Method: Linear Static and Dynamic Finite Element Analysis*. Dover Civil and Mechanical Engineering. Dover Publications, 2000. ISBN 0486411818,9780486411811.

[55] T. J. R. Hughes and J. Lubliner. On the one-dimensional theory of blood flow in the larger vessels. *Mathematical Biosciences*, 18(1-2):161–170, 1973. doi: 10.1016/0025-5564(73)90027-8.

[56] J. D. Humphrey and S. L. O'Rourke. *An Introduction to Biomechanics: Solids and Fluids, Analysis and Design*. Springer-Verlag New York, 2 edition, 2015. ISBN 978-1-4939-2622-0. doi: 10.1007/978-1-4939-2623-7.

[57] S. K. Jaganathan, A. P. Subramanian, A. A. John, M. V. Vellayappan, A. Balaji, E. Supriyanto, B. Gundumalai, and A. K. Jaganathan. Estimation and comparison of natural frequency of coronary metallic stents using modal analysis. *Indian Journal of Science and Technology*, 8(12):1–7, 2015. doi: 10.17485/ijst/2015/v8i12/58966.

[58] J. Jiang, K. Baik, and T. G. Leighton. Acoustic attenuation, phase and group velocities in liquid-filled pipes ii: Simulation for spallation neutron sources and planetary exploration. *The Journal of the Acoustical Society of America*, 130(2):695–706, 2011. doi: 10.1121/1.3598463.

[59] G. S. Karanasiou, M. I. Papafaklis, C. Conway, L. K. Michalis, R. Tzafriri, E. R. Edelman, and D. I. Fotiadis. Stents: biomechanics, biomaterials, and insights from computational modeling. *Annals of Biomedical Engineering*, 45(4):853–872, 2017. doi: 10.1007/s10439-017-1806-8.

[60] C. Kittel. *Introduction to Solid State Physics*. Wiley, 7 edition, 1996. ISBN 9780471111818,0471111813.

[61] R. Kumar. Axially symmetric vibrations of a thin cylindrical elastic shell filled with nonviscous, compressible fluid. *Acustica*, 17(4):218–222, 1966.

[62] R. Kumar. Flexural vibrations of fluid-filled circular cylindrical shells. *Acustica*, 24 (3):137–146, 1971.

[63] R. Kumar. Dispersion of axially symmetric waves in empty and fluid-filled cylindrical shells. *Acustica*, 27(6):317–329, 1972.

[64] R. Kumar. Axially symmetric vibrations of finite cylindrical shells of various wall thicknesses - i. *Acustica*, 34(5):281–288, 1976.

[65] R. Kumar and R. W. B. Stephens. Dispersion of flexural waves in circular cylindrical shells. *Proceedings of the Royal Society of London. A. Mathematical and Physical Sciences*, 329(1578):283–297, 1972. doi: 10.1098/rspa.1972.0114.

[66] C. Lally, F. Dolan, and P. J. Prendergast. Cardiovascular stent design and vessel stresses: a finite element analysis. *Journal of Biomechanics*, 38(8):1574–1581, 2005. doi: 10.1016/j.jbiomech.2004.07.022.

[67] M. G. Lawlor, M. R. O'Donnell, B. M. O'Connell, and M. T. Walsh. Experimental determination of circumferential properties of fresh carotid artery plaques. *Journal of Biomechanics*, 44(9):1709–1715, 2011. doi: 10.1016/j.jbiomech.2011.03.033.

[68] S. H. Lee, Y. Jang, S. J. Oh, K. J. Park, Y. S. Moon, J. W. Min, J. Y. Yang, and G. J. Jang. Overlapping vs. one long stenting in long coronary lesions. *Catheterization and Cardiovascular Interventions*, 62(3):298–302, 2004. doi: 10.1002/ccd.20091.

[69] J. Lekner. *Theory of Reflection.* Springer, 1987. ISBN 978-3-319-23626-1.

[70] E. Leybovitch, S. Golan, and M. Brand. Mechanical interaction between overlapping stents and peripheral arteries-numerical model. In *Modelling Symposium (EMS), 2015 IEEE European*, pages 76–79. IEEE, 2015.

[71] Z. Li and D. Kleinstreuer. Blood flow and structure interactions in a stented abdominal aortic aneurysm model. *Medical Engineering & Physics*, 27(5):369–382, 2005. doi: 10.1016/j.medengphy.2004.12.003.

[72] T. C. Lin and G. W. Morgan. Wave propagation through fluid contained in a cylindrical, elastic shell. *The Journal of the Acoustical Society of America*, 28(6): 1165–1176, 1956. doi: 10.1121/1.1908583.

[73] Z. Liu, T. Li, X. Zhu, and J. Zhang. The effect of hydrostatic pressure fields on the dispersion characteristics of fluid-shell coupled system. *Journal of Marine Science and Application*, 9(2):129–136, 2010. doi: 10.1007/s11804-010-9010-3.

[74] H. M. Loree, A. J. Grodzinsky, S. Y. Park, L. J. Gibson, and R. T. Lee. Static circumferential tangential modulus of human atherosclerotic tissue. *Journal of Biomechanics*, 27(2):195–204, 1994. doi: 10.1016/0021-9290(94)90209-7.

[75] E. Maher, A. Creane, S. Sultan, N. Hynes, C. Lally, and D. J. Kelly. Tensile and compressive properties of fresh human carotid atherosclerotic plaques. *Journal of Biomechanics*, 42(16):2760–2767, 2009. doi: 10.1016/j.jbiomech.2009.07.032.

[76] D. A. McDonald. *Blood Flow in Arteries.* London Edward Arnold, 1 edition, 1960.

[77] N. W. McLachlan. *Theory and Application of Mathieu Functions.* Clarendon Press, 1951.

[78] H. D. McNiven, J. L. Sackman, and A. H. Shah. Axially symmetric waves in hollow, elastic rods: Part ii. *The Journal of the Acoustical Society of America*, 40 (5):1073–1076, 1966. doi: 10.1121/1.1910190.

[79] H. D. McNiven, A. H. Shah, and J. L. Sackman. Axially symmetric waves in hollow, elastic rods: Part i. *The Journal of the Acoustical Society of America*, 40 (4):784–792, 1966. doi: 10.1121/1.1910149.

[80] V. Melicher and V. Gajdošík. A numerical solution of a one-dimensional blood flow model–moving grid approach. *Journal of Computational and Applied Mathematics*, 215(2):512–520, 2008. doi: 10.1016/j.cam.2006.03.065.

[81] R. D. Mindlin and H. D. McNiven. Axially symmetric waves in elastic rods. *Journal of Applied Mechanics*, 27(1):145–151, 1960. doi: 10.1115/1.3643889.

[82] I. Mirsky. Vibrations of orthotropic, thick, cylindrical shells. *The Journal of the Acoustical Society of America*, 36(1):41–51, 1964. doi: 10.1121/1.1918910.

[83] I. Mirsky and G. Herrmann. Nonaxially symmetric motions of cylindrical shells. *The Journal of the Acoustical Society of America*, 29(10):1116–1123, 1957. doi: 10.1121/1.1908716.

[84] I. Mirsky and G. Herrmann. Axially symmetric motions of thick cylindrical shells. *Journal of Applied Mechanics*, 25(1):97–102, 1958.

[85] I. Mirsky and G. Herrmann. Nonaxially symmetric motions of cylindrical shells. *The Journal of the Acoustical Society of America*, 31(2):250, 1959. doi: 10.1121/1.1907707.

[86] G. S. Mishuris, A. B. Movchan, and J. P. Bercial. Asymptotic analysis of bloch–floquet waves in a thin bi-material strip with a periodic array of finite-length cracks. *Waves in Random and Complex Media*, 17(4):511–533, 2007. doi: 10.1080/17455030701288137.

[87] G. W. Morgan and J. P. Kiely. Wave propagation in a viscous liquid contained in a flexible tube. *The Journal of the Acoustical Society of America*, 26(3):323–328, 1954. doi: 10.1121/1.1907335.

[88] A. B. Movchan, N. V. Movchan, and C. G. Poulton. *Asymptotic models of fields in dilute and densely packed composites*. World Scientific, 2002.

[89] A. B. Movchan, N. V. Movchan, I. S. Jones, and D. J. Colquitt. *Mathematical Modelling of Waves in Multi-scale Structured Media*. CRC Press, 2017. ISBN 9781498782098.

[90] M. Naghavi, P. Libby, E. Falk, S. W. Casscells, S. Litovsky, J. Rumberger, J. J. Badimon, C. Stefanadis, P. Moreno, G. Pasterkamp, et al. From vulnerable plaque

to vulnerable patient: a call for new definitions and risk assessment strategies: Part i. *Circulation*, 108(14):1664–1672, 2003. doi: 10.1161/01.CIR.0000087480.94275.97.

[91] P. M. Naghdi and J. G. Berry. On the equations of motion of cylindrical shells. *Journal of Applied Mechanics*, 21(2):160–166, 1954.

[92] P. M. Naghdi and R. M. Cooper. Propagation of elastic waves in cylindrical shells, including the effects of transverse shear and rotatory inertia. *The Journal of the Acoustical Society of America*, 28(1):56–63, 1956.

[93] F. Nematzadeh and S. K. Sadrnezhaad. Effects of material properties on mechanical performance of nitinol stent designed for femoral artery: Finite element analysis. *Scientia Iranica B*, 19(6):1564–1571, 2012. doi: 10.1016/j.scient.2012.10.024.

[94] W. W. Nichols, M. F. O'Rourke, and C. Vlachopoulos. *McDonald's Blood Flow in Arteries: Theoretical, Experimental and Clinical Principles*. CRC Press, 6 edition, 2011. ISBN 978-0-340-985-014.

[95] W. J. Olver, D. W. Ronald Lozier, F. Boisvert, and C. W. Clark. *NIST Handbook of Mathematical Functions*. Cambridge University Press, 1 pap/cdr edition, 2010. ISBN 0521140633,9780521140638,9780521192255,0521192250.

[96] T. K. Papathanasiou, A. B. Movchan, and D. Bigoni. Wave reflection and transmission in multiply stented blood vessels. *Proceedings of the Royal Society A: Mathematical, Physical and Engineering Sciences*, 473(2202), 2017. doi: 10.1098/rspa.2017.0015.

[97] I. Pericevic, C. Lally, D. Toner, and D. J. Kelly. The influence of plaque composition on underlying arterial wall stress during stent expansion: the case for lesion-specific stents. *Medical engineering & physics*, 31(4):428–433, 2009. doi: 10.1016/j.medengphy.2008.11.005.

[98] B. Peynircioglu, B. E. Cil, and M. Karcaaltincaba. Standing or stationary arterial waves of the superior mesenteric artery at mr angiography and subsequent conventional arteriography. *Journal of Vascular and Interventional Radiology*, 10(18):1329–1330, 2007. doi: 10.1016/j.jvir.2007.07.005.

[99] P. J. Prendergast, C. Lally, S. Daly, A. J. Reid, T. C. Lee, D. Quinn, and F. Dolan. Analysis of prolapse in cardiovascular stents: A constitutive equation for vascular tissue and finite-element modelling. *Journal of Biomechanical Engineering*, 125(5):692–699, 2003. doi: 10.1115/1.1613674.

[100] L. Räber, P. Jüni, L. Löffel, S. Wandel, S. Cook, P. Wenaweser, M. Togni, R. Vogel, C. Seiler, F. Eberli, et al. Impact of stent overlap on angiographic and long-term clinical outcome in patients undergoing drug-eluting stent implantation. *Journal of the American College of Cardiology*, 55(12):1178–1188, 2010. doi: 10.1016/j.jacc.2009.11.052.

[101] S. S. Rao. *Vibration of Continuous Systems*. John Wiley & Sons, 2007. ISBN 978-0-471-77171-5.

[102] F. Rikhtegar, C. Wyss, K. S. Stok, D. Poulikakos, R. Müller, and V. Kurtcuoglu. Hemodynamics in coronary arteries with overlapping stents. *Journal of Biomechanics*, 47(2):505–511, 2014. doi: 10.1016/j.jbiomech.2013.10.048.

[103] D. Rubenstein, W. Yin, and M. D. Frame. *Biofluid Mechanics: An Introduction to Fluid Mechanics, Macrocirculation, and Microcirculation*. Academic Press, 2015.

[104] D. Scheinert, S. Scheinert, J. Sax, C. Piorkowski, S. Bräunlich, M. Ulrich, G. Biamino, and A. Schmidt. Prevalence and clinical impact of stent fractures after femoropopliteal stenting. *Journal of the American College of Cardiology*, 45(2): 312–315, 2005. doi: 10.1016/j.jacc.2004.11.026.

[105] A. Schiavone, L. G. Zhao, and A. A. Abdel-Wahab. Dynamic simulation of stent deployment - effects of design, material and coating. *Journal of Physics: Conference Series*, 451(1):012032, 2013. doi: 10.1088/1742-6596/451/1/012032.

[106] M. Schillinger, M. Exner, W. Mlekusch, M. Haumer, R. Ahmadi, H. Rumpold, O. Wagner, and E. Minar. Inflammatory response to stent implantation: differences in femoropopliteal, iliac, and carotid arteries. *Radiology*, 224(2):529–535, 2002. doi: 10.1148/radiol.2241011253.

[107] M. Schillinger, M. Exner, W. Mlekusch, M. Haumer, R. Ahmadi, H. Rumpold, O. Wagner, and E. Minar. Balloon angioplasty and stent implantation induce a vascular inflammatory reaction. *Journal of Endovascular Therapy*, 9(1):59–66, 2002. doi: 10.1177/152660280200900111.

[108] N. K. C. Selvarasu, D. K. Tafti, and P. P. Vlachos. Hydrodynamic effects of compliance mismatch in stented arteries. *Journal of biomechanical engineering*, 133 (2), 2011. doi: 10.1115/1.4003319.

[109] W. Soedel. *Vibrations of Shells and Plates*. Dekker Mechanical Engineering. CRC Press, 3 edition, 2004. ISBN 978-0-8247-5629-1.

[110] S. V. Sorokin, F. Gautier, and A. Pelat. A hierarchy of models of axisymmetric wave propagation in a fluid-filled periodic cylindrical shell composed of high-contrast cells. *Mechanical Systems and Signal Processing*, 136:106487, 2020. doi: 10.1016/j.ymssp.2019.106487.

[111] J. Tambaca, S. Canic, M. Kosor, R. D. Fish, and D. Paniagua. Mechanical behavior of fully expanded commercially available endovascular coronary stents. *Texas Heart Institute Journal*, 38(5):491–501, 2011.

[112] A. S. Tijsseling and A. Anderson. A. Isebree Moens and DJ Korteweg: on the speed of propagation of waves in elastic tubes. In *Proc. 11th International Conference on Pressure Surges*, pages 227–245, 2012.

[113] L. D. T. Topoleski and B. Stephen. *Biomechanical Behavior of Atherosclerotic Plaque*, pages 869–911. Springer Berlin, 2015. ISBN 978-3-7091-1309-7. doi: 10.1007/978-3-642-37078-6_31.

[114] L. D. T. Topoleski, N. V. Salunke, J. D. Humphrey, and W. J. Mergner. Composition- and history-dependent radial compressive behavior of human atherosclerotic plaque. *Journal of Biomedical Materials Research: An Official Journal of The Society for Biomaterials and The Japanese Society for Biomaterials*, 35(1):117–127, 1997.

[115] J. P. Tullis. *Hydraulics of Pipelines: Pumps, Valves, Cavitation, Transients*. John Wiley & Sons, 1989.

[116] F. N. Van de Vosse and N. Stergiopulos. Pulse wave propagation in the arterial tree. *Annual Review of Fluid Mechanics*, 43:467–499, 2011.

[117] A. Vellender and G. S. Mishuris. Eigenfrequency correction of bloch-floquet waves in a thin periodic bi-material strip with cracks lying on perfect and imperfect interfaces. *Wave Motion*, 49(2):258–270, 2012. doi: 10.1016/j.wavemoti.2011.11.002.

[118] A. Vellender, G. S. Mishuris, and A. B. Movchan. Weight function in a bimaterial strip containing an interfacial crack and an imperfect interface. application to bloch-floquet analysis in a thin inhomogeneous structure with cracks. *Multiscale Modeling & Simulation*, 9(4):1327–1349, 2011. doi: 10.1137/110824838.

[119] W. Walke, Z. Paszenda, and J. Filipiak. Experimental and numerical biomechanical analysis of vascular stent. *Journal of Materials Processing Technology*, 164-165: 1263–1268, 2005. doi: 10.1016/j.jmatprotec.2005.02.204.

[120] M. Wall, S. Frecentese, N. Movchan, and A. Movchan. Dynamic response of stents in vascular systems: Development of an adaptive model to study the effect of stent placement on aneurysmal and occlusive arterial disease in various anatomical configuration. *European Journal of Vascular and Endovascular Surgery*, 58(6):e853, 2019.

[121] J. R. Womersley. Method for the calculation of velocity, rate of flow and viscous drag in arteries when the pressure gradient is known. *The Journal of physiology*, 127(3):553, 1955.

[122] J. R. Womersley. Xxiv. oscillatory motion of a viscous liquid in a thin-walled elastic tube i: The linear approximation for long waves. *The London, Edinburgh, and Dublin Philosophical Magazine and Journal of Science*, 46(373):199–221, 1955.

[123] J. Xu, J. Yang, S. Sohrabi, Y. Zhou, and Y. Liu. Finite element analysis of the implantation process of overlapping stents. *Journal of medical devices*, 11(2):021010, 2017. doi: 10.1115/1.4036391.

[124] H. Zahedmanesh and C. Lally. Determination of the influence of stent strut thickness using the finite element method: implications for vascular injury and in-stent restenosis. *Medical & Biological Engineering & Computing*, 47(4):385–393, 2009. doi: 10.1007/s11517-009-0432-5.

[125] X. M. Zhang, G. R. Liu, and K. Y. Lam. Vibration analysis of thin cylindrical shells using wave propagation approach. *Journal of Sound and Vibration*, 239(3): 397–403, 2001. doi: 10.1006/jsvi.2000.3139.

[126] X. M. Zhang, G. R. Liu, and K. Y. Lam. Coupled vibration analysis of fluid-filled cylindrical shells using the wave propagation approach. *Applied Acoustics*, 62(3): 229–243, 2001. doi: 10.1016/S0003-682X(00)00045-1.

[127] Y. Zhang, M. L. Dunn, K. S. Hunter, C. Lanning, D. D. Ivy, L. Claussen, S. J. Chen, and R. Shandas. Application of a microstructural constitutive model of the pulmonary artery to patient-specific studies: Validation and effect of orthotropy. *Journal of Biomechanical Engineering*, 192(2):193–201, 2007. doi: 10.1115/1.2485780.